X-ray computed tomography reconstruction on non-standard trajectories for robotized inspection

Hussein Banjak

N°d'ordre NNT : 2016LYSEI113

THESE de DOCTORAT DE L'UNIVERSITE DE LYON
opérée au sein de
L'institut National des Sciences Appliquées de Lyon

Ecole Doctorale 160
Électronique, Électrotechnique, Automatique

Spécialité de doctorat :
Discipline : Traitement du Signal et de l'Image

Soutenue publiquement le 10 Novembre 2016 par :
Hussein Banjak

X-ray Computed Tomography Reconstruction on Non-Standard Trajectories for Robotized Inspection

---

Devant le jury composé de :

Jan SIJBERS	Professeur des Universités, Université de Antwerp	Rapporteur
Thomas RODET	Professeur des Universités, ENS Cachan	Rapporteur
Françoise PEYRIN	Directrice de Recherche, INSERM	Examinatrice
Ulf HASSLER	Ingénieur de Recherche, Fraunhofer EZRT	Examinateur
Agnès Decroux	Ingénieure de Recherche, CyXplus	Membre invité
Valérie KAFTANDJIAN	Professeur des Universités, INSA-Lyon	Directrice de thèse
Marius COSTIN	Ingénieur de Recherche, CEA-Saclay	Encadrant de thèse
Caroline VIENNE	Ingénieure de Recherche, CEA-Saclay	Encadrante de thèse

CEA, LIST
Département d'Imagerie et de Simulation pour le Contrôle (DISC)

Département FEDORA – INSA Lyon - Ecoles Doctorales – Quinquennal 2016-2020

SIGLE	ECOLE DOCTORALE	NOM ET COORDONNEES DU RESPONSABLE
CHIMIE	**CHIMIE DE LYON** **http://www.edchimie-lyon.fr** Sec : Renée EL MELHEM Bat Blaise Pascal 3e etage secretariat@edchimie-lyon.fr Insa : R. GOURDON	M. Stéphane DANIELE Institut de Recherches sur la Catalyse et l'Environnement de Lyon IRCELYON-UMR 5256 Équipe CDFA 2 avenue Albert Einstein 69626 Villeurbanne cedex directeur@edchimie-lyon.fr
E.E.A.	**ELECTRONIQUE, ELECTROTECHNIQUE, AUTOMATIQUE** **http://edeea.ec-lyon.fr** Sec : M.C. HAVGOUDOUKIAN Ecole-Doctorale.eea@ec-lyon.fr	M. Gérard SCORLETTI Ecole Centrale de Lyon 36 avenue Guy de Collongue 69134 ECULLY Tél : 04.72.18 60.97 Fax : 04 78 43 37 17 Gerard.scorletti@ec-lyon.fr
E2M2	**EVOLUTION, ECOSYSTEME, MICROBIOLOGIE, MODELISATION** **http://e2m2.universite-lyon.fr** Sec : Safia AIT CHALAL Bat Darwin - UCB Lyon 1 04.72.43.28.91 Insa : H. CHARLES Safia.ait-chalal@univ-lyon1.fr	Mme Gudrun BORNETTE CNRS UMR 5023 LEHNA Université Claude Bernard Lyon 1 Bât Forel 43 bd du 11 novembre 1918 69622 VILLEURBANNE Cédex Tél : 06.07.53.89.13 e2m2@ univ-lyon1.fr
EDISS	**INTERDISCIPLINAIRE SCIENCES-SANTE** **http://www.ediss-lyon.fr** Sec : Safia AIT CHALAL Hôpital Louis Pradel - Bron 04 72 68 49 09 Insa : M. LAGARDE Safia.ait-chalal@univ-lyon1.fr	Mme Emmanuelle CANET-SOULAS INSERM U1060, CarMeN lab, Univ. Lyon 1 Bâtiment IMBL 11 avenue Jean Capelle INSA de Lyon 696621 Villeurbanne Tél : 04.72.68.49.09 Fax :04 72 68 49 16 Emmanuelle.canet@univ-lyon1.fr
INFOMATHS	**INFORMATIQUE ET MATHEMATIQUES** **http://infomaths.univ-lyon1.fr** Sec :Renée EL MELHEM Bat Blaise Pascal 3e etage infomaths@univ-lyon1.fr	Mme Sylvie CALABRETTO LIRIS – INSA de Lyon Bat Blaise Pascal 7 avenue Jean Capelle 69622 VILLEURBANNE Cedex Tél : 04.72. 43. 80. 46 Fax 04 72 43 16 87 Sylvie.calabretto@insa-lyon.fr
Matériaux	**MATERIAUX DE LYON** **http://ed34.universite-lyon.fr** Sec : M. LABOUNE PM : 71.70 –Fax : 87.12 Bat. Saint Exupéry Ed.materiaux@insa-lyon.fr	M. Jean-Yves BUFFIERE INSA de Lyon MATEIS Bâtiment Saint Exupéry 7 avenue Jean Capelle 69621 VILLEURBANNE Cedex Tél : 04.72.43 71.70 Fax 04 72 43 85 28 Ed.materiaux@insa-lyon.fr
MEGA	**MECANIQUE, ENERGETIQUE, GENIE CIVIL, ACOUSTIQUE** **http://mega.universite-lyon.fr** Sec : M. LABOUNE PM : 71.70 –Fax : 87.12 Bat. Saint Exupéry mega@insa-lyon.fr	M. Philippe BOISSE INSA de Lyon Laboratoire LAMCOS Bâtiment Jacquard 25 bis avenue Jean Capelle 69621 VILLEURBANNE Cedex Tél : 04.72 .43.71.70 Fax : 04 72 43 72 37 Philippe.boisse@insa-lyon.fr
ScSo	**ScSo*** **http://recherche.univ-lyon2.fr/scso/** Sec : Viviane POLSINELLI Brigitte DUBOIS Insa : J.Y. TOUSSAINT viviane.polsinelli@univ-lyon2.fr	Mme Isabelle VON BUELTZINGLOEWEN Université Lyon 2 86 rue Pasteur 69365 LYON Cedex 07 Tél : 04.78.77.23.86 Fax : 04.37.28.04.48

*ScSo : Histoire, Géographie, Aménagement, Urbanisme, Archéologie, Science politique, Sociologie, Anthropologie

Abstract

The number of industrial applications of computed tomography (CT) is large and rapidly increasing with typical areas of use in the aerospace, automotive and transport industry. To support this growth of CT in the industrial field, the identified requirements concern firstly software development to improve the reconstruction algorithms and secondly the automation of the inspection process. Indeed, the use of robots gives more flexibility in the acquisition trajectory and allows the control of large and complex objects, which cannot be inspected using classical CT systems.

In this context of new CT trend, a robotic platform has been installed at CEA LIST to better understand and solve specific challenges linked to the robotization of the CT process. The considered system integrates two robots that move the X-ray generator and detector. This thesis aims at achieving this new development. In particular, the objective is to develop and implement analytical and iterative reconstruction algorithms adapted to such robotized trajectories. The main focus of this thesis is concerned with helical-like scanning trajectories. We consider two main problems that could occur during acquisition process: truncated and limited-angle data. We present in this work experimental results for reconstruction on such non-standard trajectories. CIVA software is used to simulate these complex inspections and our developed algorithms are integrated as reconstruction tools.

This thesis contains three parts. In the first part, we introduce the basic principles of CT and we present an overview of existing analytical and iterative algorithms for non-standard trajectories. In the second part, we modify the approximate helical FDK algorithm to deal with transversely truncated data and we propose a modified FDK algorithm adapted to reverse helical trajectory with the scan range less than 360°.For iterative reconstruction, we propose two algebraic methods named SART-FISTA-TV and DART-FISTA-TV which are based on SART and DART, respectively. These two algorithms perform well from limited-angle data and few-view projections. In the third part, we perform experimental CT inspections using the robotic platform and 3D images were reconstructed using the algorithms developed during the thesis.

Keywords : Robotic tomography, non-destructive testing, analytical and iterative reconstruction, non-standard scanning trajectories, limited-angle data, truncated data, few projection views.

Contents

Chapter 1

Introduction

1.1 Context

This thesis addresses research topics in the field of X-ray industrial non destructive testing (NDT). NDT is a highly valuable technique as it allows to evaluate the properties of a material or system without damaging it. Among the various NDT methods (such as ultrasonic, thermography, eddy-current, radiography...), X-ray computed tomography (CT) is a powerful tool to characterize or localize inner flaws and to verify the geometric conformity of an object. The use of CT is large and has increased dramatically in many industrial areas to inspect components for flaw detection, geometric measurement as well as for reverse engineering applications. CT can be used for inspection of components during manufacturing and this can ensure product integrity and contribute to optimize production costs.

In the context of new CT trends, robot-based CT systems were developed for both NDT at the Fraunhofer Development Center X-ray Technology (EZRT) [47] and for medical applications at Siemens Healthcare [36]. Very recently, an advanced robotic X-ray NDT platform has been installed at CEA LIST (see Fig. 1.1). The platform consists of two multi-axes cooperative robots equipped with an X-ray source and detector and allows a large variety of acquisitions on non-standard trajectories. This CT robotized system enables to process non-conventional scans for three-dimensional (3D) image reconstruction of complex and large industrial pieces that can not be inspected using classical CT systems. During data acquisition we do not need to move the inspected object where our strategy is based on the concept that only the two robots move which ensures a new level of automation during the inspection process. Examples of such advanced platform applications include detection of flaws, dimensional measurement and 3D analysis of complex objects in the domains of automotive, aeronautics and manufacturing areas.

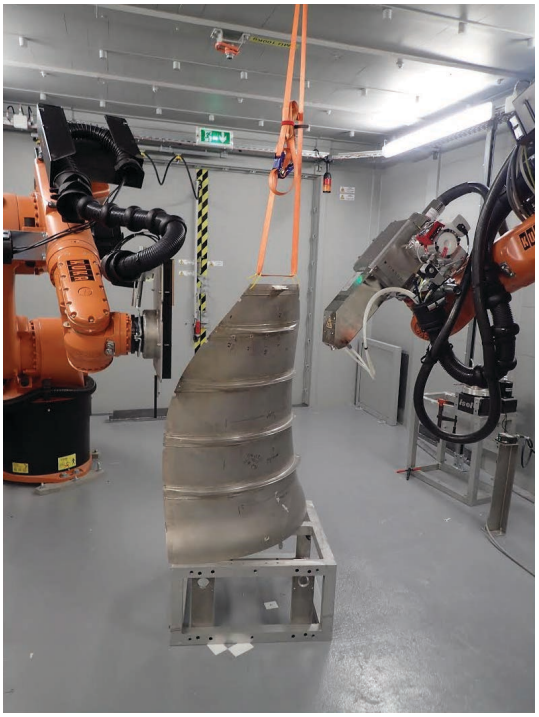

FIGURE 1.1: Robotic X-ray inspection platform installed at CEA LIST.

1.2 Objective and Major Challenges

Compared to medical CT, the scanned object in NDT might be very large and composed of high-attenuation materials and consequently the use of a standard circular trajectory for data acquisition would be impossible due to constraints in space. In some cases like the inspection of planar objects such as printed circuit boards, the use of computed laminography [146] is suitable. However, this technique concentrates on one plane only and thus the obtained resolution in the object is anisotropic. Thus, the use of robotic arms is one of the acknowledged new trends in NDT since it allows laminography and even more flexible acquisition trajectories and therefore could be used for 3D reconstruction of hardly accessible regions that might be a major limitation of classical CT systems. This technology enables a large variety of scanning trajectories for the inspection of complex industrial pieces or objects with unfavorable dimensions to X-ray penetration. A simple example of such inspection trajectories is the popular helical trajectory that can deal with long objects which is the major limitation of a circular scanning trajectory.

Among the new challenges brought by robotic CT, we focus in this thesis more particularly on the limited access viewpoint imposed by the setup where important constraints control the mechanical motion of the platform. The second major challenge is the truncation of projections that occur when only a field-of-view (FOV) of the object

is viewed by the detector.

Another challenge is the localization of source and detector for each point of the trajectory where position error of the robots can introduce artifacts in the reconstruction. This particular challenge is not addressed in this work. Nevertheless, it is possible to reduce the impact of this known limitation of robotic CT by choosing robots of high accuracy and integrating a geometric calibration method of the CT system.

Before performing real robotic inspections, we highly rely on CT simulations to evaluate the capability of the reconstruction algorithm corresponding to a defined scanning trajectory and data acquisition configuration. For this purpose, we use CIVA which is an advanced NDT simulation platform developed at CEA [22] and that can provide a realistic model for radiographic acquisitions and is capable of simulating the projection data corresponding to a specific CT scene defined by the user. Thus, the main objective of this thesis is to develop reconstruction algorithms adapted to non-standard trajectories and to integrate these algorithms in CIVA software as plugins of reconstruction.

1.3 Original Contributions

In this thesis, we present both analytical and iterative reconstruction algorithms. For analytical reconstruction, we consider only the helical/helical-like scanning trajectory. On the other hand, the proposed iterative algorithms can deal with arbitrary trajectories of acquisition. We mainly focus on two important aspects that may occur during data acquisition: i) truncated data and ii) limited-angle data. We also aim to reconstruct from small number of projections in order to accelerate inspection cycles and to increase equipment life cycles. Our proposed algorithms are firstly tested with CIVA simulated data and then used to perform 3D reconstructions from experimental data acquired with the robotic inspection platform. A brief description of these original contributions is given here.

- **Analytical algorithms for helical trajectory**

  We have presented a theoretical overview and implementation details of three analytical reconstruction algorithms adapted to helical scanning trajectory. The first two algorithms are exact and were developed by Zou and Pan [150, 149] and the third one is the popular approximate Feldkamp-Davis-Kress (FDK) algorithm [113]. We have implemented these three algorithms and proposed an optimization approach for the implementation of the FBP algorithm. A numerical comparison of the three algorithms using both complete (noiseless and noisy) and truncated CIVA-simulated data was presented at an international conference [2]. In addition, our implementation of the helical FDK algorithm was integrated

as a plugin of reconstruction in CIVA CT and this work was a part of a paper presented at an international conference [22].

- **Reconstruction from truncated data**

  We have proposed two helical FDK-type algorithms that can handle transversely truncated data and we showed by numerical simulations (using CIVA) that these two algorithms perform well and can solve the well-known cup artifacts usually observed with the standard FDK algorithm in the case of truncated data. This contribution was presented at an international conference [5].

- **Reconstruction from limited-angle data**

  We have proposed two reconstruction algorithms for reverse helical trajectory in super-short-scan mode. The first one is analytical and of FDK-type and the second one is iterative and based on the algebraic SART algorithm [52]. A numerical comparison of the two algorithms was illustrated using CIVA-simulated data that were generated on a reverse helical trajectory limited to 150°. Based on the numerical results obtained, some remarks were concluded regarding the pros and cons of each algorithm when reconstructing with such configuration. These numerical results and concluding remarks were included in a paper that was presented at an international conference [4].

- **Iterative algorithms**

  We have presented an improved version of Discrete Algebraic Reconstruction Technique (DART) [7] which is an algebraic algorithm that can incorporate prior knowledge about the different materials (attenuation coefficients) of the scanned object into the reconstruction process. Our extended algorithm is called DART-FISTA-TV and combines DART with Total Variation (TV) regularization. We showed by numerical comparisons that the proposed DART-FISTA-TV algorithm can improve the image quality and performs better than the original DART algorithm when projection data are noisy. In addition, a regularized algebraic algorithm named SART-FISTA-TV was integrated in CIVA as a plugin of reconstruction. These results were presented at an international conference and will be published soon [3].

- **Reconstruction from experimental robotic acquisitions**

  We have shown reconstruction results from primary experimental acquisitions performed by the robotic platform. Different inspections were performed and then volume images were reconstructed using the proposed reconstruction algorithms. The first experimental results we obtained were presented as a Keynote at an international conference [6].

To summarize, this thesis is supported by six published conference papers [5, 2, 3, 4, 6, 22] and a journal paper is ready to be submitted. Here is a complete listing of these papers:

- H. Banjak, M. Costin, C. Vienne, V. Kaftandjian, "Two Local FBP Algorithms for Helical Cone-beam Computed Tomography". In: Digital Industrial Radiology and Computed Tomography, 2015.
- H. Banjak, M. Costin, C. Vienne, V. Kaftandjian, "Implementation and Evaluation of Two Helical CT Reconstruction Algorithms in CIVA". In: 42nd Annual Review of Progress in Quantitative Non-Destructive Evaluation. AIP Publishing, Vol. 1706. AIP Publishing, 2016, p. 110001.
- H. Banjak, M. Costin, C. Vienne, R. Guillamet, V. Kaftandjian, "Reconstruction Algorithms for Reverse Helical Super-Short-Scan Mode". In: 4th International Meeting on Image Formation in X-ray Computed Tomography, 2016.
- H. Banjak, M. Costin, C. Vienne, V. Kaftandjian, "X-ray Computed Tomography Reconstruction on Non-Standard Trajectories for Robotized Inspection". In: proceedings of the World Conference of NDT, 2016.
- M. Costin, D. Tisseur, C. Vienne, R. Guillamet, H. Banjak, N. Bhatia, R. Fernandez, "CIVA CT, an advanced simulation platform for NDT". In: 6th Conference on Industrial Computed Tomography, 2016.
- H. Banjak, M. Costin, C. Vienne, R. Guillamet, V. Kaftandjian, "Iterative CT Reconstruction on Limited Angle Trajectories Applied to Robotic Inspection". In: 43nd Annual Review of Progress in Quantitative Non-Destructive Evaluation. AIP Publishing, 2017 (to be published).

1.4 Thesis Outline

This thesis consists of seven chapters. After the introduction presented in the first chapter, we present a bibliographic study which is divided into two review chapters (Chapters 2 and 3). We demonstrate a brief description of these two chapters as follows:

- Chapter 2: We describe the fundamental principles of X-ray computed tomography including both physical basics of X-ray imaging and mathematics of image reconstruction process. We present also other important aspects like the evolution of CT scanners, data acquisition scanning trajectories and missing data problems as few-view, limited-angle and truncated data.

- Chapter 3: We review main analytical and iterative reconstruction methods for non-standard scanning trajectories. For analytical reconstruction, both exact and approximate algorithms are considered with a main focus on helical scanning trajectories. We introduce basic mathematical notations, geometry conventions and inversion formulas of some reconstruction algorithms. For iterative reconstruction, statistical and algebraic methods are reviewed. The reconstruction process of some algebraic methods is illustrated also. We terminate this chapter with some concluding remarks about the advantages and disadvantages of each approach.

We present our original contributions in the next three chapters (Chapters 4, 5 and 6). A description of these three chapters is as follows:

- Chapter 4: This chapter is devoted only to analytical algorithms for reconstruction on a helical scanning trajectory. We have implemented two exact helical algorithms. The implementation details are described and an optimized implementation was proposed. We show by numerical simulations the advantages of our proposed implementation and we compare the two exact algorithms with the popular approximate helical FDK algorithm. In addition, we propose two FDK-type algorithms for helical trajectory and that can handle transversely truncated data. CIVA simulated data are used to show the advantages of these two algorithms compared to the standard helical FDK algorithm when projection data are truncated transversely.

- Chapter 5: We present in this chapter contributions for both analytical and iterative reconstruction. We mainly focus on the limited-angle aspect of the trajectory. For analytical reconstruction, we propose an FDK-type algorithm adapted to limited-angle reverse helical trajectory. For the iterative part, two regularized algebraic algorithms: i) SART-FISTA-TV and ii) DART-FISTA-TV are proposed for reconstruction on such incomplete trajectory. We validate and compare the proposed algorithms and study their performance using numerical data generated by CIVA.

- Chapter 6: We present results from real data obtained with the robotic CT platform. Different inspections were performed on a helical scanning trajectory and with missing data configurations like truncated data and limited-angle data. We show 3D reconstructions based on real projection data and using both analytical and iterative algorithms. These first experimental results validate the performance of the inspection platform.

Finally, we summarize in Chapter 7 the thesis work and we discuss some possible future work about reconstruction algorithms development for the robotic inspection platform.

Chapter 2

Basic Principles of Computed Tomography

Fundamentally, tomography can be defined as a cross-sectional imaging technique that aims to create the image of a solid object from the set of its projections measured from different views. For X-ray imaging, we can get these projections by directing an X-ray beam at the object from different orientations and measuring its intensity attenuation when traversing the object being imaged. A set of such measurements is called sinogram and the main idea of CT is to recover the linear attenuation coefficient function of the object from the acquired sinogram.

The introduction of CT was fundamentally based on firstly the discovery of X-rays by Röntgen in 1895 and secondly the mathematical foundation to the solution of the inverse problem in CT which was presented by Radon in 1917. The applicability of first mathematical image reconstruction techniques on X-ray projections in medical applications were carried out independently by Oldendorf [81] and Cormack [21]. Bates and Peters [8] proposed Fourier-based reconstruction techniques and a key paper on the different reconstruction filters for Fourier-based CT reconstruction was published [93].

CT was first commercially introduced for medical imaging in 1971 by Hounsfield [42]. In 1979, Cormack and Hounsfield shared the Nobel Prize in Physiology and Medicine for their pioneer contributions in CT. In the eighties, this technology which can overcome the limitations of standard radiography has entered the industrial field and was used for NDT, material analysis and flaws detection like cracks and voids. Nowadays, the use of CT in industry has a wide range of potential applications in the manufacturing, automotive, aerospace, transport and food industry [25].

This chapter begins with the fundamental principles of CT regarding the physical basics of X-ray generation, X-ray interaction with matter and X-ray detection and the mathematical basics of image reconstruction. Then, it gives other important concepts as generations of CT systems, data acquisition scanning trajectories and missing data problem like few-view, limited-angle and truncated data.

2.1 Physical Principles

X-rays are a form of electromagnetic radiation which consist of photons with very short wavelengths (λ) ranging from a few picometers to a few nanometers (see Fig. 2.1). These short wavelength photons are of high energy E which is given by

$$E = \frac{hc}{\lambda}, \tag{2.1}$$

where $h = 6.6261 \times 10^{-34} J.s$ is Planck's constant and $c = 3 \times 10^{8} m/s$ is the speed of light in vacuum.

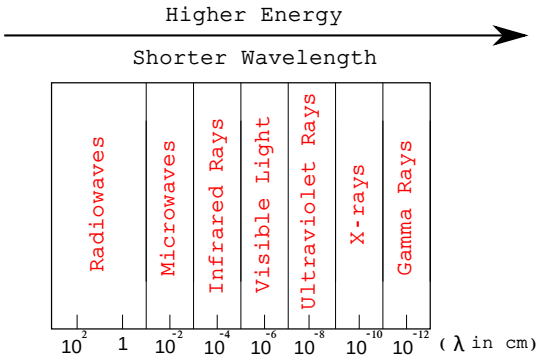

FIGURE 2.1: Illustration of electromagnetic spectrum.

We explain in this section the different physical aspects of X-rays starting from the process of its generation, then its interaction with matter and finally its detection.

2.1.1 X-ray Generation

X-rays are produced by accelerating electrons in a vacuum tube between cathode and anode (see Fig. 2.2). During this process of X-ray generation, the cathode which consists of a tungsten filament is heated by applying a voltage U_h and electrons are emitted from this heated cathode towards the anode. A high voltage U_{acc} is applied to accelerate the emitted electrons. Once these high velocity accelerated electrons strike the anode which is a metal target (usually tungsten), they are decelerated and X-ray radiation is created.

When the accelerated electrons collide with the anode, most of their kinetic energy gets converted to heat on the anode and only less than 1 % is transformed into X-rays. These X-rays are produced in two ways: i) Bremsstrahlung radiation and ii) characteristic radiation. Bremsstrahlung interaction produces most of the X-ray photons (approximately 80%). Bremsstrahlung is a German word which means "braking radiation" and is a good description of this process which happens when the emitted electrons that

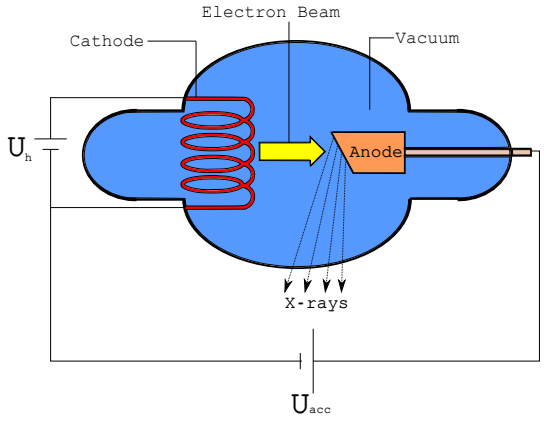

FIGURE 2.2: Diagram of an X-ray tube.

penetrate the anode material pass near the nucleus. The attractive force from the positively charged nucleus deflects and slows down these negatively charged high-speed electrons. The kinetic energy lost by these decelerated electrons appears in the form of photons. When the electron is more close to the nucleus, the electrostatic interaction and braking effect increases and as a result the energy of the resulting Bremsstrahlung photon is higher. Thus, the photons produced by this process are of different energy and the X-ray spectrum is continuous. The second process that produces characteristic radiation and that generates X-rays is based on the collision between the high-speed electrons and the orbital electrons of tungsten target atom within the tube anode. This interaction can happen only if the kinetic energy of the incoming electron is greater than the binding energy of the electron within the atom. When the collision occurs, an electron in one of the atom's lower orbital is removed leaving a vacancy that is filled by a higher orbital electron. As this high orbital electron moves down to fill the empty position, it releases its excess energy in the form of an X-ray photon whose energy is equivalent to the difference in the lower and higher binding energies. This process is named characteristic radiation because the energy of the emitted photons is characteristic of the material anode. Knowing that the probability for filling a K-shell vacancy is not the same for all shells, the number of generated photons at each characteristic energy is different. In contrast to Bremsstrahlung interaction which produces a continuous energy spectrum, a line spectrum with different discrete energies is produced in this interaction process.

The intensity of the X-ray beam depends on the filament temperature which is controlled by the cathode current. The more the cathode is heated, the more are the number of electrons released by the cathode and as a result the more are the emitted X-ray photons (thermionic emission). On the other hand, the energy of the X-ray photons is a function of the voltage across the tube which determines the kinetic energy of the electrons when they collide with the anode. As the accelerating voltage increases, the

energy of the X-ray photons increases and consequently their penetration power increases as well. Thus, the energy interval of the X-ray spectrum is determined by the applied voltage.

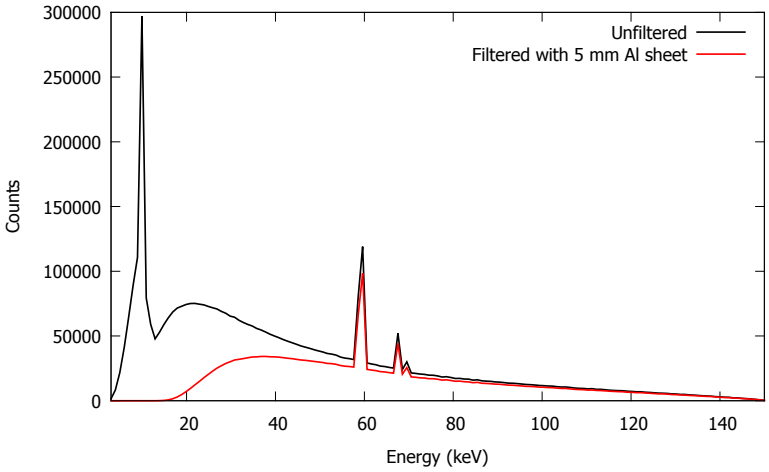

FIGURE 2.3: Example of an X-ray spectrum with and without Al filter.

To summarize, the generated X-ray beam consists of a spectrum of X-ray energy which is produced from characteristic and Bremsstrahlung radiation interaction described previously. This spectrum can be modified and controlled by the anode current and the accelerating voltage. Furthermore, thin metal sheets like aluminum (Al) or copper (Cu) could be placed in the path of the X-ray beam to remove low energy photons which do not have enough energy to reach the detector. This filtering of the beam helps in reducing the beam-hardening artifacts in the reconstructed image and in decreasing the patient dose for medical applications. Fig. 2.3 shows an example of a simulated output spectrum from a tungsten anode at 150 kV with unfiltered (black curve) and filtered (red curve) tube using 5 mm of Al which cuts low energy photons up to about 20 keV. The maximal energy of the shown continuous spectrum is 150 keV and the average energy is about 1/3 of the maximum energy value.

2.1.2 X-ray Matter Interaction

The basic physical principle of X-ray imaging is the interaction of X-radiation with the matter of the object to be imaged. In practice, when the X-ray beam passes through the object, it is attenuated due to three main interaction processes, which are photoelectric effect, Compton scattering and pair production. There exists also other phenomena of interaction which do not contribute significantly to X-ray attenuation like Rayleigh scattering which is an elastic scattering during which an interaction between the X-ray photon and atomic bound electrons occurs without ionizing or exciting these target

atoms. It should be mentioned that radiation with a smaller wavelength, i.e. a high-energy X-ray, is less attenuated when passing through matter than low-energy X-ray.

Photoelectric effect is a pure photon absorption process that depends strongly on the atomic number of the material and which results in total absorption of the X-ray photon and the emission of a bound electron. Compton scattering is an inelastic scattering process which is a mixture of photon energy absorption and scattering that results in a free electron and a scattered (less energetic) photon. During Compton scattering only a part of the X-ray photon energy is lost in contrast to photoelectric absorption where the entire energy of the X-ray photon is absorbed. Compton scattering is the dominant interaction mechanism for high energy radiation whereas photoelectric absorption dominates for low energy radiation. Pair production is a pure photon absorption process which is rare and occurs only when the energy of incident X-rays exceeds 1.02 MeV. This process becomes important when the X-ray photons energy exceeds 2 MeV and the material is of high atomic number. During this phenomenon, the X-ray photon interacts with the nucleus and as a result the X-ray photon is annihilated and an electron-positron pair is created. In the energy domain of typical industrial applications (<450 keV), the two dominant processes of interaction are photoelectric effect and Compton scattering.

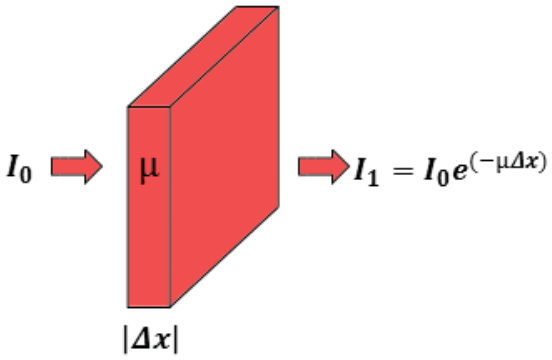

FIGURE 2.4: Lambert-Beer's Law illustration.

X-ray attenuation is characterized by Lambert-Beer's Law and is primarily a function of beam energy and the density and composition of the material of the object being scanned. For a monochromatic X-ray beam of energy E, Lambert-Beer's law gives the beam intensity value I_1 after crossing a thickness Δx of matter as:

$$I_1 = I_0 e^{(-\mu \Delta x)}, \tag{2.2}$$

where I_0 is the initial X-ray intensity and μ is the linear attenuation coefficient of the

penetrated material at energy E (see Fig. 2.4). In the case of multi-material object, several attenuation coefficients are encountered and a more general form of Lambert-Beer's law is given by

$$I_1 = I_0 e^{-\int_0^l \mu(x)dx}, \tag{2.3}$$

with l is the distance traversed by the X-ray beam when penetrating the material. A second point that should be mentioned is the energy dependence E of the attenuation coefficient μ. Thus, with a polychromatic X-ray beam Eqn. (2.3) becomes

$$I_1 = \int_{E_{min}}^{E_{max}} I_0(E) e^{-\int_0^l \mu(E,x)dx} dE, \tag{2.4}$$

where $[E_{min}, E_{max}]$ is the energy spectrum of the X-ray beam. For simplicity, we will neglect the energy dependence and we use Eqn. (2.3) as the basic model for deriving reconstruction algorithms. Consequently, we will reconstruct a mean value of the attenuation coefficient on the energy range of the X-ray beam which can create some beam-hardening artifacts in the reconstructed image.

2.1.3 X-ray Detection

A detector array behind the object and opposite to the X-ray source is used to measure X-ray intensity attenuation. Detectors for X-ray imaging were originally X-ray films but are now mostly replaced by digital detectors. An ideal detector should detect the incident photons of the complete band of X-ray energies efficiently and should have a nearly linear response across a large range of intensities. In practice, the detectors are optimized for certain energy ranges. We can classify the X-ray detectors into two classes: indirect-conversion detectors and direct-conversion detectors. The first ones use indirect technique to convert X-rays into an electric charge, whereas the second ones use direct technique for conversion.

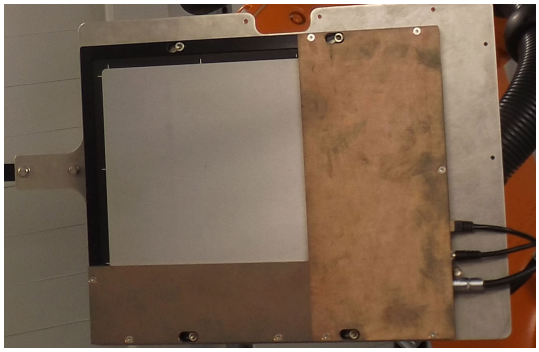

FIGURE 2.5: Flat-panel detector.

Indirect-conversion detectors are a common type and widely available. There are two main components in indirect-conversion detectors: i) scintillator layer which converts the X-ray radiation entering the detector into visible light and ii) photon detector that absorbs the light photons and consequently produces an electric charge which is proportional to the intensity of X-ray radiation. An example of such a detector, which has been used in this work (see Fig. 2.5), is an amorphous silicon-based flat panel detector with a cesium iodide (CsI) scintillator deposed onto an array of photodiodes. Another kind of indirect-conversion detectors use a photon detector that consists of charge-coupled devices (CCDs). These CCD-based detectors use fibre optics to guide the light from the light emitting material (scintillator) to the CCD camera.

Direct-conversion detectors convert X-ray beams into electric charges directly without any light-emitting materials or additional processes as with indirect-conversion systems. Under applied bias voltage, X-ray photons entering the semi-conductor layer like silicon (Si), selenium (Se), gallium arsenide (GaAS), or cadmium telluride (CdTe) lose energy though ionization and are converted to electron-hole pairs. The charges are accumulated and read using thin-film transistor (TFT) arrays which are also used in indirect conversion detectors. Direct-conversion detectors are more efficient than indirect ones and produce images with better quality.

2.2 Mathematical Basics

The mathematical principles of CT were first investigated by Radon in 1917 who proved that the mathematical problem in tomography is an inverse problem whose solution is unique and a two- or three-dimensional object could be reproduced if an infinite number of its projections are available. Radon developed an inversion formula that can reconstruct a function from its line or plane integrals. This formula was first applied to radio astronomy [15] and then to medical imaging including CT.

In this section, we will concentrate only on the Radon-based method to describe the mathematical basics of image reconstruction. For the sake of simplicity, we present only the concept of 2D reconstruction and we consider the case of parallel-beam geometry that was used in first generation systems. A numerical example is presented to illustrate the corresponding theory. For more detailed presentations, we suggest the reader to refer to the books of KaK and Slaney [53] and Natterer [75].

2.2.1 Radon Transform

Mathematically, 2D Radon data refer to the line integrals of the function at different viewing angles. The line integral of a two-dimensional function $f(x, y)$ can be written

as

$$\rho(\beta, t) = \int_{-\infty}^{+\infty} \int_{-\infty}^{+\infty} f(x, y)\delta(x\cos\beta + y\sin\beta - t)dxdy, \tag{2.5}$$

where δ is Dirac delta function, t refers to the perpendicular distance from the origin O to the projection ray with $t = x\cos\beta + y\sin\beta$ and β is the angle between this distance t and the x-axis (see Fig. 2.6).

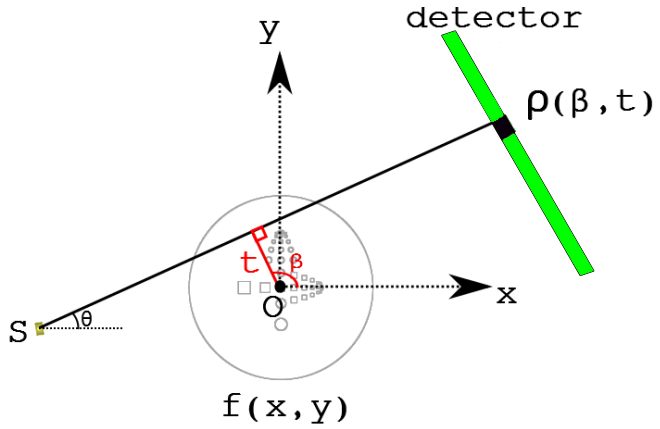

FIGURE 2.6: Line integral illustration.

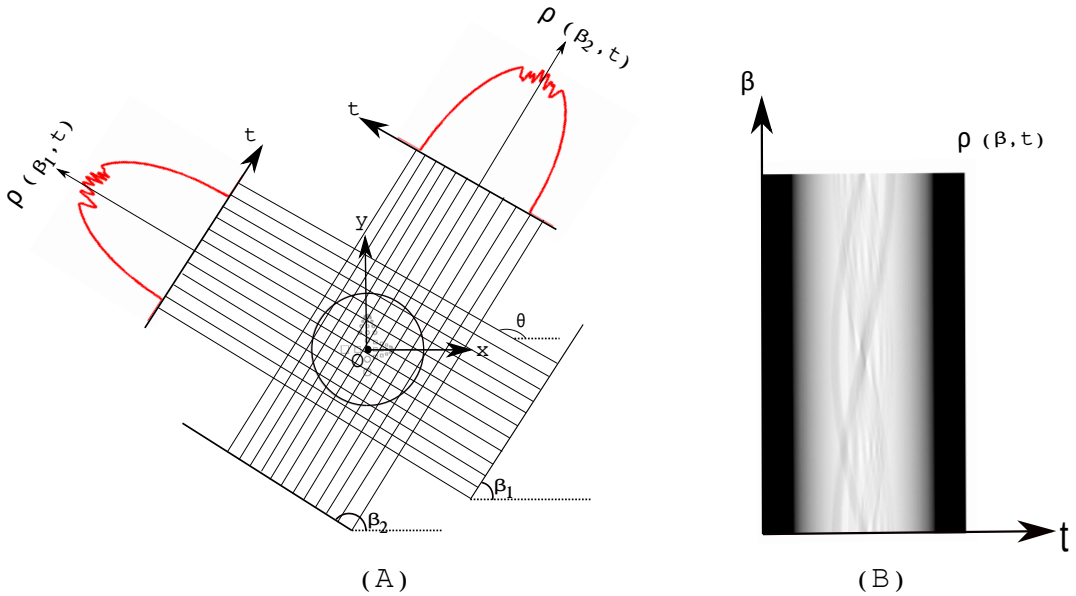

FIGURE 2.7: Illustration of (A) 2D Radon transform and (B) acquired sinogram.

Figure 2.7 (A) shows 2D Radon data which refer to a set of line integrals collected along a series of parallel rays at position t from the origin O and across a viewing angle β that varies from $0°$ to $180°$. These measured line integrals are grouped into an image

called sinogram and displayed in Fig. 2.7 (B). Each row in the sinogram corresponds to a set of line integrals collected across a projection angle β and the aim of CT is to reconstruct function f from this acquired sinogram.

2.2.2 Fourier Slice Theorem

The inversion of the Radon transform is based on the Fourier slice theorem. This theorem relates projection data ρ to object function f where it states that the one-dimensional Fourier transform of a parallel projection of f obtained at angle β is equivalent to a radial line at the same angle in the two-dimensional Fourier transform of f (see Fig. 2.8).

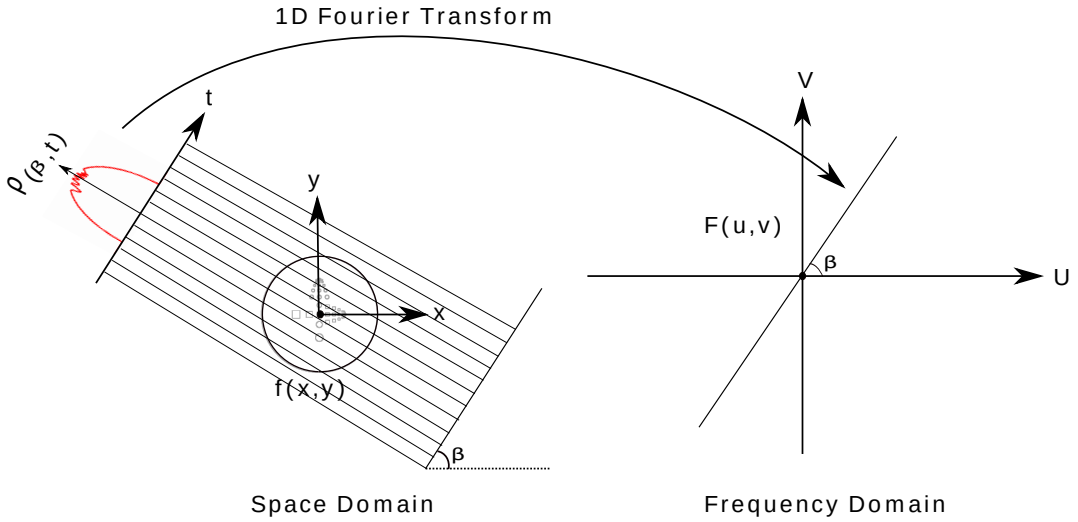

FIGURE 2.8: Illustration of Fourier slice theorem.

Thus, the inversion of Radon transform can be implemented directly using the Fourier slice theorem. The implementation process is summarized by the following steps:

1. Compute a sufficient number of parallel projections $\rho(\beta, t)$ of the object with β varying from $0°$ to $180°$.
2. Calculate the 1D Fourier transform of each of these projections.
3. Use the Fourier slice theorem to get the 2D Fourier transform of the object where the 1D Fourier transform of each projection is related to a line in the 2D Fourier transform of the object.
4. Recover the object by applying a 2D inverse Fourier transform.

In summary, this implementation consists of using a series of 1D Fourier transforms and then applying a 2D inverse Fourier transform. Despite the simplicity of this direct inversion of the Radon transform using the Fourier slice theorem, there are some challenges in practical implementation. The Fourier slice theorem gives us data which correspond to radial lines in the 2D Fourier space and consequently these data are on a polar grid. However, applying the 2D inverse Fourier transform requires samples which fall on a rectangular grid. Thus, interpolation of data in the frequency domain is required to move from polar to Cartesian coordinate. This change between Cartesian and polar coordinates in the frequency domain creates strong artifacts in the reconstruction. For further explanations, we suggest the reader to refer to the book of Jiang Hsieh [44]. As a result, the direct Fourier reconstruction was rarely used and alternative implementations of the Fourier slice theorem were studied. Among these implementations, the most popular one is the filtered back-projection (FBP) algorithm that will be derived and described in the next subsection.

2.2.3 Filtered Back-Projection Algorithm

The filtered back-projection algorithm is one of the most commonly used algorithms for tomographic image reconstruction. As the name implies, there are two steps in the filtered back-projection algorithm: the filtering part, which can be visualized as a simple weighting of each projection in the frequency domain, and the back-projection part which consists of projecting back each view along a line corresponding to the direction in which the projection data were collected.

The derivation of the filtered back-projection algorithm presented here follows the one illustrated in the book of Jiang Hsieh [44]. Given $F(u,v)$ the Fourier transform of $f(x,y)$ with u and v representing two spatial frequencies, the object function $f(x,y)$ may then be obtained from $F(u,v)$ by the inverse Fourier transform:

$$f(x,y) = \int_{-\infty}^{+\infty} \int_{-\infty}^{+\infty} F(u,v) e^{2\pi i(ux+vy)}\, du\, dv. \tag{2.6}$$

Knowing that the Fourier slice theorem relates the parallel projections to object data which are collected in the polar coordinates, we change in Eqn. (2.6) from Cartesian coordinates (u,v) to polar coordinates (β,ω) as follows:

$$\begin{cases} u & = \omega\, \cos\beta \\ v & = \omega\, \sin\beta \\ dudv & = \omega\, d\omega\, d\beta, \end{cases} \tag{2.7}$$

to get

$$f(x,y) = \int_0^{2\pi} d\beta \int_0^{+\infty} F(\omega\cos\beta, \omega\sin\beta) e^{2\pi\omega i(x\cos\beta + y\sin\beta)} \omega d\omega. \tag{2.8}$$

Using the Fourier slice theorem, we substitute $F(\omega\cos\beta, \omega\sin\beta)$ by $P(\beta,\omega)$ (1D Fourier transform of projection $\rho(\beta,t)$) in Eqn. (2.8) to obtain the following relationship:

$$f(x,y) = \int_0^{2\pi} d\beta \int_0^{+\infty} P(\beta,\omega) e^{2\pi\omega i(x\cos\beta + y\sin\beta)} \omega d\omega, \tag{2.9}$$

$$= \int_0^{\pi} d\beta \int_{-\infty}^{+\infty} P(\beta,\omega) e^{2\pi\omega i(x\cos\beta + y\sin\beta)} |\omega| d\omega. \tag{2.10}$$

This Eqn. is the main formula of the filtered back-projection algorithm and can be rewritten in the form

$$f(x,y) = \int_0^{\pi} \rho_r(x\cos\beta + y\sin\beta) d\beta, \tag{2.11}$$

with

$$\rho_r(\beta,t) = \rho_r(x\cos\beta + y\sin\beta) = \int_{-\infty}^{+\infty} P(\beta,\omega)|\omega| e^{2\pi\omega i(x\cos\beta + y\sin\beta)} d\omega. \tag{2.12}$$

As we can see, this algorithm consists of two main steps. The first step (Eqn. (2.12)) is filtering the projections by a kernel whose frequency domain response is $|\omega|$ and known as the ramp filter. Then, these filtered projections ρ_r are back-projected to recover the object function f (Eqn. (2.11)). In practical applications, the ramp filter significantly amplifies the statistical noise existing in the projection data. To minimize this problem, the ramp kernel is usually associated with an apodization window. The most common window functions used are: i) sinc (Shepp-Logan filter), ii) cosine, iii) Hamming and iv) Hanning window functions.

Figure 2.9 shows an example of a filtered back-projection reconstruction from 360 projection views in parallel-beam geometry. Here, the function radon of MATLAB is used to generate Radon data of the object and the function iradon is used to recover the object image by inverting the Radon transform based on the described filtered back-projection algorithm.

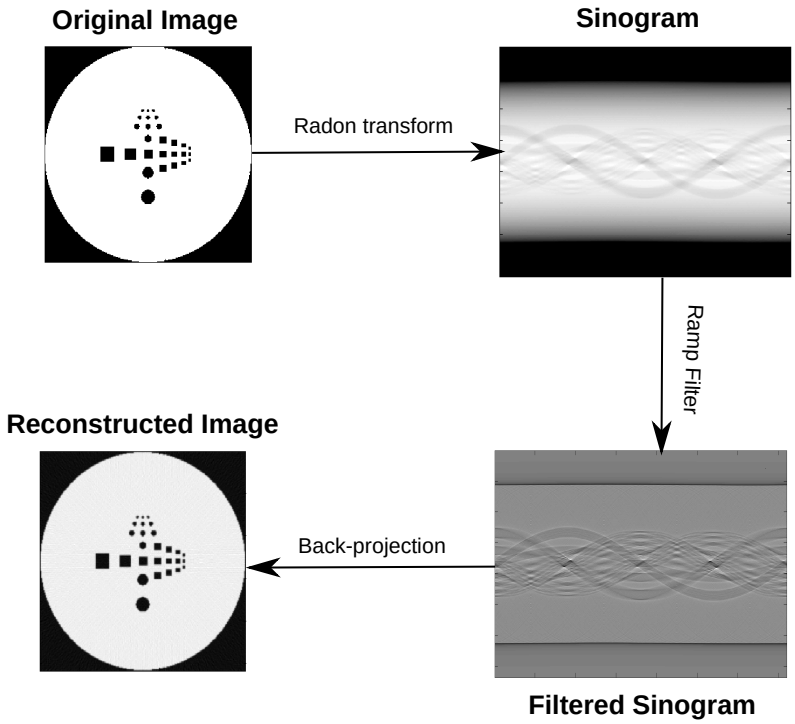

FIGURE 2.9: Example of a FBP reconstruction in 2D parallel-beam geometry.

2.3 Generations of CT Scanners

The evolution of CT scanners can be characterized in seven generations [16]. In the first generation systems illustrated in Fig. 2.10 , one X-ray source (represented in yellow) and one detector (represented in green) are shifted synchronously on opposite sides of the object in order to get the data of one projection view λ. Then, the source-detector system changes its angle of rotation λ for the data acquisition of the next projection data. Thus, a combination of translational and rotational motion is needed to accumulate the transmission measurements required for image reconstruction. This is known as the parallel-beam geometry. For the rotational motion, either the object is rotated between the X-ray source and the detector (mostly in industrial applications) or the source-detector system rotates around the object as the case for medical CT. The data collected by this acquisition geometry are called Radon data and refer to the line integrals along parallel lines at different viewing angle λ which changes from 0 to $180°$.

After the development of the first-generation CT scanners, the main technical advances have been directed toward increasing the speed of data acquisition. Previously, a pencil beam with only a single detector were used in the first-generation scanners. Later developments allowed the collimation of the X-ray beam to a $10°$ fan in the

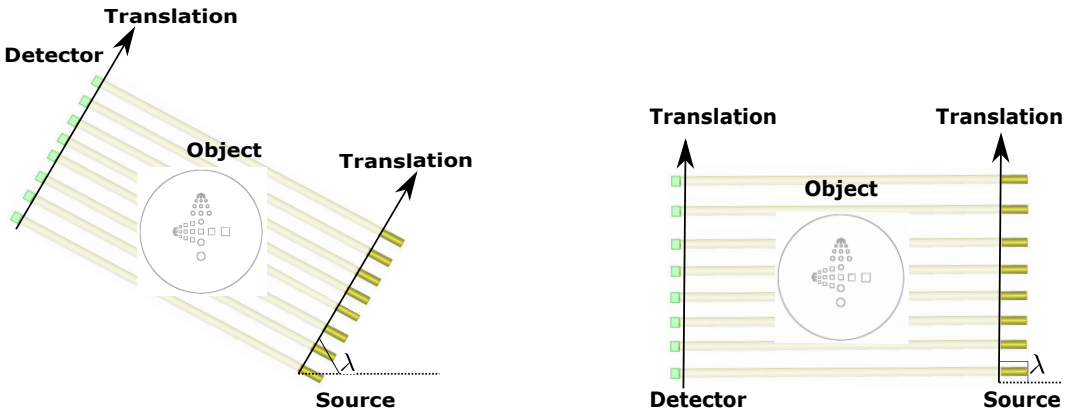

(A) λ = 45° (B) λ = 90°

FIGURE 2.10: Parallel beam scanning geometry.

second-generation systems. Here an array of 8 to 30 detectors can be used rather than a single array (see Fig. 2.11).

FIGURE 2.11: Comparison between first (A) and second (B) generation CT scanners.

In the second-generation CT scanners multiple measures of X-ray transmission can be performed simultaneously and hence the scanning time is reduced. On the other hand, this type of scanners still uses the complicated translation-rotation motion. As a remark, the first- and second-generation systems use only 1D detectors.

The evolution from the second- to the third- generation systems has helped in increasing the acquisition speed more and more. The third-generation scanners which is the most widely used nowadays, use one X-ray source and a segment detector at the opposite side of the object as illustrated in Fig. 2.12a. This system eliminates the necessity of stopping each time for the back-and-forth translation and depends only on rotational motion of the x-ray tube and detector array.

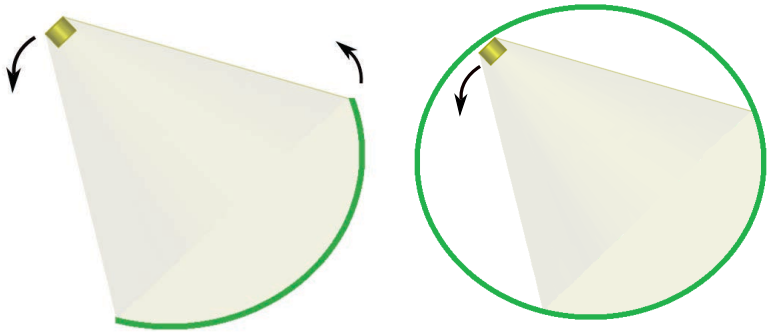

(A) Rotate-rotate generation . (B) Rotate-stationary generation.

FIGURE 2.12: Comparison between third (A) and fourth (B) generation CT scanners.

In the fourth-generation systems the detector is a stationary circular array and the X-ray source rotates around the object (see Fig. 2.12b). However, this technology was later abandoned. The only difference between the third- and fourth-generation scanners was the motion of the detector.

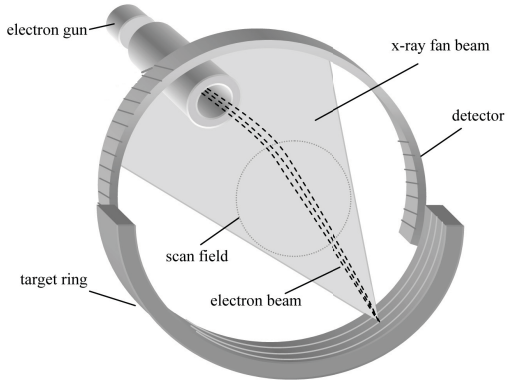

FIGURE 2.13: Fifth-generation CT scanner (figure reproduced from [44]).

The fifth-generation scanners require no mechanical motion for data acquisition where both the X-ray tube and detector are stationary. A simplified schematic diagram of a fifth-generation scanner is represented in Fig. 2.13. It is also named electron beam scanners where a high-speed electron beam is steered along a semicircular tungsten strip anode (bottom 210° arc in Fig. 2.13) which is fixed and surrounds the patient. When the electron beam strikes the anode, a source of X-rays is produced and that rotates due to the sweeping motion of the electron beam. The detector is fixed and represented by the top 216° arc in Fig. 2.13. Electron beam scanner is very fast and therefore it is useful for clinical applications like cardiac imaging. However, there are

limitations of these CT scanners whose architecture is complex and which are more expensive than traditional scanners and demand a considerable amount of space.

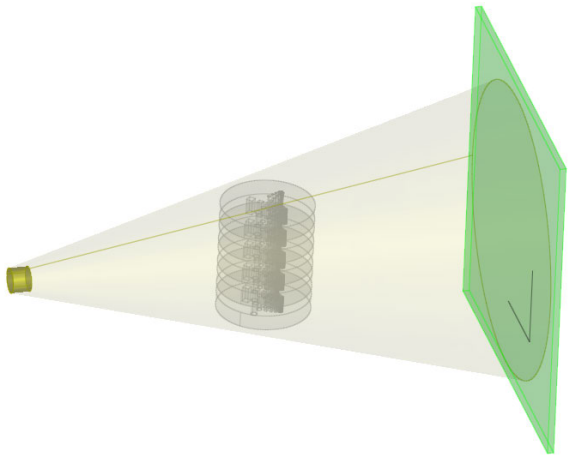

FIGURE 2.14: Cone-beam scanning system.

For third-generation and fourth-generation CT scanners the X-ray source and detector (for third-generation) have to be connected by cables to the rest of the gantry and thus rotation stop and reverse sense has to be performed every $360°$. In the sixth-generation scanners, a slip-ring technology was proposed which passes electrical power to the X-ray source and detector without fixed connections and consequently allows the gantry to rotate continuously without having to stop after each complete rotation. This generation allows helical scanning geometry by translating the object/patient along a table during the continuous rotation of the system source-detector. More details about the helical data acquisition geometry will be introduced in the next subsection.

Finally, technological advances lead to the evolution of the sixth-generation scanners which use single row detectors towards the seventh-generation scanners which use multiple-row detectors and allow helical scanning in cone-beam (CB) geometry. Compared to the conventional fan-beam geometry, CB geometry (see Fig. 2.14) provides faster data collection, higher image resolution, easier hardware implementation and better radiation utilization. However, in a CB geometry the amount of scattered radiation that reaches the detector is larger. In this thesis the CB geometry is considered.

2.4 Data Acquisition Trajectories

Among all the trajectories of data acquisition, the circular one was considered to be the most popular. However, 3D image reconstruction based on a circular trajectory does not satisfy Tuy's data sufficiency condition [109] for an exact three-dimensional

reconstruction, which states that any plane passing through the FOV of the object must intersect the source trajectory in at least one point. Then, recent advances lead to the use of non-standard trajectories like helix, ellipse-line-ellipse, circular-arcs-plus-line, etc. Among them, we are more interested in the helical-like trajectories.

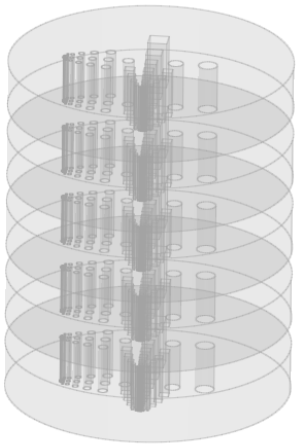

FIGURE 2.15: 3D view of the multi-disk phantom.

Classically CT acquisition is based on a circular trajectory and this is by far the most frequent case in industrial applications. To accomplish such scanning geometry, the system source-detector can be held fixed while the object is rotated around an axis as this is the case for industrial applications. Alternatively, this can be achieved by a continuous rotation of the system source-detector around the object or patient which stays stationary as this is the case for clinical CT scanners. This trajectory is a technically simple CT configuration and ensures an exact reconstruction only in the central plane of the object. However, when inspecting long objects and due to data insufficiency this scanning geometry creates severe artifacts in the reconstruction. These artifacts would become more serious when the cone angle is large.

The multi-disk phantom illustrated in Fig. 2.15 is a test object which demonstrates the limitations of the circular trajectory. We can see in Fig. 2.16 that this scanning geometry gives good reconstruction in the horizontal central slice (Fig. 2.16c), whereas important artifacts appear in the upper and lower slices (Fig. 2.16b). For this reason, more advanced CT scanning methods have been proposed to handle this aspect known as the long-object problem.

Helical data acquisition was proposed in 1989 [54] as a solution to deal with long objects. Since its invention, this scanning geometry has been extensively studied and

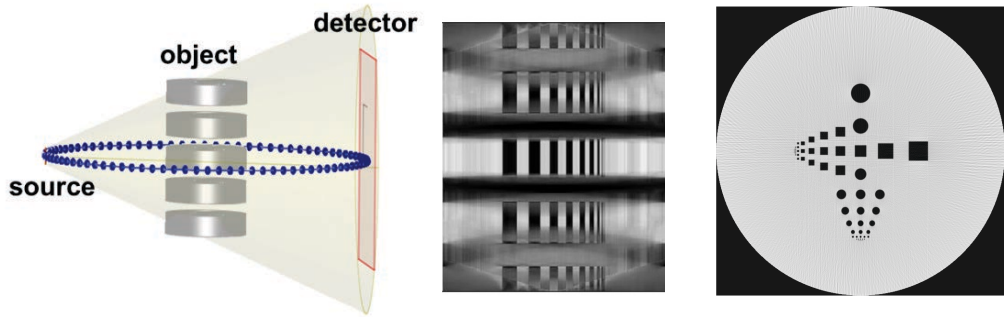

(A) Scanning geometry (B) Vertical slice (C) Horizontal slice

FIGURE 2.16: FDK reconstruction of the multi-disk phantom from circular scanning geometry.

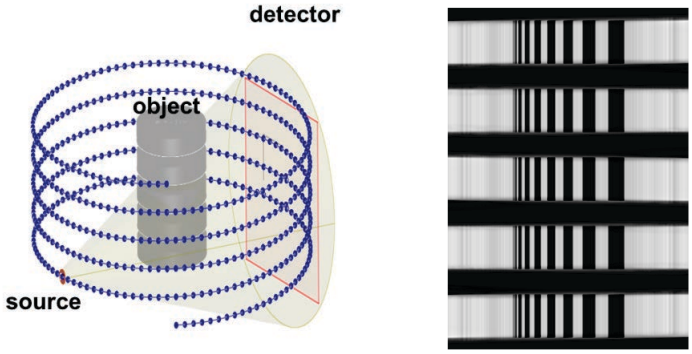

(A) Scanning geometry (B) Vertical slice

FIGURE 2.17: FDK reconstruction of the multi-disk phantom from helical scanning geometry.

has become very interesting because it satisfies Tuy's condition and can collect data sufficient for an exact reconstruction of the object. In helical CB scan, the system source-object rotates while the inspected object is translated along the direction of the rotational axis. Fig. 2.17 illustrates the reconstruction of the multi-disk phantom using a helical trajectory. It is clear that the artifacts shown previously are suppressed within this acquisition geometry. As a remark, the illustrated reconstruction results are obtained with our implemented circular and helical FDK algorithms and that will be explained in details in the next chapter.

In 2008, the reverse helical trajectory was proposed for linear-accelerator (LINAC) mounted CT systems [19]. The direction of rotation is the only difference between classical and reverse helical trajectory. In contrast to classical helical trajectory whose direction of rotation is constant, reverse helical trajectory changes its direction of rotation between clock-wise and anti-clockwise each time the rotation angle has reached a maximum value defined as λ_m which represents the angular range of the helix. When

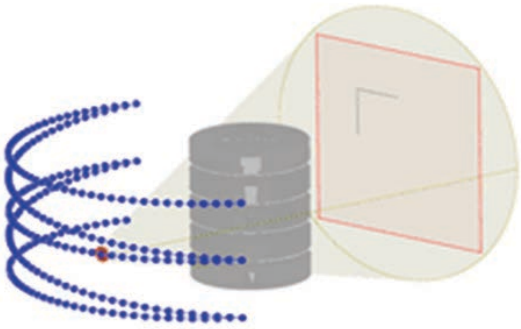

FIGURE 2.18: Limited-angle reverse helical scanning geometry.

$\lambda_m \leq 2\pi$ we refer to this trajectory as limited-angle reverse helical trajectory and an example of such a trajectory with $\lambda_m = 210°$ is illustrated in Fig. 2.18 .

2.5 Incomplete Projection Data

In certain industrial applications, it is not possible to obtain complete projection data due to some constraints during data acquisition. These missing data will affect the quality of the reconstructed image. Incomplete projection data have been classified into three main categories [20]: truncated data, limited-angle data and few-view data.

2.5.1 Truncated Data

When dealing with X-ray inspection of large industrial objects, we are generally interested in the 3D reconstruction of a region-of-interest (ROI) potentially containing flaws or other features rather than on the reconstruction of the whole object. This local reconstruction is related to a reduction in the field-of-view which consequently truncates the projections during data acquisition and produces severe artifacts when using conventional algorithms of reconstruction. Fig. 2.19b shows an example where the object size is too large compared with the dimensions of the detector. Thus, the detector is not large enough to contain the CB projections of the object and therefore the projections are truncated.

It was demonstrated by [20] that this aspect known as interior problem does not have a unique solution. Thus, exact reconstruction from truncated projection data is complicated and may even be impossible in certain situations. In fact, the obtained projections may be truncated in two basic manners either transversely or axially. An efficient solution for handling axial truncation is the use of a helical scanning geometry.

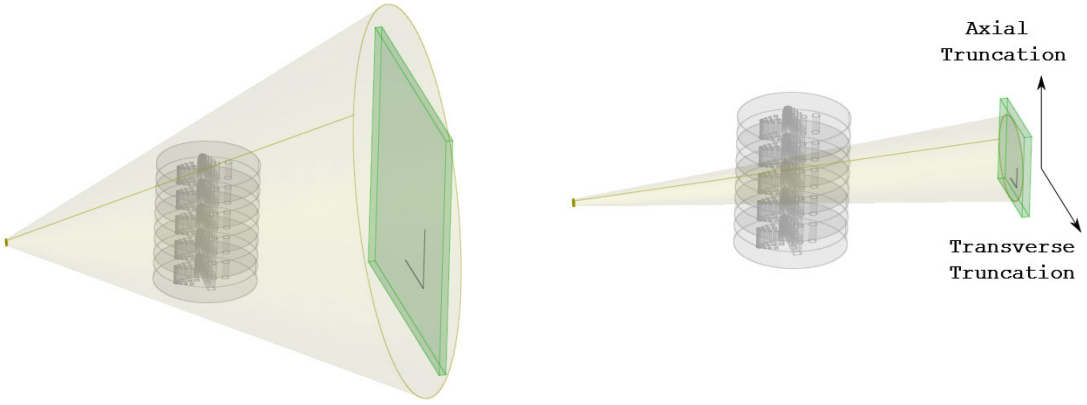

(A) Complete data (B) Truncated data

FIGURE 2.19: Illustration of data truncation.

To deal with transversely truncated data, different techniques have recently been developed. We will give in Chapter 4 a more detailed overview of some existing methods that can handle transverse truncation.

2.5.2 Limited-angle Data

Limited-angle data refers to the situation where projection data are acquired at limited angular range. An example of this aspect is shown in Fig. 2.20. Due to its missing projection data, limited-angle data can significantly degrade the quality of the reconstructed image especially when the acquired projection data are highly incomplete. Conventional reconstruction methods including both analytical and iterative algorithms do not perform well and some artifacts are inevitable. It was recently stated [20] that reconstructing an object from limited-angle data is a process that is severely ill-posed or unstable. The inversion process is not continuous and an error in the measurements can cause instability everywhere in the reconstructed object.

To deal with limited-angle data, various methods have been proposed. The first achievement was the half-scan fan-beam which corresponds to π plus the opening angle of the fan. A weighting function to handle redundant data in case of a half-scan fan-beam reconstruction was introduced [87]. Later, 2D and 3D reconstruction methods with fan-beam and CB projections, respectively, on less than a short scan were developed [79, 62]. We show in Chapter 5 an FDK-type algorithm for reconstruction on a limited-angle reverse helical trajectory. Also, two efficient iterative algorithms for limited-angle data will be presented.

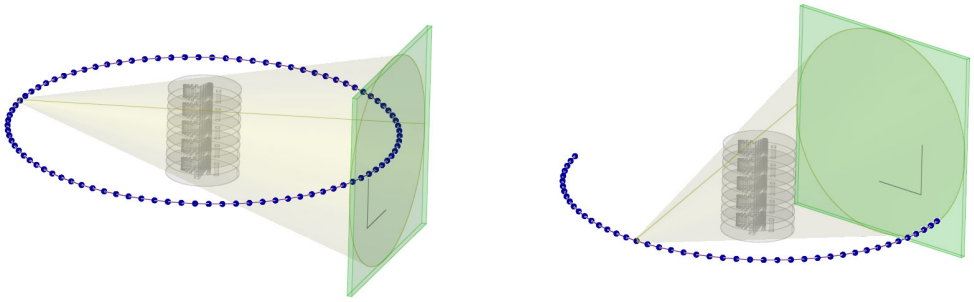

(A) complete-angle data (B) limited-angle data

FIGURE 2.20: Illustration of limited-angle data.

2.5.3 Few-view Data

Few-view CT refers to CT in which the measured number of projections is reduced significantly. This accelerates the inspection time and increases equipment life cycles. Sparse-view CT is considered as an ill-posed inverse problem. Due to insufficient sampling, the number of projections does not satisfy the Nyquist sampling theorem and as a result FBP algorithms produce streak artifacts. Iterative reconstruction methods like total variation based compressed sensing algorithms [95] have been proposed for reconstruction from a reduced number of projections. These algorithms are based on assumption of image sparsity in the image gradient domain and aims to minimize the total variation (TV). This technique of minimizing the TV of the image has been used in our proposed iterative algorithms for reconstruction from a small number of projections.

We have addressed in this chapter the fundamental principles of CT including both physical and mathematical basics, the different generations of CT scanners, some of the common data acquisition trajectories and the types of missing data. Now, we will discuss in the following chapter analytical and iterative CB reconstruction algorithms for scanning trajectories which are more advanced than the classical circular trajectory.

Chapter 3

Existing Analytical and Iterative Reconstruction Algorithms for Non-Standard Trajectories

Image reconstruction algorithms are classified into two major categories: analytical and iterative reconstruction. As the name suggests, analytical algorithms are based on inversion formulas which are derived analytically. On the other hand, iterative algorithms define a system of equations describing the CT process and aim to solve this system in an iterative manner.

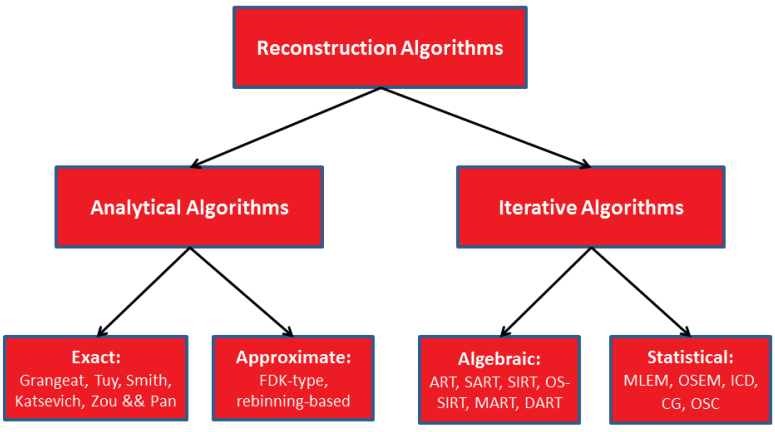

FIGURE 3.1: Overview of some prominent reconstruction algorithms.

This chapter is intended as an overview of both analytical and iterative reconstruction algorithms for non-standard trajectories. For analytical reconstruction, we review two kinds of algorithms: exact and approximate. This latter is divided into FDK-type and rebinning-based algorithms. Iterative algorithms are also classified into two categories: algebraic and statistical methods. A general overview of iterative algorithms is presented in this chapter with more focus on algebraic principles rather than statistical

models. Finally, some general conclusions regarding the advantages and disadvantages of each approach are stated. These different prominent reconstruction algorithms that will be presented in this chapter are illustrated in Fig. 3.1.

3.1 Approximate Analytical Algorithms for Helical Trajectory

In this section, we first show an overview of various approximate analytical algorithms developed for helical trajectory and more general scanning geometries. Then, we describe the helical scanning geometry and we introduce the different notations used throughout the reconstruction inversion formulas. Finally, we illustrate the steps performed in the helical FDK algorithm.

3.1.1 Related Work

Approximate CB reconstruction algorithms are roughly divided into two main classes: rebinning-based algorithms and FDK algorithms. Rebinning-based algorithms [29] are based on separating the 3D reconstruction into a set of 2D reconstructions. These algorithms involve two main steps:

(a) Rebinning process which rearranges the CB data into a set of 2D fan-beam or parallel-beam data.

(b) 2D filtered back-projection reconstruction of the rebinned data.

In the rebinning step, a number of slices in the object are selected, and then a sinogram which corresponds to each slice is chosen from the acquired CB data. The chosen slices can be planar or non-planar. Noo et al. [76] developed a rebinning-based helical reconstruction algorithm with each chosen slice is orthogonal to the axis of rotation of the helix. A more accurate rebinning step of this algorithm was proposed later and that is based on choosing tilted slices instead of these transaxial slices [49, 92].

The second type of methods is based on the FDK algorithm [35] which is one of the most commonly used algorithms due to its high efficiency and simplicity. This algorithm is a heuristic extension of the exact fan-beam reconstruction and was developed initially for reconstruction on a circular trajectory and then extended for a large family of general scanning trajectories including the helical one [113]. An advantage of FDK-type algorithms is their flexibility where they can be adapted to incomplete scanning trajectories like the half-scan geometry [114, 77]. The FDK algorithm [35, 113] and its variants [59, 120, 102, 106] are used extensively in current commercial scanners.

FDK algorithm was extended to the helical trajectory with variable pitch [143]. It should be mentioned that efforts have been made to improve the reconstruction accuracy of the helical FDK algorithm. For example, the 1D row-wise filtering step of

the standard helical FDK algorithm was replaced by a 1D rotational filtering across the detector [103]. In addition, a new redundancy weighting scheme that can improve noise characteristics has been proposed [99]. Furthermore, view weighting strategies that use redundant data have been proposed and that give better reconstruction results over larger cone angle and helical pitch [105, 107, 104]. Half-scan helical FDK algorithm has been improved by developing an algorithm that reconstruct images in nutated surfaces formed by a family of PI-lines [46]. The concept of PI-lines will be explained in the next section.

3.1.2 Helical Data Acquisition Geometry and Associated Notations

Consider a 3D object of attenuation function $f(\overrightarrow{r})$ where $\overrightarrow{r}$ is the position vector of a point M located in the object. The coordinates of M in the fixed coordinate system of the object $(\overrightarrow{e}_x, \overrightarrow{e}_y, \overrightarrow{e}_z)$ are given by (x, y, z). The actual support of the object is confined within a cylinder of radius r and central axis along the z-direction. Thus, we have

$$f(\overrightarrow{r}) = 0 \qquad \text{for} \qquad x^2 + y^2 > r^2. \tag{3.1}$$

As illustrated in Fig. 3.2, the X-ray source S moves on a helical trajectory of radius R. The coordinates of S in the system $(\overrightarrow{e}_x, \overrightarrow{e}_y, \overrightarrow{e}_z)$ are denoted by

$$\overrightarrow{y}(\lambda) = (R\cos\lambda, R\sin\lambda, h\lambda), \qquad \lambda \in [\lambda_{min}, \lambda_{max}]. \tag{3.2}$$

λ_{min} and λ_{max} are the endpoints of the rotation angle λ and $2\pi h$ is the helical pitch which represents the axial translation distance of the source during one complete rotation. A two-dimensional detector is placed at a distance D from the source with its axes defined by the unit vectors $\overrightarrow{e}_u$ and $\overrightarrow{e}_v$. O_d is the origin of the detector and defined by the orthogonal projection of S onto the detector. The unit vector joining O_d and S is given by $\overrightarrow{e}_w$. The expressions of the three unit vectors $\overrightarrow{e_u}(\lambda)$, $\overrightarrow{e_v}(\lambda)$ and $\overrightarrow{e_w}(\lambda)$ in the coordinate system $(\overrightarrow{e_x}, \overrightarrow{e_y}, \overrightarrow{e_z})$ are:

$$\begin{cases} \overrightarrow{e_u}(\lambda) = (-\sin\lambda)\overrightarrow{e_x} + (\cos\lambda)\overrightarrow{e_y} \\ \overrightarrow{e_v}(\lambda) = \overrightarrow{e_z} \\ \overrightarrow{e_w}(\lambda) = (\cos\lambda)\overrightarrow{e_x} + (\sin\lambda)\overrightarrow{e_y}. \end{cases} \tag{3.3}$$

The projection of a point M on the detector is defined by the coordinates (u_d, v_d) (see Fig. 3.2). The measured projection data are given by

$$P(\overrightarrow{\theta}, \lambda) = \int_{l=0}^{+\infty} f(\overrightarrow{y}(\lambda) + \overrightarrow{\theta}\, l)dl, \tag{3.4}$$

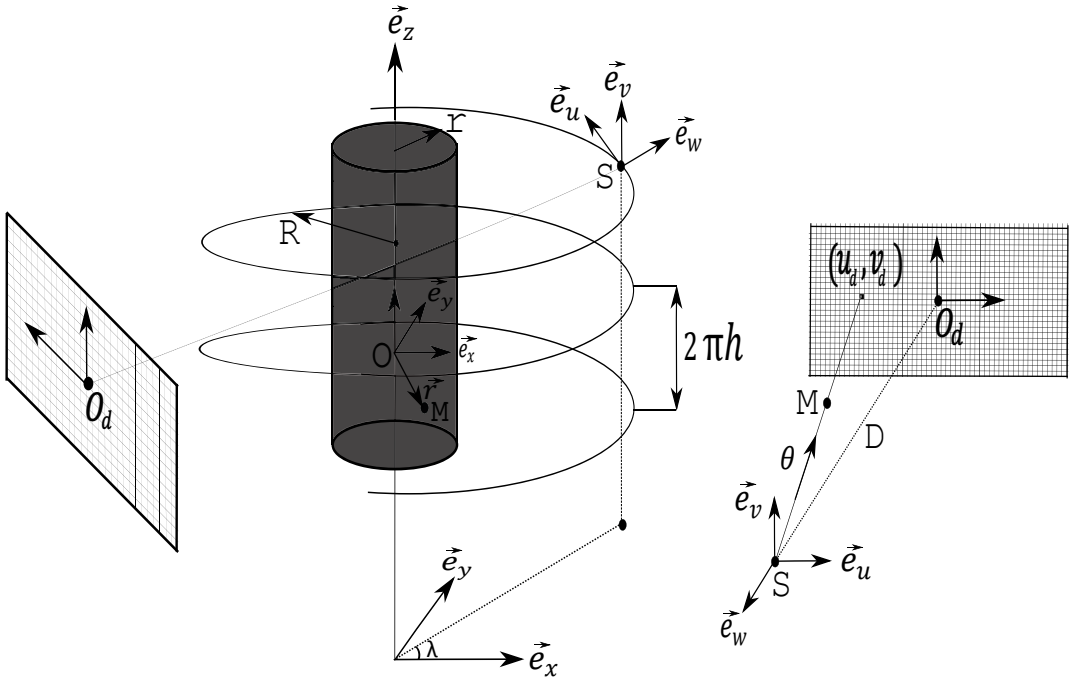

FIGURE 3.2: Helical CB acquisition geometry and associated notations.

where $\overrightarrow{\theta}(u_d, v_d, \lambda)$ is the unit vector of the X-ray emitted from the source point S of rotation angle λ and crossing the detector at the point of coordinates (u_d, v_d). $P(\overrightarrow{\theta}, \lambda)$ can be written as a function of (u_d, v_d):

$$P(\overrightarrow{\theta}, \lambda) = P(u_d, v_d, \lambda), \tag{3.5}$$

where

$$u_d\overrightarrow{e_u}(\lambda) + v_d\overrightarrow{e_v}(\lambda) - D\overrightarrow{e_w}(\lambda) = A(u_d, v_d)\overrightarrow{\theta} \quad \text{and} \quad A(u_d, v_d) = \sqrt{u_d^2 + v_d^2 + D^2}. \tag{3.6}$$

Based on Eq. (3.6), the projection position (u_d, v_d) of a point $M(x, y, z)$ is expressed as

$$\begin{cases} u_d = D\left(\frac{x\sin\lambda - y\cos\lambda}{x\cos\lambda + y\sin\lambda - R}\right) \\ v_d = -D\left(\frac{z - h\lambda}{x\cos\lambda + y\sin\lambda - R}\right). \end{cases} \tag{3.7}$$

3.1.3 FDK Algorithm

The FDK algorithm is of filtered-back-projection (FBP) structure that consists of three main steps:

(a) Cosine weighting of projections (Eq. (3.10)).

(b) Row-wise ramp filtering of weighted projections (Eq. (3.9)).

(c) Back-projection of the filtered data (Eq. (3.8)).

Its inversion reconstruction formula assuming helical trajectory can be expressed as

$$f(\overrightarrow{r}) = \int_{\lambda_i}^{\lambda_f} \frac{RD}{|R - \overrightarrow{r} \cdot \overrightarrow{e_w}(\lambda)|^2} P_R(u_d, v_d, \lambda)\, d\lambda, \tag{3.8}$$

where $\lambda_i = \frac{z}{h} - \pi$, $\lambda_f = \frac{z}{h} + \pi$ and $P_R(u_d, v_d, \lambda)$ are the ramp-filtered data given by

$$P_R(u_d, v_d, \lambda) = \int_{-\infty}^{+\infty} h_r(u_d - u'_d) P'(u'_d, v_d, \lambda)\, du'_d. \tag{3.9}$$

In this equation, h_r represents the ramp filter kernel and P' refers to the weighted projection data

$$P'(u_d, v_d, \lambda) = \frac{D}{\sqrt{D^2 + u_d^2 + v_d^2}} P(u_d, v_d, \lambda). \tag{3.10}$$

It should be mentioned that the ramp filter is global and thus filtering any point in the 2D projection matrix requires a complete knowledge of the projections away from that point at the same lateral position. When projections are truncated transversely, this condition is not satisfied and as a result the filtering step is not performed correctly which produces significant artifacts in the reconstructed image.

3.2 Exact Analytical Algorithms for Helical Trajectory

This section provides an overview of proposed exact reconstruction algorithms for helical scanning trajectory. Among them, we identified three algorithms and we show their structure and inversion formulas. The notions of PI-lines, long-object problem and Tam-Danielsson window are introduced also.

3.2.1 Related Work

Approximate reconstruction algorithms can no longer perform well when the cone angle is sufficiently large. Thus, great efforts have been made to derive an exact analytical inversion formula that can yield accurate reconstruction even for very large values of the cone-angle. As the name implies, an exact reconstruction algorithm aims to find an analytical solution that matches the object function in mathematical precision. Kudo et al. [60] developed a helical CB algorithm based on the Grangeat's theorem [41] that relates the CB projections to the 3D Radon transform of the object function. However, this algorithm does not deal with the long-object problem. As defined by [28], the long-object problem in helical CT is the problem of reconstructing a ROI of a long object using axially truncated CB projections. Several Radon-based algorithms that solve

the long-object problem have been developed [28, 89, 100, 58, 91]. Based on the theories of Tuy [109] and Smith [97], other exact CB inversion formulas were developed also [98, 141].

Although the previous mentioned algorithms are based on exact inversion formulas, they are not attractive due to their high computational cost where the filtering operation involved is usually shift-variant. In 2002, the first theoretically exact filtered-backprojection reconstruction formula for helical CT was proposed by Katsevich [56]. This algorithm is based on the concept of PI-lines and can handle longitudinally truncated data. It should be stated that the PI-lines concept was essential for the development of several helical reconstruction algorithms. Implementation details on the algorithm of Katsevich for the flat and curved detector geometry have been demonstrated [132, 78]. Recently, Katsevich's algorithm was accelerated on cluster and using graphics processing unit (GPU) [32, 122, 119].

Based on Katsevich's work, a filtered-backprojection (FBP) and back-projection filtration (BPF) algorithms that reconstruct the image over PI-lines in helical cone-beam CT were proposed by Zou and Pan [149, 150]. In general, a FBP algorithm consists of two steps. Firstly, the differentiated projection data are filtered. Secondly, these filtered data are back-projected in order to reconstruct the image. The structure of the BPF algorithm differs from the FBP one in the sense that it performs the back-projection operation before the filtering step. The back-projection filtration (BPF) or differentiated back-projection (DBP) algorithm of Zou and Pan is based on computing the back-projection of a derivative of the projection data and then applying a finite inverse Hilbert transform along the PI-lines.

Katsevich's algorithm and the two algorithms of Zou and Pan were generalized for reconstruction on more flexible scanning curves like a saddle curve or a non-standard helix with a variable radius and pitch [57, 133, 123, 127, 125, 145, 152, 135, 83, 84, 85, 121, 144, 134, 151]. Tingliang et al. [147] extended the BPF algorithm of Zou and Pan for reconstruction on any general trajectory satisfying Tuy's data sufficiency condition [109].

Local exact helical reconstruction algorithms [30, 126, 124] that can handle transversely truncated data were proposed based on the BPF algorithm of Zou and Pan. These algorithms combine the differentiated back-projection relation with a result on the inversion of the truncated Hilbert transform. This latter can be achieved algebraically using a singular value decomposition (SVD) or based on the projection onto the convex sets (POCS) method [129]. It was proved that exact and stable inversion of the truncated Hilbert transform along a segment would be possible aided by partial knowledge on small subregion of that segment.

3.2.2 PI-lines Concept

For a point M of position vector $\vec{r}$, a PI-line (dotted line passing in Fig. 3.3) is a line segment passing through M and intersecting the helix at two points $\vec{y}(\lambda_i)$ and $\vec{y}(\lambda_o)$ such that $|\lambda_o - \lambda_i| \leq 2\pi$. That is to say that $\vec{y}(\lambda_i)$ and $\vec{y}(\lambda_o)$ are separated by less than one helical turn. The portion within the helix that joins the two extremities of the PI-line is called the PI-line helix segment. Every point inside the helix belongs to one and only one PI-line [24, 61]. An important feature of the helical trajectory is that for each point whose PI-line is specified by $\vec{y}(\lambda_i)$ and $\vec{y}(\lambda_o)$, the PI-line helix segment defines a complete coverage of the point and should be sufficient for an exact reconstruction of that point. This explains the exact reconstruction on PI-line segments.

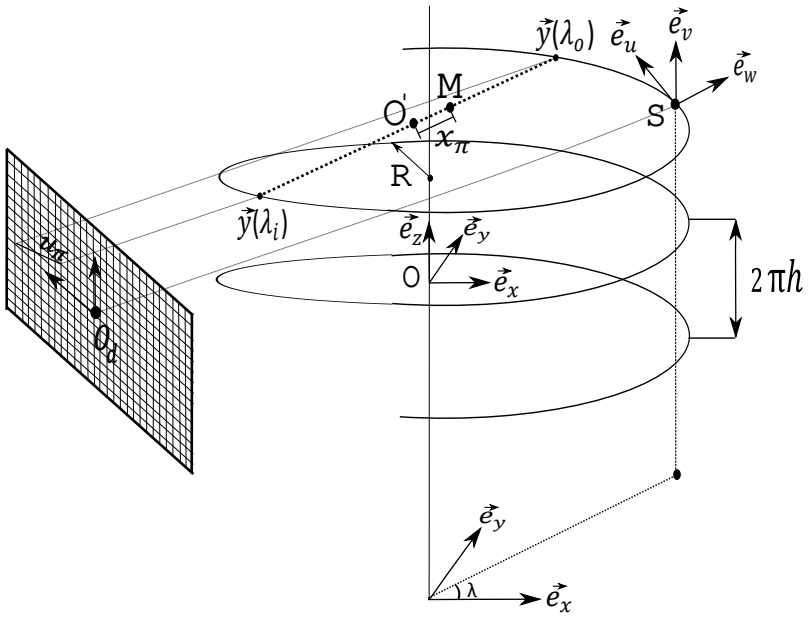

FIGURE 3.3: Illustration of PI-lines concept.

Defrise et al. [28] have related the coordinates (x, y, z) of a point M in the fixed system of the object to its indices $(t, \lambda_i, \lambda_o)$ by

$$\begin{cases} x = R[(1-t)\cos\lambda_i + t\cos\lambda_o] \\ y = R[(1-t)\sin\lambda_i + t\sin\lambda_o] \\ z = \frac{h}{2\pi}[(1-t)\lambda_i + t\lambda_o], \end{cases} \tag{3.11}$$

where the parameter t $\in [0, 1]$ defines x_π the position of M on the PI-line of extremities λ_i and λ_o through the expression

$$x_\pi = (t - 1/2)|\vec{y}(\lambda_o) - \vec{y}(\lambda_i)|. \tag{3.12}$$

In particular, x_π represents the abscissa of M on the axis directed along the PI-line and whose origin O' is located at the midpoint of this PI-line. Therefore, we get a new PI-line coordinate system $(x_\pi, \lambda_i, \lambda_o)$. In the next chapter, two notations will be used to characterize the attenuation function of the reconstructed 3D object, depending on the coordinate system we consider. This function will be denoted by $f_\pi(x_\pi, \lambda_i, \lambda_o)$ in the PI-line system and by $f(x, y, z)$ in the fixed coordinate system of the object. We also define two approaches of numerical implementation known as voxel-based implementation and PI-line-based implementation. The voxel-based implementation aims at obtaining the function $f(x, y, z)$ directly from the computed projections. On the other hand, the PI-line-based implementation gets firstly $f_\pi(x_\pi, \lambda_i, \lambda_o)$ and then obtains $f(x, y, z)$ through a 3D interpolation on f_π.

3.2.3 Long-object Problem and Tam-Danielsson Window

Based on the concept of PI-lines, it was proven that for a given rotation angle λ, the region Γ (see Fig. 3.4) in the detector bounded by Γ^+ and Γ^-, the projections of the upper and lower turns of the helix, respectively, represents the minimum data set required for an exact reconstruction of a point inside the helix [101, 24]. This region is known as the Tam-Danielsson window. It can be observed that any point on the boundaries Γ^+ and Γ^- belongs to a PI-line (dotted lines in Fig. 3.4) connecting $\overrightarrow{y}(\lambda)$ with another vertex on the helix turns located above and below $\overrightarrow{y}(\lambda)$.

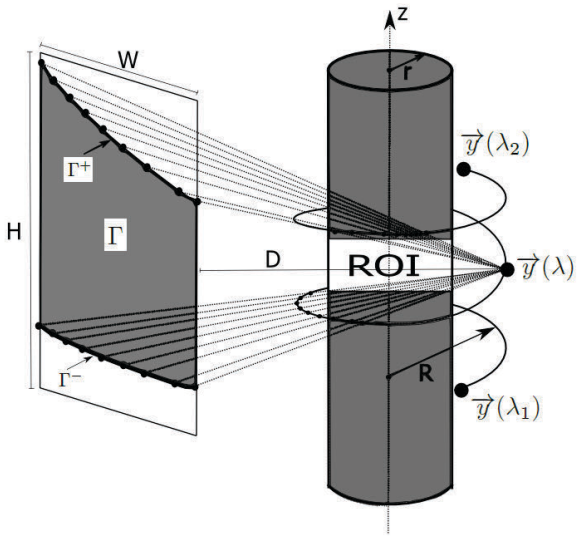

FIGURE 3.4: Illustration of Long-object problem and Tam-Danielsson window.

Thus, the minimum width W and height H of the needed detector for an exact reconstruction are denoted by

$$\mathrm{W} = 2\left(\frac{D\sin\Delta}{1-\cos\Delta}\right) \tag{3.13}$$

and

$$\mathrm{H} = 2\left(\frac{Dh(2\pi-\Delta)}{R(1-\cos\Delta)}\right) \tag{3.14}$$

with

$$\Delta = 2\cos^{-1}(\frac{r}{R}). \tag{3.15}$$

The key benefit of the Tam-Danielsson detection geometry is that it allows to solve the long-object problem. This problem is defined as reconstructing the ROI (white region in Fig. 3.4) bounded by the two trans-axial slices with a helical scan of endpoints defined by $\overrightarrow{y}(\lambda_1)$ and $\overrightarrow{y}(\lambda_2)$. The significant property of this helical scan is that it covers the ROI and its immediate vicinity only and does not require to cover the whole axial extent of the object for the reconstruction of the considered ROI.

3.2.4 Description of Three Exact Helical Reconstruction Algorithms

This subsection describes three exact algorithms for reconstruction on a helical trajectory: i) FBP algorithm of Katsevich [56], ii) FBP algorithm of Zou and Pan [150] and iii) BPF algorithm of Zou and Pan [149]. The inversion formula of each algorithm is demonstrated.

FBP Algorithm of Katsevich

The algorithm of Katsevich [56] consists of first computing the first derivative of CB projections $P(\overrightarrow{\theta},\lambda)$ with respect to λ. Secondly, these differentiated CB projections are filtered using the kernel $(1/\sin\gamma)$:

$$P^F(\overrightarrow{\theta},\lambda) = \int_0^{2\pi} \frac{\partial}{\partial q} P(\cos(\gamma)\overrightarrow{\theta} + \sin(\gamma)\overrightarrow{e}(\overrightarrow{\theta},\lambda), q)|_{q=\lambda} \frac{1}{\sin\gamma} d\gamma, \tag{3.16}$$

where $\overrightarrow{e}(\overrightarrow{\theta},\lambda)$ is a unit vector perpendicular to $\overrightarrow{\theta}$ (refer to [56] for more details on the choice of $\overrightarrow{e}(\overrightarrow{\theta},\lambda)$) . Finally, the filtered data $P^F(\overrightarrow{\theta},\lambda)$ are back-projected to recover the attenuation function $f(\overrightarrow{r})$ as follows:

$$f(\overrightarrow{r}) = -\frac{1}{2\pi^2}\int_{\lambda_i(\overrightarrow{r})}^{\lambda_o(\overrightarrow{r})} \frac{1}{|\overrightarrow{r}-\overrightarrow{y}(\lambda)|} P^F\left(\frac{\overrightarrow{r}-\overrightarrow{y}(\lambda)}{|\overrightarrow{r}-\overrightarrow{y}(\lambda)|},\lambda\right) d\lambda. \tag{3.17}$$

As illustrated in Eq. (3.17), the back-projection operation is performed over the helix segment of endpoints $\lambda_i(\overrightarrow{r})$ and $\lambda_o(\overrightarrow{r})$, the lower and upper bounds of the unique PI-line passing through the point of position $\overrightarrow{r}$.

FBP Algorithm of Zou and Pan

The FBP algorithm of Zou and Pan [150] consists of first computing the modified differentiated projections $\widehat{P}(u_d, v_d, \lambda)$ expressed as

$$\begin{aligned}\widehat{P}(u_d, v_d, \lambda) &= \left[\frac{d\overrightarrow{y}(\lambda)}{d\lambda}.\overrightarrow{e}_u(\lambda)\right] A(u_d, v_d)\frac{dP(u_d, v_d, \lambda)}{du_d} - \left[\frac{d\overrightarrow{y}(\lambda)}{d\lambda}.\overrightarrow{\theta}\right] P(u_d, v_d, \lambda) \\ &+ \left[\frac{d\overrightarrow{y}(\lambda)}{d\lambda}.\overrightarrow{e}_v(\lambda)\right] A(u_d, v_d)\frac{dP(u_d, v_d, \lambda)}{dv_d},\end{aligned} \tag{3.18}$$

where $P(u_d, v_d, \lambda)$ represents the projection data in terms of the coordinates (u_d, v_d) and $\overrightarrow{\theta}$ is the unit vector that joins the point of position $\overrightarrow{r}$ with its projection on the detector defined by the coordinates (u_d, v_d).

Secondly, these differentiated CB projections are filtered (Hilbert integral over u'_π in Eqn. (3.19)) and then backprojected (integral over λ in Eqn. (3.19)) along the helix segment of extremities λ_i and λ_o to obtain the attenuation function $f(\overrightarrow{r})$ as follow

$$\begin{aligned}f(\overrightarrow{r}) &= -\frac{1}{2\pi^2}\int_{\lambda_i(\overrightarrow{r})}^{\lambda_o(\overrightarrow{r})}\left(\frac{A^2(u_d, v_d)}{|\overrightarrow{r} - \overrightarrow{y}(\lambda)|^2}\right)d\lambda \int_{\mathbb{R}}\left(\frac{\widehat{P}(u'_d, v'_d, \lambda)}{(u_\pi - u'_\pi)A^2(u'_d, v'_d)}\right)du'_\pi \\ &-\frac{1}{2\pi^2}\left[\frac{A(u_d, v_d)}{|\overrightarrow{r} - \overrightarrow{y}(\lambda)|}\int_{\mathbb{R}}\left(\frac{P(u'_d, v'_d, \lambda)}{(u_\pi - u'_\pi)A(u'_d, v'_d)}\right)du'_\pi\right]_{\lambda_i(\overrightarrow{r})}^{\lambda_o(\overrightarrow{r})},\end{aligned} \tag{3.19}$$

where u_π-axis is along the projection of the PI-line with extremities $\lambda_i(\overrightarrow{r})$ and $\lambda_o(\overrightarrow{r})$ onto the detector (see Fig. 3.3).

BPF Algorithm of Zou and Pan

Another approach of reconstructing the object from its CB projections collected along a helical trajectory was also proposed by Zou and Pan [149]. The structure of this exact algorithm is differentiated back-projection with Hilbert post-filtering. This alternative algorithm which we refer to as the back-projection-filtration algorithm reconstructs the image by first back-projecting the weighted data derivatives and then filtering these back-projections. The weighted CB back-projections are given by

$$g(\overrightarrow{r}) = \int_{\lambda_i(\overrightarrow{r})}^{\lambda_o(\overrightarrow{r})}\frac{\widehat{P}(u_d, v_d, \lambda)}{|\overrightarrow{r} - \overrightarrow{y}(\lambda)|^2}d\lambda + \left[\frac{P(u_d, v_d, \lambda)}{|\overrightarrow{r} - \overrightarrow{y}(\lambda)|}\right]_{\lambda_i(\overrightarrow{r})}^{\lambda_o(\overrightarrow{r})}. \tag{3.20}$$

The expression of g is related to the attenuation function of the object f using the following fundamental formula

$$g_\pi(x_\pi, \lambda_i, \lambda_o) = 2 \int_{x_{\pi v1}}^{x_{\pi v2}} \frac{dx'_\pi}{x_\pi - x'_\pi} f_\pi(x'_\pi, \lambda_i, \lambda_o), \tag{3.21}$$

with $f_\pi(x_\pi, \lambda_i, \lambda_o) = 0$ for $x_\pi \notin [x_{\pi v1}, x_{\pi v2}]$. In other words, $x_{\pi v1}$ and $x_{\pi v2}$ are the lower and upper ends of the portion of the PI-line segment $[\lambda_i, \lambda_o]$ that intersects with the region of interest of the object. Basically, Eqn. (3.21) represents the filtering step in this algorithm. There are several approaches to solve (3.21) and recover f from its weighted CB back-projections g. Two main solutions will be described in the next chapter.

3.3 Iterative Algorithms

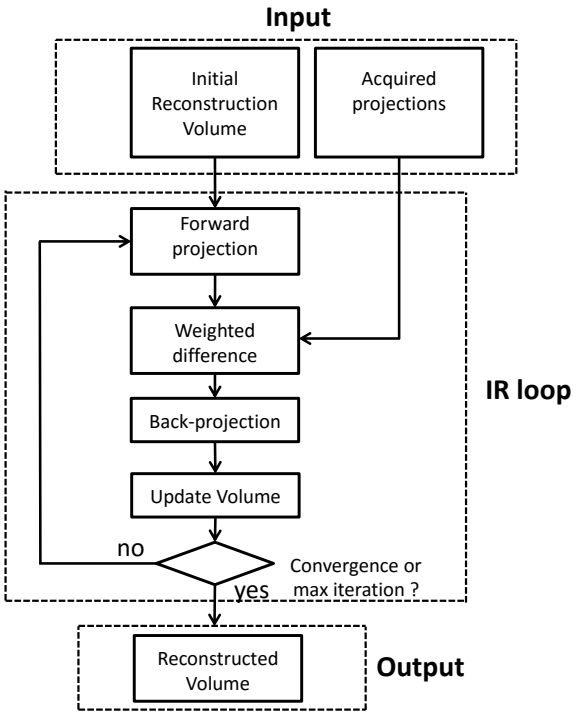

FIGURE 3.5: Basic schema of iterative reconstruction (IR) process.

Unlike analytic methods which perform reconstruction within a single step using a specific inversion formula, iterative methods refine and modify the image iteratively in order to minimize a cost function which measures the fit of the image to the projection data. This cost function is based on the imaging system model and can be solved using

an optimization algorithm. The global iterative process is illustrated in Fig. 3.5 and each iteration consists of the following three main steps:

- Forward projection to produce synthesized projections of the current image.
- Estimation of the difference between the synthesized projections and the experimentally acquired projections.
- Back-projection of the weighted difference to update the 3D volume.

The iteration process is ended when a fixed number of iterations is reached or when the update of the current volume estimate is small enough. To initialize the volume image either we start with an empty volume or with a prior volume reconstructed by a filtered-backprojection method. The more is the initial volume similar to the object, the more the algorithm converges rapidly to a stable solution. Iterative reconstruction algorithms are divided into two main types: algebraic and statistical methods.

3.3.1 Algebraic Methods

Algebraic methods are pure iterative methods without any modeling and which represent the reconstruction problem as a linear system of equations $P = A.f$ where P represents the projection data, A refers to the projection system model and f defines the voxel values in the object. A is very large and direct inversion is extremely time and memory intensive. Thus, algebraic methods aim to minimize the function error $\|A.f - P\|$. We present here standard algebraic methods like ART, SART, SIRT, OS-SIRT and MART. Then, we introduce a regularized algebraic method called DART that can incorporate prior knowledge of the attenuation coefficients in the object into the reconstruction process and can regularize the reconstruction under difficult practical conditions as few number of projections or missing data.

Algebraic reconstruction technique (ART)

ART was the first algorithm to be used in CT scanners [39]. It is a pure iterative algorithm without any modeling and is based on Kaczmarz method [51] to solve the linear system $P = A.f$. The convergence of this algorithm is noise sensitive where the more the data are corrupted with noise, the worse is the convergence. The following equation describes the structure of the algorithm:

$$f_j^{(k+1)} = f_j^k + \lambda \cdot \frac{p_i - \sum_{n=1}^{N} a_{in} \cdot f_n^k}{\sum_{n=1}^{N} a_{in}^2} \cdot a_{ij} \tag{3.22}$$

where a_{ij} represents an element in the matrix A with i the index of a pixel in the projection matrix P and j the index of a voxel in the image function f. For each iteration k,

the update of the voxel values in f is based on a single pixel p_i in the sinogram. λ is a relaxation parameter between 0 and 2. The smaller is λ, the better is the reconstruction but the longer is the computational time.

Simultaneous Algebraic Reconstruction Technique (SART)

SART [52] was introduced as an improvement of ART. The reconstruction process of this algorithm is defined by:

$$f_j^{(k+1)} = f_j^k + \lambda \cdot \frac{\sum_{p_i \in P_\theta} \frac{p_i - \sum_{n=1}^{N} a_{in} f_n^k}{\sum_{n=1}^{N} a_{in}} \cdot a_{ij}}{\sum_{p_i \in P_\theta} a_{ij}}. \tag{3.23}$$

Here, the update of the voxel values in f during each iteration k is based on a whole 2D projection matrix computed at a specific angle of view θ and not on a single pixel p_i in P. This leads to a faster convergence compared to ART.

Simultaneous Iterative Reconstruction Technique (SIRT)

Another form of ART named SIRT [38] has been developed. The update of the voxel values is based on the full 3D sinogram P as we can see in the structure of the algorithm given by

$$f_j^{(k+1)} = f_j^k + \lambda \cdot \frac{\sum_{p_i \in P} \frac{p_i - \sum_{n=1}^{N} a_{in} f_n^k}{\sum_{n=1}^{N} a_{in}} \cdot a_{ij}}{\sum_{p_i \in P} a_{ij}}. \tag{3.24}$$

Ordered Subsets Simultaneous Iterative Reconstruction Technique (OS-SIRT)

The concept of ordered subsets (OS) for CT reconstruction methods was firstly introduced by [72]. The idea is to divide the projection data into groups called subsets and the correctional updates are performed based on each subset instead of the complete set of projection data. For each iteration, we start by selecting one subset to update the image and then we rotate around all other consecutive subsets until all the projections are used. The aim is to increase the rate of convergence and therefore reduce the reconstruction time. The smaller is the number of projections per subset, the higher is the convergence speed. This technique was applied to SIRT and the obtained algorithm is called OS-SIRT [118]. OS-SIRT is equivalent to SART if each subset contains only one projection, whereas it corresponds to SIRT if there exists only one subset containing all the given projections.

Multiplicative Algebraic Reconstruction Technique (MART)

MART [40] is a nonlinear method that can be represented as

$$f_j^{(k+1)} = f_j^k \left(\frac{p_i}{\sum_{n=1}^{N} a_{in} \cdot f_n^k} \right)^{\lambda a_{ij}} . \tag{3.25}$$

We can notice here that MART multiply the correction term when updating the current image in contrast to all previously mentioned methods which add the correction term into the current solution. Therefore, f should be initialized with non-zero values in this case. While ART-based methods aims to minimize the overall variance of the reconstruction, MART maximizes the entropy [69, 68]. A significant advantage of MART is that it confines the reconstructed image to the convex hull of the object which is clinically important and allows dose reduction. The convex hull represent the envelope of all straight lines touching the object at its perimeter or surface, without crossing it. A simultaneous version of the MART algorithm named SMART was introduced later [17].

Discrete Algebraic Reconstruction Technique (DART)

When inspecting industrial objects, the different materials (aluminum, steel, plastic...) of the scanned object are often known in advance and thus the corresponding gray levels could be defined in the reconstruction. An iterative algorithm named DART has been developed [7] which can incorporate such prior knowledge of gray levels for each composition and can be applied if the object consists of five or less different materials. It is a regularized algebraic method that can produce accurate reconstruction results under extremely limited data conditions. DART combines an algebraic reconstruction method with a segmentation step. As visualized in Fig. 3.6, starting from an initial conventional algebraic reconstruction method like ART, SART or SIRT and based on known gray levels, a threshold operation is applied to obtain a segmented image that only has the given gray levels. Then, a region U is defined which contains the boundary region of the segmented image and other randomly added pixels. The pixels which do not belong to U are considered as fixed and are assigned their threshold values, whereas algebraic iterations on the non-fixed pixels belonging to U are performed again to refine the uncertain boundaries of the segmented image. As a remark, when fixing the pixels not belonging to region U, the number of unknowns in the system of linear equations is reduced and therefore the system becomes better determined. Finally, a Gaussian smoothing filter is applied before the iteration is repeated. The Gaussian filter is a way to reduce the fluctuations over the boundary pixels and to deal with noise.

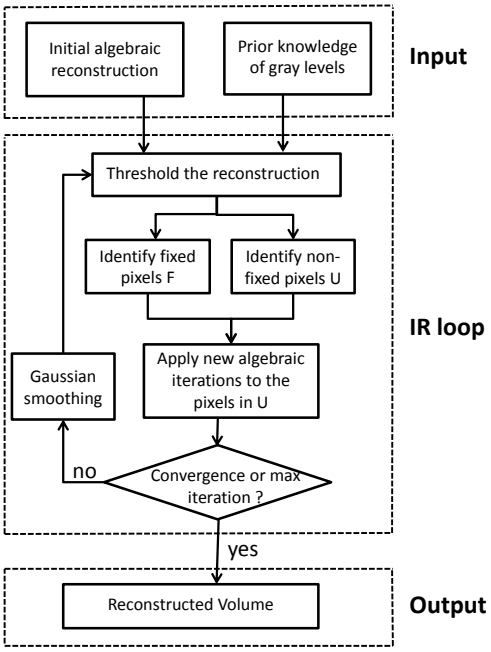

FIGURE 3.6: Schematic view of DART reconstruction process.

An adaptive DART algorithm [71] was developed which is more accurate than DART and achieves much better reconstruction on the borders. In addition to its application for reconstruction from small number of projections and from small angular range, DART was used as a technique to increase the reconstruction resolution [1]. When dealing with experimental dataset, the attenuation values can not be known exactly and therefore finding the right gray values of the object is not easy. To solve this problem, an advanced and more flexible segmentation method for DART algorithm named Projection Distance Minimization (PDM) has been proposed [110]. In this method, the gray levels are automatically estimated during the reconstruction process and the only required prior information is the number of gray levels. The estimation of these gray levels is based on minimizing the Euclidean distance between the forward projections of the segmented image and the projections measured during data acquisition. A multiresolution approach of DART to increase its computational efficiency and accelerate the convergence has been developed [23]. To improve the robustness of DART to noisy data, a modified DART algorithm named SDART was proposed [13]. This algorithm uses a penalty matrix to spread the noise across the whole image domain. Recently, another improved DART algorithm called TVR-DART [148] was introduced and which can give more accurate reconstructions than DART by integrating a total variation regularization term on the segmented reconstruction and replacing the hard segmentation function with an automated soft segmentation function.

3.3.2 Statistical Methods

Statistical reconstruction methods can model the photon counting statistical properties of the detector or X-ray source and can operate in either sinogram domain or image domain or both domains (full statistical). Statistical methods working in the sinogram domain allow to reduce noise in projection raw data without significantly impairing spatial resolution. An example of such algorithms propose adaptive filtering approaches based on the local statistical properties of the projections [43, 50]. Alternative sinogram smoothing approach using a roughness-penalized Poisson likelihood objective function was proposed also [64]. On the other hand, image domain-based methods aim at denoising the image after the reconstruction. Full statistical methods work during the reconstruction process and are divided into two groups of methods which are based on either the maximum likelihood (ML) or the least squares (LS).

An algorithm named maximum likelihood expectation-maximization (MLEM) was originally developed for emission tomography [94] and then adapted to transmission tomography [66]. This algorithm consists of two main steps: an expectation (E) step that computes the expectation of the log-likelihood, and a maximization (M) step that finds the parameters maximizing the expected log-likelihood computed on the E step. To accelerate the convergence speed, the ordered subset principle was applied to MLEM forming OS-EM algorithm [73]. Based on the maximum likelihood concept, the convex algorithm [65] was introduced. This algorithm retains the E-step, but provides an approximation to the M-step and as a result converges much faster than the standard MLEM algorithm. Again the convex algorithm has been accelerated by the use of ordered susbsets to propose the OSC algorithm [55, 11]. An important technique that incorporates a polychromatic acquisition model into the Maximum-Likelihood Algorithm was proposed to eliminate beam-hardening artifacts [26].

Least-squares Bayesian reconstruction methods which update a single pixel at each iteration and are known as iterative-coordinate-descent (ICD) were proposed [14, 90, 137]. These methods are based on direct optimization of the maximum a posteriori (MAP) criterion and converges faster than EM-based approaches which take an indirect approach. Positivity constraints and non-Gaussian prior distributions could be easily incorporated in the ICD algorithm. Knowing that these methods rely on updating a single pixel each iteration, it is difficult to develop multi-threaded CPU or GPU implementations. However, the convergence is very rapid if we start from an initial FBP reconstructed image [14] which has the benefit of providing a good estimate of the low frequency components. The ordered subsets concept (OS-ICD) was applied to speed up the convergence of this algorithm [67]. Furthermore, a non-homogeneous ICD (NH-ICD) algorithm [139, 138] was proposed to accelerate the convergence by focusing computation where it is most needed. A statistical algorithm [108] using the

ICD approach was applied to real patient data generated on a helical trajectory. The reconstruction results show significant reduction of helical CB artifacts, enhanced image resolution and reduced noise level.

Other statistical algorithms like conjugate gradient (CG) [10] and preconditioned conjugate gradient approaches [74] have been developed based on the MAP estimation problem. These algorithms are known to have high convergence speed for quadratic optimization problems. However, they demand more memory than ICD approaches and can't incorporate positivity constraints into the reconstruction process. It should be mentioned that applying positivity constraint can enhance the quality of reconstruction results and accelerate numerical convergence [82].

3.4 Discussion

We summarize here the pros and cons of each set of reconstruction algorithms according to its nature. This discussion can be divided into two parts. The first part compares approximate and exact analytical algorithms, whereas the second part compares analytical and iterative algorithms.

3.4.1 Approximate Versus Exact Analytical Algorithms

Although approximate algorithms produce some image artifacts when the cone angle becomes large, they are very efficient and give high quality reconstructions in case of small cone angle. It was mentioned that these algorithms may be competitive against exact alternatives in terms of image resolution, noise robustness and dose efficiency provided that the CB angle is small [111]. Despite the significant research efforts which have been devoted to the subject of exact reconstruction since the introduction of Katsevich's algorithm, approximate algorithms have been dominating in CT applications [112]. It was stated that approximate reconstruction approaches derived from the FDK algorithm are still the dominant force behind most commercial CT scanners [45].

It should be mentioned also that exact reconstruction algorithms are not as flexible as approximate ones and can not be adapted to the half-scan geometry. In terms of noise characteristics, exact algorithms are not necessarily optimal because the redundant projection data are usually discarded. The major concerns nowadays for exact helical reconstruction algorithms are computational cost and accuracy (robustness to noise and free of artifacts).

3.4.2 Analytical Versus Iterative Algorithms

As we have seen analytical reconstruction is based on an idealized mathematical model and an inverse transform is employed. It is fast and linear (i.e. we can analyze some

properties like spatial resolution and robustness to noise). In case of complete and low-noise data with a sufficient data sampling, analytical algorithms are preferred because of their model simplicity, high speed and low memory demands.

In practical situations, the projections are affected by noise, the X-ray source is polychromatic and not point-like as assumed by the model. Moreover, in many cases the object is not accessible for full measurements because of some geometrical constraints. Here, analytical reconstruction is not the optimal choice because it treats all X-rays equally and it is severely affected by incomplete or sparse data [12]. In this situation, iterative reconstruction methods perform much better. Iterative approaches are more realistic and can better model the physics of data acquisition. In addition, they can handle much more noisy data, allow more flexibility in the scanning geometry, deal with incomplete or sparse data and can easily incorporate prior knowledge into the reconstruction process.

The major drawback of iterative algorithms are their model complexity and high computational cost. Another downside is their non-linear behavior where it is difficult to analyze noise properties and spatial resolution [70]. In addition, certain important parameters have to be chosen and that are usually significant for the performance of iterative reconstruction methods.

Generally speaking, analytical reconstruction is more efficient whereas iterative methods can improve image quality at the cost of higher computational demands. However, this latter is becoming more acceptable with the high technological development in computer performance and the introduction of parallel implementation using graphics processing unit (GPU).

Chapter 4

CT Reconstruction on Helical Scanning Geometry

This chapter is devoted only to image reconstruction on a helical scanning trajectory. This trajectory can collect data sufficient for an exact reconstruction of the object and thus has a considerable potential for long object imaging which is the main limitation of circular scanning trajectories. We assume here that the trajectory is complete and thus we study only analytical methods of reconstruction due to their simplicity and low computational cost. In particular, we consider two exact helical algorithms of type FBP and BPF which were developed by Zou and Pan [149, 150] and has been extensively studied by different research groups. In addition, we consider the approximate and widely used helical FDK algorithm [113] as a reference for evaluation and performance comparison.

The chapter is divided into two sections. The first section presents a numerical comparison of the three mentioned helical algorithms. Furthermore, we present the implementation details of the algorithms of Zou and Pan with an optimized implementation of the FBP algorithm [150]. We show by numerical simulations the advantages of our implementation approach compared to the original one proposed by Zou and Pan.

In the second section, we present two helical FDK-type algorithms that can handle transversely truncated data. These two algorithms use alternative approaches for filtering the projections which can reduce reconstruction artifacts obtained with the standard FDK reconstruction that is based on the ramp filter and that can not deal with transversely truncated projections. CIVA simulated data are used to show the advantages of these two algorithms in case of truncated data.

4.1 Study of Helical Reconstruction Algorithms

In this section, a theoretical comparison of the three algorithms is shown. The implementation of the FDK algorithm is relatively simple. Thus, we only explain here the implementation details of the two (FBP and BPF) inversion formulas proposed by

Zou and Pan. We also compare our proposed implementations with the original ones and we demonstrate a numerical comparison of the three algorithms. For performance evaluation of the described algorithms, both complete (noise-free and noisy) and truncated data generated by CIVA are used in computer simulations.

4.1.1 Theoretical Analysis of the Implemented Algorithms

The FDK algorithm is approximate and lacks of a mathematical theory that can yield an inversion formula with exact reconstruction. The ramp filter is global and thus filtering any point in the 2D projection matrix requires a complete knowledge of the whole corresponding detector row. When projections are truncated transversely, this condition is not satisfied and as a result the filtering step is not performed correctly which produces significant artifacts in the reconstructed image. In other words, the FDK algorithm can not handle truncated data.

The two algorithms proposed by Zou and Pan are based on exact mathematical inversion formulas. These two algorithms are not as flexible as the FDK algorithm which can be adapted to the half-scan geometry. The filtering step is basically composed of the first derivative operator and the Hilbert transform and which is supposed to give better performance than the ramp filter when data are truncated transversely. This will be validated by numerical simulations and more theoretical explanations will be given in the next section.

The minimum detection window of the helical FDK algorithm is bounded by the adjacent lower and upper helical turns and is larger than the Tam-Danielsson window which was theoretically proven as the minimum detector size required for an exact reconstruction. In particular, the BPF algorithm uses data only in the Tam-Danielsson window, whereas the size of the detector array required for the FBP algorithm is slightly greater than the Tam-Danielsson window.

Going back to the description of the BPF algorithm in the previous chapter, we can see that the filtering step (Eqn. (3.21)) is performed along the PI-lines in the image domain and thus the reconstructed image is obtained in the PI-line coordinate system $(x_\pi, \lambda_i, \lambda_o)$. As a result, an interpolation step is needed for rebinning the obtained attenuated function $f_\pi(x_\pi, \lambda_i, \lambda_o)$ into the local coordinate system of the object $(\overrightarrow{e}_x, \overrightarrow{e}_y, \overrightarrow{e}_z)$. This additional interpolation step denotes a loss in the spatial resolution of the reconstructed image. Hence, the BPF algorithm suffers from a poor spatial resolution compared to the other two algorithms.

4.1.2 Implementation and Optimization of the FBP Algorithm

Zou and Pan have validated their proposed FBP algorithm [150] following a PI-line based implementation that can be synthesized as follows:

- Step 1: Compute the modified data $\widehat{P}$ (Eq. (3.18)) for each rotation angle λ.
- Step 2: Perform a 1D-Hilbert filtering on the modified data (Eq. (3.19) using $\widehat{P}/A^2$).
- Step 3: Find all the PI-lines passing through the ROI of the object.
- Step 4: For each PI-line specified by the extremities λ_i and λ_o, back-project the filtered data obtained in Step 2 to get $f_\pi(x_\pi, \lambda_i, \lambda_o)$ along the PI-line segment $[\lambda_i, \lambda_o]$.
- Step 5: Apply a 3D interpolation on $f_\pi(x_\pi, \lambda_i, \lambda_o)$ to obtain $f(x, y, z)$ the attenuation function of the object in the fixed coordinate system. A simple 3D linear interpolation is used.

However, with this strategy the 3D interpolation on $f_\pi(x_\pi, \lambda_i, \lambda_o)$ to get $f(x, y, z)$ will affect the spatial resolution of the reconstructed image. Thus, we propose in this work a voxel-based implementation to reconstruct the image directly in the global coordinate system of the object. The voxel-based implementation consists of the following steps:

- Step 1: Compute the modified data $\widehat{P}$ (Eq. (3.18)) for each rotation angle λ.
- Step 2: Perform a 1D-Hilbert filtering on the modified data (Eq. (3.19) using $\widehat{P}/A^2$).
- Step 3: Find all the Voxels defining the image of the object.
- Step 4: For each Voxel of position (x, y, z), back-project the filtered data obtained in Step 2 along its corresponding PI-line $[\lambda_i, \lambda_o]$ to get $f(x, y, z)$ (attenuation function of the object at position (x, y, z)).

For both implementations the computational cost would be $O\left[N_\lambda N_f N_u log(N_u)\right]$ (steps 1 and 2) + $O\left[N_x N_y N_z N_\lambda\right]$ where N_x, N_y, and N_z correspond to the number of image voxels in the x-, y- and z- direction, respectively. N_λ refers to the number of rotation angles λ, N_u is the sampling number along each PI-line and N_f is the set of filtering lines. However, in our proposed implementation, we avoid the rebinning step that remaps the reconstructed image from the PI-line coordinate system into the coordinate system of the object and consequently we need a smaller number of views N_λ which reduces the computational cost of the algorithm.

4.1.3 Implementation of the BPF algorithm

As shown previously in the third section, the difficulty of the BPF algorithm [149] is to obtain the attenuation function f from its weighted CB back-projections g based on Eq. (3.21). First, let's see the approach proposed by Zou and Pan to solve (3.21). For a

given PI-line (dashed line in Fig. 4.1) of extremities λ_i and λ_o with abscissas along the u_π-axis denoted by $x_{\pi\lambda_i}$ and $x_{\pi\lambda_o}$, respectively, define G_n and F_n as the Fourier series expansions of $g_\pi(x_\pi, \lambda_i, \lambda_o)$ and $f_\pi(x_\pi, \lambda_i, \lambda_o)$, respectively. We have :

$$G_n(\lambda_i, \lambda_o) = \int_{x_{\pi\lambda_i}}^{x_{\pi\lambda_o}} g_\pi(x_\pi, \lambda_i, \lambda_o) e^{2\pi j n \omega_\pi x_\pi} \, dx_\pi \tag{4.1}$$

and

$$F_n(\lambda_i, \lambda_o) = \int_{x_{\pi\lambda_i}}^{x_{\pi\lambda_o}} f_\pi(x_\pi, \lambda_i, \lambda_o) e^{2\pi j n \omega_\pi x_\pi} \, dx_\pi. \tag{4.2}$$

Substituting (4.1) and (4.2) in (3.21), we obtain :

$$G_n(\lambda_i, \lambda_o) = \sum_{n'} K_{n,n'} F_{n'}(\lambda_i, \lambda_o), \tag{4.3}$$

where

$$K_{n,n'} = \int_{x_{\pi\lambda_i}}^{x_{\pi\lambda_o}} dx_\pi \int_{x_{\pi\lambda_i}}^{x_{\pi\lambda_o}} \frac{e^{2\pi j \omega_\pi (n x_\pi - n' x_p i')}}{x_\pi - {x_\pi}'} \, d{x_\pi}', \tag{4.4}$$

n and n' are the frequency indices corresponding to x_π and ${x_\pi}'$, respectively, and $\omega_\pi = \frac{1}{(x_{\pi\lambda_o} - x_{\pi\lambda_i})}$. Knowing that we can calculate the values of G_n for each PI-line using (4.1) and (3.20) and that we can compute the kernel $K_{n,n'}$ following Eq. (4.4), consequently the linear system (4.3) can be solved and we get F_n along each PI-line. Finally, we can obtain f_π by calculating the inverse Fourier series expansion of F_n.

In this work, we did not follow the same way of implementation as Zou and Pan and we proposed a different approach to solve (3.21). It can be observed in (3.21) that $g_\pi(x_\pi, \lambda_i, \lambda_o)$ represents the finite Hilbert transform of $f_\pi(x_\pi, \lambda_i, \lambda_o)$. The finite inverse Hilbert transform has been studied widely and an efficient formula for the inversion of the finite Hilbert transform has been proposed [142, 128]. Based on this formula, we have derived a new solution to Eqn. (3.21):

$$f_\pi(x_\pi, \lambda_i, \lambda_o) = \frac{1}{2\pi \left(\sqrt{(x_{\pi v2} + \varepsilon)^2 - x_\pi^2} - \sqrt{x_{\pi v2}^2 - x_\pi^2} \right)} \int_{-x_{\pi v2}-\varepsilon}^{x_{\pi v2}+\varepsilon} \frac{K(x_{\pi v2}, {x_\pi}')}{(x_\pi - {x_\pi}')} g_\pi({x_\pi}', \lambda_i, \lambda_o) d{x_\pi}', \tag{4.5}$$

where

$$K(x_{\pi v2}, x) = \begin{cases} -\sqrt{(x_{\pi v2} + \varepsilon)^2 - x^2} & \text{if } x_{\pi v2} < |x| < (x_{\pi v2} + \varepsilon) \\ \sqrt{(x_{\pi v2})^2 - x^2} - \sqrt{(x_{\pi v2} + \varepsilon)^2 - x^2} & \text{if } x_{\pi v1} < x < x_{\pi v2} \\ 0 & \text{otherwise,} \end{cases} \tag{4.6}$$

with $x_{\pi v1}$ and $x_{\pi v2}$ are the abscissas of the lower and upper ends of the portion of the PI-line segment intersecting with the region of interest of the object. These abscissas

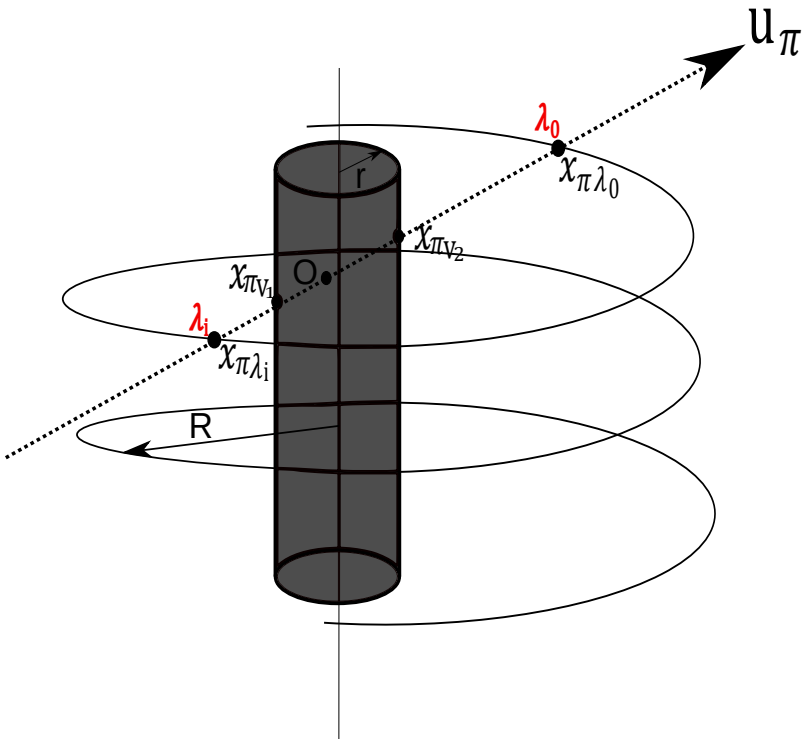

FIGURE 4.1: Illustration of a PI-line and some notations.

are calculated on the the axis directed along the PI-line (U_π direction in Fig. 4.1) and whose origin O is defined by the midpoint of the segment [$x_{\pi v1}$,$x_{\pi v2}$]. ε is a small positive number to be chosen based on the value of $x_{\pi v2}$. It was mentioned that a good choice of ε satisfies the condition $(x_{\pi v2} + \varepsilon)/x_{\pi v2} = 1.0667$ [142]. To summarize, our approach (Eqn. (4.5)) of filtering the data consists of three steps: (i) pre-weighting, (ii) Hilbert filtering and (iii) post-weighting. Similar to the numerical implementation of the FBP algorithm, we present here the steps involved in the implementation of the BPF algorithm:

- Step 1: Compute the modified data $\widehat{P}$ (Eq. (3.18)) for each rotation angle λ.
- Step 2: Find all the PI-lines passing through the ROI of the object.
- Step 3: For each PI-line specified by the extremities λ_i and λ_o, back-project the modified data $\widehat{P}$ along this PI-line segment to get $g_\pi(x_\pi, \lambda_i, \lambda_o)$.
- Step 4: Perform an inverse 1D-Hilbert filtering (Eq. (4.5)) along each PI-line $[\lambda_i, \lambda_o]$ of the weighted back-projected image $g_\pi(x_\pi, \lambda_i, \lambda_o)$ to get $f_\pi(x_\pi, \lambda_i, \lambda_o)$.
- Step 5: Rebin the obtained attenuation function $f_\pi(x_\pi, \lambda_i, \lambda_o)$ into the local coordinate system of the object $(\vec{e}_x, \vec{e}_y, \vec{e}_z)$ using a simple 3D linear interpolation.

The computational cost here would be $O\left[N_\lambda\right]$ (step 1) + $O\left[N_x N_y N_z N_\lambda N_u log(N_u)\right]$ and as we can see the filtering step is performed along the PI-lines and as a result this BPF algorithm must be implemented in a PI-line-based way which needs a greater number of projections N_λ compared to the FBP algorithm.

4.1.4 Voxel-based Versus PI-line-based Implementation of the FBP Algorithm

First of all, we aim to show numerically the advantages of our proposed voxel-based implementation of the FBP algorithm compared to the PI-line based implementation developed by Zou and Pan. In this comparison, we have used the 3D Shepp-Logan head phantom [93] as a basic reference model to carry on simulation experiments. The theoretical density values of this phantom are between 0 and 1 and its support is an ellipsoid with 6.9 cm, 9.2 cm and 8.1 cm, the half length of the x-, y- and z-axes, respectively.

TABLE 4.1: Simulation parameters for generating numerical projections using the Shepp-Logan phantom.

Object radius (r)	10 cm
Helix radius (R)	90 cm
Source-detector distance (D)	180 cm
Helical pitch (2πh)	10 cm
Detector width (W)	40.7 cm
Detector height (H)	11.1 cm
Detector sampling	185×678 pixels
Detector pixel size	0.6×0.6 mm^2
Reconstruction matrix	$512 \times 512 \times 512$ voxels

The CB helical data were simulated with a configuration specified in Table 4.1. As a remark, the pitch value is chosen to satisfy the condition that the detector is larger than the Tam-Danielsson window. We assume in this simulation that the X-ray source is monochromatic and the sinogram is computed based on geometrical aspects only where we neglect all other physical issues. We have computed projection data over 1310 rotation angles (512 projections per turn) uniformly distributed between $\lambda_{min} = -2.56\pi$ and $\lambda_{max} = 2.56\pi$.

Fig. 4.2 shows three orthogonal central slices of the phantom reconstructed using the FBP algorithm. The first row corresponds to original orthogonal central slices in the phantom with the white-dashed lines used for 1D numerical comparison. Two computer simulations compare the PI-line-based and voxel-based implementations. The PI-line-based implementation of the algorithm provides the reconstruction illustrated in the second row. It is clear that some distortions appear in the non-uniform regions of

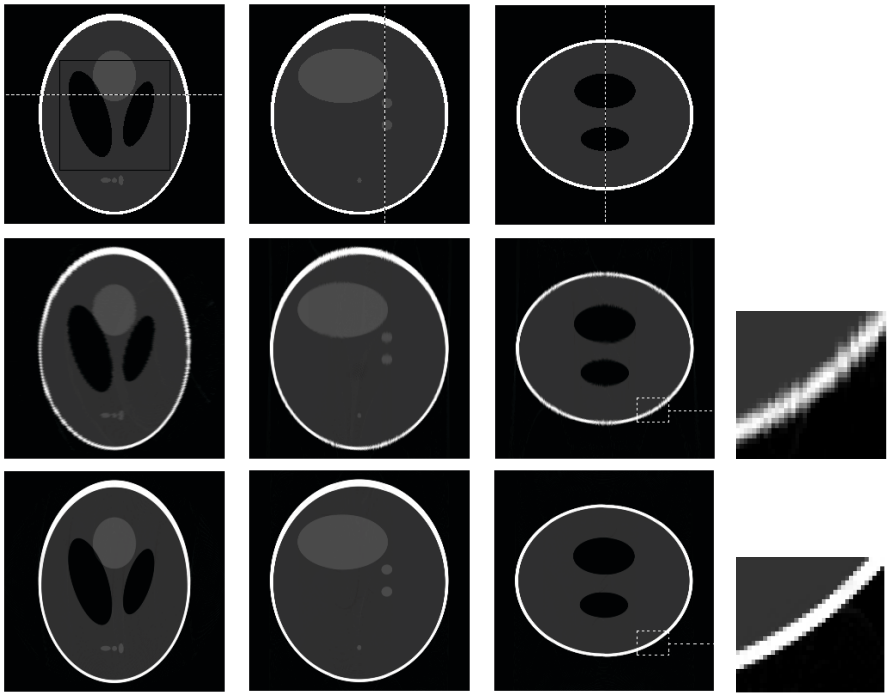

FIGURE 4.2: Reconstruction of the Shepp-Logan phantom using the FBP algorithm. Three orthogonal central slices of the original image are displayed in the first row. The second and third row shows the slices reconstructed using the PI-line-based and voxel-based implementations of the algorithm, respectively.

the three slices. These distortions come from the performed interpolation in the rebinning step. As illustrated in the third row, our proposed voxel-based implementation is more accurate and we do not obtain these distortions in the reconstruction.

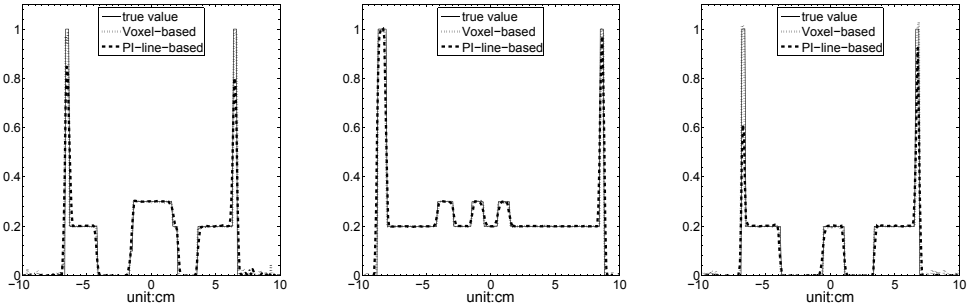

(A) x = -1.45 cm and z = 0. (B) y = 0 and z = 2.5 cm. (C) x = 0 and z = 0.

FIGURE 4.3: 1D profile lines through different slices of the reconstructed phantom shown in Fig. 4.2.

A 1D numerical comparison of the original and reconstructed values using the two described implementations is illustrated in Fig. 4.3. Specifically, Fig. 4.3a displays

the profile along the position x= -1.45 cm in the horizontal slice (z = 0). The profile along the line specified by y = 0 and z = 2.5 cm is illustrated in Fig.4.3b. Finally, Fig. 4.3c shows the profile along the line determined by x = 0 and z = 0. For the voxel-based implementation, the true (continuous line) and reconstructed (dotted line) values are in excellent agreement. However, the reconstructed values of the PI-line-based implementation (dashed line) are not very close to the original values.

4.1.5 Numerical Comparison of the Implemented Algorithms

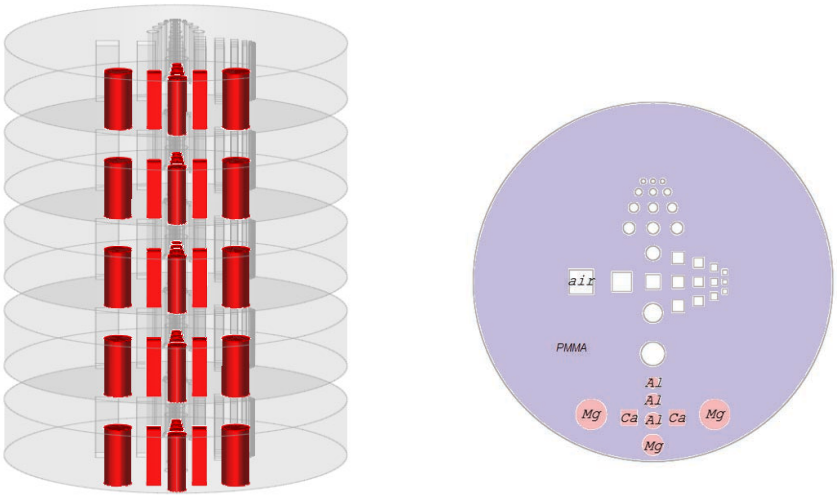

(A) 3D view (B) horizontal slice

FIGURE 4.4: CIVA multi-disk phantom illustration.

We aim to investigate the behavior of the three mentioned algorithms using CIVA-simulated data generated along a standard helical trajectory with the configurations specified in Table 4.2. The simulated object is a computer-aided-design (CAD) model phantom which is similar to the Defrise disk phantom [27] with additional rectangular and circular holes of different sizes (see Fig. 4.4). In this simulation and in what follows we use a monochromatic X-ray source of 80 KeV and Monte Carlo methods are not considered where we neglect the scattering of photons. The height of this phantom is 18.5 mm and it consists of five circular disks with thickness 2.5 mm stacked along the z-direction and separated by 1.5 mm with the radius of each disk is 7.5 mm. The phantom is made of polymethyl-methacrylate (PMMA), aluminum (Al), calcium (Ca) and magnesium (Mg).

TABLE 4.2: CIVA numerical simulation parameters.

Object radius (r)	7.5 mm
Helix radius (R)	30 mm
Source-detector distance (D)	60 mm
Helical pitch (2πh)	2.333 mm
Number of helical turns	9
Number of projections per turn	360
Detector pixel size	0.065×0.065 mm^2
Detector sampling	100×512 pixels
Reconstruction matrix	$512 \times 512 \times 512$ voxels

In what follows, the quality of the reconstructed $M \times N \times P$ image is assessed quantitatively through the mean square error (MSE) defined as:

$$MSE(f_r) = \frac{1}{MNP} \sum_{i=1}^{M} \sum_{j=1}^{N} \sum_{k=1}^{P} |f_r(i,j,k) - f(i,j,k)|^2, \tag{4.7}$$

where f_r and f are the reconstructed and original images, respectively.

Noiseless Data

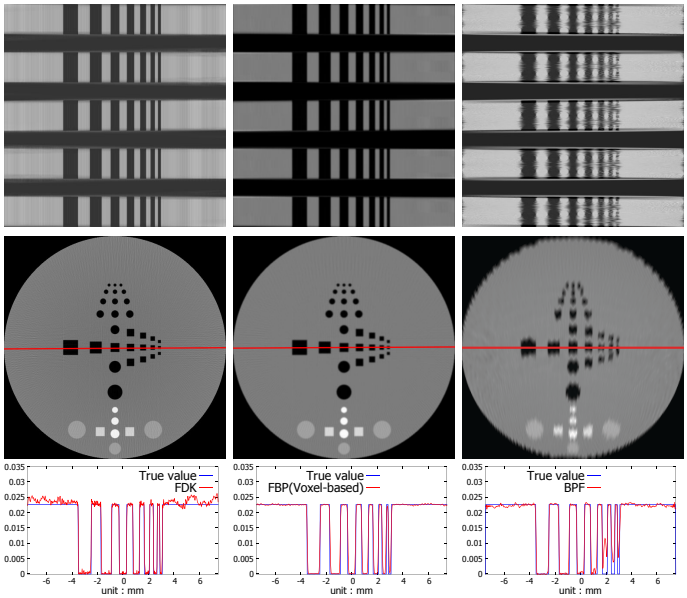

(A) FDK (B) FBP (C) BPF

FIGURE 4.5: Reconstruction of the multi-disk phantom from complete noiseless projection data (360 projections per turn).

We firstly simulate noise-free CB projections and the reconstruction results are shown in Fig. 4.5 with a display window [0,0.03] that refers to the range of attenuation coefficients in the object. The first column corresponds to the helical FDK reconstruction whereas the second and third columns refer to reconstruction results using the FBP and BPF algorithms, respectively. We illustrate a vertical central slice of each reconstructed image in the first row. The horizontal central slice of each reconstructed image is displayed in the second row with red lines used for the 1D numerical comparison plotted in the third row. It is clear from the reconstructed slices that the BPF algorithm shows artifacts and suffers from a poor spatial resolution because of the additional interpolation step performed as described previously. These artifacts do not appear in the images reconstructed by the FDK and FBP algorithms and it can be observed that the FBP algorithm gives better image quality. The 1D profiles show a good agreement between the reconstructed values (red lines) and the original ones (blue lines) except for the BPF algorithm. This 1D numerical comparison illustrates the exact property of the FBP algorithm where the reconstructed values are very close to the original ones in contrast to the approximate FDK algorithm whose reconstructed values are less accurate.

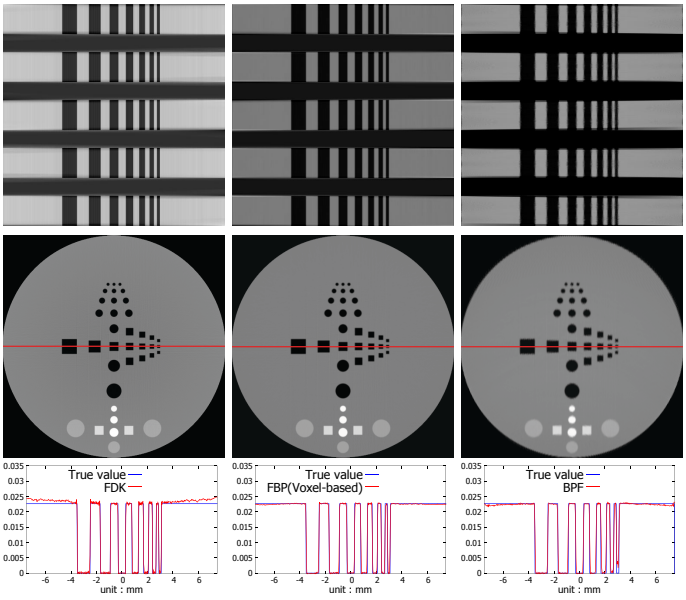

(A) FDK (B) FBP (C) BPF

FIGURE 4.6: Reconstruction of the multi-disk phantom from complete noiseless projection data (1080 projections per helical turn).

In practice, the spatial resolution of the BPF algorithm can be improved if we get a large number of projections. For this reason, we have increased the number of projections per turn to 1080. We show in Fig. 4.6 a vertical and horizontal central slice of each reconstructed image and a 1D numerical comparison along the red lines. The

reconstructed values (red lines) agree well with the original ones (blue lines) for the three algorithms. Among the three algorithms, FBP shows excellent results and is the most accurate one.

Noisy Data

In fact, X-ray photons counting on the detector follows a Poisson distribution. For high number of counts this distribution can be considered as a Gaussian one and the noisy projections are denoted by

$$g^n(u_d, v_d, \lambda) = g(u_d, v_d, \lambda) + n(\sigma), \tag{4.8}$$

where $n(\sigma)$ is an additive white Gaussian noise of standard deviation σ. Noisy data were generated from a Gaussian with σ equal to 0.5% of the maximum value in the noiseless data. The reconstruction of the phantom disk from noisy projections is illustrated in Fig. 4.7. The 1D numerical comparison along the red lines demonstrates that the FBP and BPF algorithms are more robust to noisy data than the helical FDK algorithm. Specifically, the BPF algorithm shows better robustness to noisy data compared to the FBP algorithm.

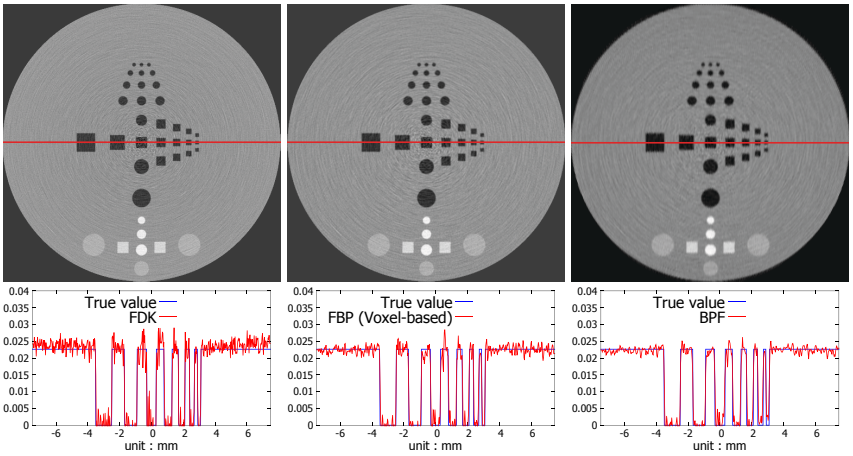

(A) FDK (B) FBP (C) BPF

FIGURE 4.7: Reconstruction of the multi-disk phantom from complete noisy projection data (1080 projections per helical turn).

Usually, the ramp filter is apodized with a smoothing window for a better response to noisy data. An example of such window is the Hamming smoothing window which can significantly suppress noise as we can see in Fig. 4.8 that shows a comparison of an FDK reconstruction using a standard ramp filter (see Fig. 4.8 (A)) and using a ramp filter combined with the Hamming window (see Fig. 4.8 (B)). The horizontal central slice of each reconstructed image and the 1D profiles illustrate that the noise has

been been effectively suppressed when the ramp filter is smoothed with the Hamming window. One disadvantage of this window is reducing the spatial resolution of the image. Thus, a good choice of the cut-off frequency of the window is necessary for compromising between noise characteristics and spatial resolution.

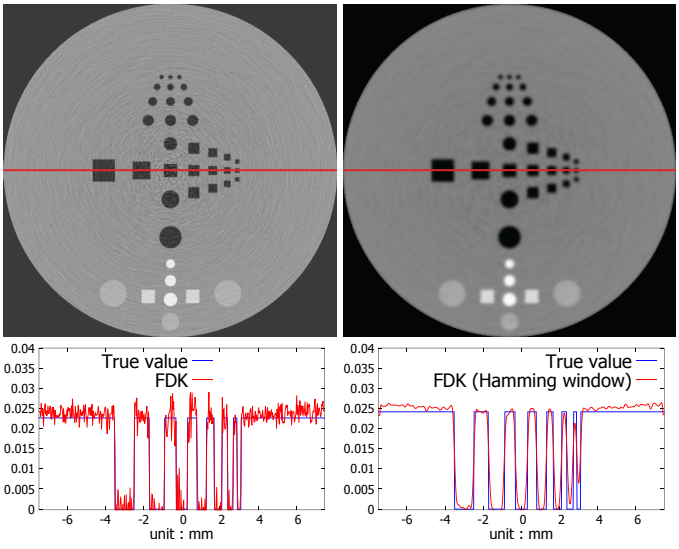

(A) (B)

FIGURE 4.8: FDK reconstruction of the multi-disk phantom from complete noisy projection data (1080 projections per helical turn) (A) without and (B) with Hamming smoothing window.

Truncated Data

We aim to study reconstruction from truncated data. As an example, 128 pixels on each side of every row in the detector are set to zero. Within this configuration, only half of the object is viewed by the detector and as a result the field-of-view (FOV) is reduced to its half size as we can see in Fig. 4.9.

Figure 4.10 shows reconstruction results from transversely truncated data. Horizontal central slices in the FOV (red circular dashed-region in Fig. 4.9) of the images reconstructed by the three algorithms are shown in the first row with a 1D numerical comparison along the red lines is displayed in the second row. The first column corresponds to FDK reconstruction whereas the second and third columns correspond to FBP and BPF reconstruction, respectively.

It can be clearly seen that important artifacts known as cup-artifacts appear on the boundaries of the image reconstructed by FDK, whereas these artifacts are suppressed when using the FBP and BPF algorithms. For quantitative evaluation and if we compare the reconstruction values plotted along the 1D profiles, we can notice that the FBP and BPF algorithms give much better reconstruction values than the FDK algorithm

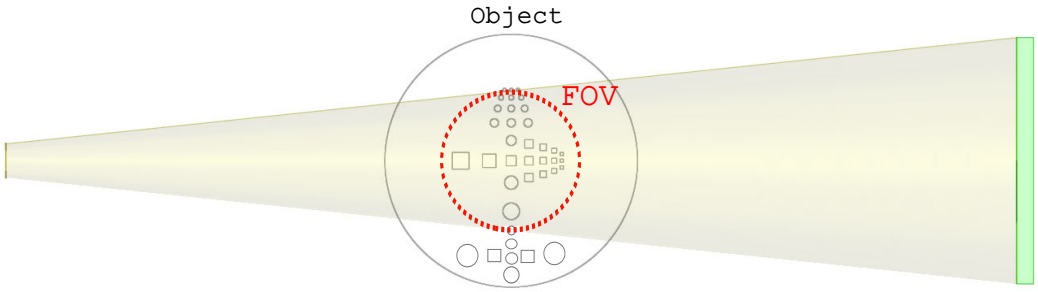

FIGURE 4.9: Illustration of the FOV corresponding to truncated projection data.

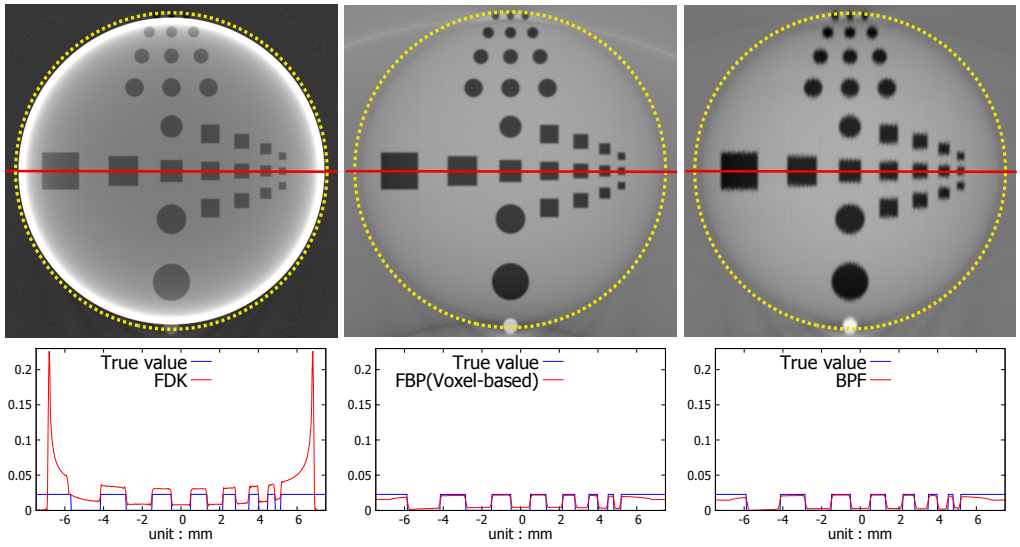

(A) FDK (B) FBP (C) BPF

FIGURE 4.10: Reconstruction of the multi-disk phantom from truncated noiseless projection data (1080 projections per helical turn). The yellow dotted-circular region corresponds to the FOV of the reconstructed image.

that denotes a large offset value. To summarize, the FBP and BPF algorithms are not exact when data are truncated. However, they give satisfying results and they perform much better than the FDK algorithm that shows severe artifacts. We will present in the next section two modified helical FDK algorithms that can deal with transverse truncation.

Quantitative Evaluation and Reconstruction Time

Table 4.3 shows a comparison of the three algorithms for the first (complete noiseless data), second (complete noisy data) and third (truncated noiseless data) simulations.

In this table, we show the measured MSE and the time of reconstruction for each algorithm. The MSE is computed on the whole 3D volume in the case of complete data and only for the considered FOV when the projections are truncated.

TABLE 4.3: Quantitative evaluation of the three described algorithms.

Reconstruction algorithm	FDK	FBP	BPF
Reconstruction time (minutes)	52.5	74.1	74.8
Mean-square-error (complete noiseless data) $\times 10^{-6}$	5	3.5	5.4
Mean-square-error (complete noisy data) $\times 10^{-6}$	32.3	14.9	9.6
Mean-square-error (truncated noiseless data) $\times 10^{-6}$	252.8	6.6	6.2

The reconstruction time of the FBP and BPF algorithms is similar and is greater than that of the FDK algorithm. The MSE measurements correlates well with the previously illustrated reconstructed images. The FBP algorithm denotes the smallest MSE value and is the most accurate one when reconstructing from complete noiseless data. When projection data are noisy, the MSE values of the FBP and BPF algorithms are much smaller than that of the FDK algorithm. In case of truncation, the FBP and BPF algorithms show very small MSE values compared to the FDK algorithm which gives artifacts and high reconstruction error.

4.2 FDK-type Algorithms for Transversely Truncated Data

Different methods have been proposed to reduce the effect of truncation artifacts. We will just mention here some of analytical methods due to the large amount of published work on this aspect.

The most common approach is extrapolating the truncated projections to estimate the missing truncated data and then to perform standard reconstruction from extrapolated projections [80]. Later, other methods were proposed that do not demand this additional extrapolation step to eliminate truncation artifacts. For example, we can mention the FBP and BPF algorithms mentioned in the previous section. However, these two algorithms can not denote an exact reconstruction in case of truncated data. Algorithms based on the concept of differentiated back-projection (DBP) [149, 86] were proposed for exact ROI reconstruction even when data are truncated. The idea is to compute the derivative of projection data firstly and then to back-project into the image space. Finally, these back-projected differentiated data are filtered along specific lines in the image domain using the Hilbert kernel. In this strategy, the derivation and back-projection steps are local and hence not affected by truncation. Thus, reconstruction errors come only from the filtration step which represents the inversion of the truncated Hilbert transform. Exact and stable solution for the inversion of the truncated Hilbert transform is generally impossible. However, it was stated that a prior knowledge on a

small subregion in the region of interest of the object allows to obtain a stable inversion of the truncated Hilbert transform [63]. This inversion can be performed in an analytic or iterative way. An efficient technique named POCS (projection into convex sets) originally developed for iterative reconstruction [130] was used to invert the truncated Hilbert transform algebraically aided by a prior information on the object [31]. This approach is more costly than analytic ones but yields an accurate reconstruction with several truncation configurations. Thus, if a prior knowledge on a region in the object is available, the inversion of the truncated Hilbert transform is unique and therefore we can obtain an accurate ROI reconstruction. However, these type of algorithms are expensive and time-consuming compared to FDK-type algorithms.

Recently, two interesting filtered-backprojection (FBP) algorithms for ROI reconstruction on circular trajectory have been published [116, 115]. These algorithms are based on the general structure of the FDK algorithm [35] but follow a different approach when filtering the projections. Remind that in case of transversely truncated data, FDK reconstruction errors come only from the non-local ramp filtering step. Based on this work, we propose here to replace the global ramp filtering approach in the helical FDK algorithm into either the local first derivative operator combined with the Hilbert transform or the 1D Laplace operator followed by a non-local filtering step using a logarithmic kernel. A more detailed description of these two approaches is given thereafter.

4.2.1 FDK Algorithm Based on the First Derivative Operator

A fundamental relationship that relates ramp filtering to the Hilbert transform was demonstrated as follows [79]:

$$P_R(u_d, v_d, \lambda) = \frac{1}{2\pi} \frac{\partial}{\partial u_d} P_H(u_d, v_d, \lambda). \tag{4.9}$$

Here, P_H is obtained by applying the Hilbert transform along each row in the data matrix P. Based on this Eqn., it was proposed to replace the ramp filter in the standard FDK algorithm on a circular trajectory by a first derivative composed with a Hilbert transform [115]. In other words, this algorithm is based on the FDK method but uses an alternative approach of filtering that decomposes the ramp kernel into the first derivative operator and the Hilbert transform.

The first derivative is local and gives accurate results even when the projections are truncated whereas the Hilbert transform is global and as a result is affected by truncations. However, when applying the first derivative operator, we obtain zeros in most of the regions and consequently the filtered data after the Hilbert transform are not influenced significantly by truncations. Hence, the structure of this algorithm is

the same as that of FDK with a different manner of filtering that can handle transverse truncations. Similarly, we first weight the computed projections. Then, the weighted datasets are filtered using the first derivative operator and the Hilbert transform(Eq. (4.9)). Finally, these filtered data are back-projected to get the reconstructed image. In this work, we applied this approach for the helical FDK reconstruction algorithm to deal with transversely truncated data.

4.2.2 FDK Algorithm Based on the 1D Laplace Operator

An important algorithm for circular ROI reconstruction named 2D approximate truncation resistant algorithm for computed tomography (ATRACT) has been published [33]. Similarly, it is based on the FDK algorithm but uses another approach of filtering that decomposes the ramp filter into the 2D Laplace operator coupled with a 2D Radon-based filtering operation. This algorithm is very efficient and gives artifact-free reconstructions when the projections are truncated transversely. The only drawback of this algorithm is the high computational cost of the 2D Radon-based filtering step. Later, this algorithm was optimized to further reduce the computational complexity by proposing another approach that replaces the ramp filter by the 1D Laplace operator and a 1D logarithmic-based filtering step [116]. An analytical proof of this algorithm, known as 1D ATRACT, was illustrated [117]. Briefly, the ramp kernel in the Fourier domain $|\sigma|$ can be reformulated as follows:

$$\begin{aligned} |\sigma| &= \sigma sgn(\sigma) \\ &= (2\pi i\sigma)^2 \left(-\frac{1}{4\pi^2}\frac{sgn(\sigma)}{\sigma}\right). \end{aligned} \tag{4.10}$$

The first term in this Eqn. corresponds to the Fourier transform of the 1D Laplace operator and the second term represents the Fourier transform of a logarithmic kernel. Knowing that multiplication in the Fourier domain refers to a convolution in the spatial domain, the ramp-filtered data P_R can be computed as

$$P_R(u_d, v_d, \lambda) = -\frac{1}{4\pi^2}\int_{-\infty}^{+\infty} \ln|u_d - u'_d| P_L(u'_d, v_d, \lambda)\, du'_d, \tag{4.11}$$

where P_L are the Laplace filtered data defined by

$$P_L(u_d, v_d, \lambda) = \frac{\partial^2}{\partial u_d^2} P'(u_d, v_d, \lambda). \tag{4.12}$$

Remind that P' are the cosine weighted projections defined previously in Eqn. (3.10). Thus, the ramp filter is mathematically identical to the Laplace operation (Eqn. (5.2)) and a 1D logarithmic-based filtering step (Eqn. (5.3). The Laplace operation is local and

hence is not influenced by truncations whereas the 1D logarithmic-based filtering is global but less sensitive to truncations compared to the 1D ramp filtering step because of its low-pass character.

This algorithm was also developed for reconstruction on circular trajectory. Similarly, our main contribution was to adapt it for helical scanning geometry using the same approach which was followed during the extension of the standard FDK algorithm from circular to helical trajectory.

4.2.3 Numerical Validation of the Proposed FDK-type Algorithms

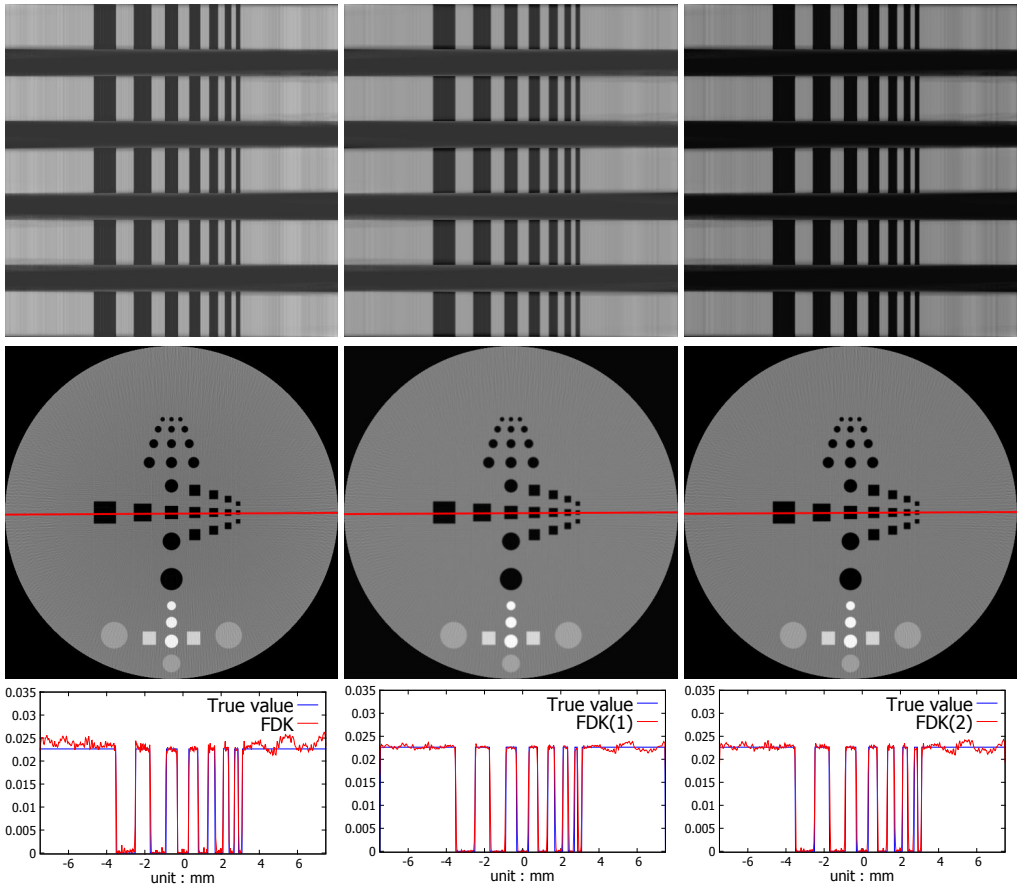

(A) FDK (B) FDK$^{(1)}$ (C) FDK$^{(2)}$

FIGURE 4.11: FDK-type reconstruction of the multi-disk phantom from complete noiseless projection data.

Firstly, we validated the implementation of the two algorithms using complete and noise-free data. These numerical validations are illustrated in Fig. 4.11 that represents a reconstruction of the CIVA multi-disk phantom from complete noiseless projection data. The first column corresponds to the standard FDK reconstruction whereas the

second and third columns refer to reconstruction results using the modified FDK algorithms which are based on the first derivative operator ($FDK^{(1)}$) and the 1D Laplace operator ($FDK^{(2)}$), respectively. A vertical and horizontal central slices of each reconstructed image are displayed in the first and second rows, respectively, with the red lines used for a 1D numerical comparison plotted in the third row. The three algorithms produce images of acceptable quality and as expected we do not see here any noticeable difference between them when projection data are complete.

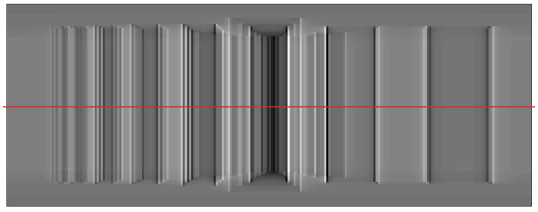

FIGURE 4.12: Non-truncated 2D projection filtered by the standard FDK algorithm.

As we have mentioned previously, the ramp filter of the FDK algorithm is the only non-local operation that denotes errors when data are truncated transversely. Thus, we will compare the impact of each filtering approach on transversely truncated data to show the advantages of the two proposed algorithms. Firstly, we show in Fig. 4.12 a filtered 2D projection obtained from complete data using the standard FDK algorithm. This filtered projection is the reference in our numerical comparison of 2D truncated projections filtered using the three described algorithms and that is illustrated in Fig. 4.13. In particular, figures 4.13a, 4.13b and 4.13c illustrate filtered 2D projections obtained from truncated data using FDK, $FDK^{(1)}$ and $FDK^{(2)}$ respectively. It is obvious that the filtering steps of $FDK^{(1)}$ (Fig. 4.13b) and $FDK^{(2)}$ (Fig. 4.13c) are much better than the ramp filter of the standard FDK algorithm that denotes a filtered sinogram (Fig. 4.13a) far from the reference (Fig. 4.12).

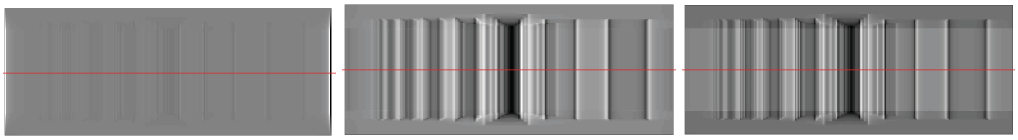

(A) FDK (B) $FDK^{(1)}$ (C) $FDK^{(2)}$

FIGURE 4.13: Truncated 2D projection filtered by the three described algorithm.

Fig. 4.14 represents reconstruction of the multi-disk phantom from truncated noiseless data. The configuration of truncation is the same as that illustrated previously in Fig. 4.9. The first column corresponds to the standard FDK reconstruction whereas the second and third columns correspond to $FDK^{(1)}$ and $FDK^{(2)}$, respectively. As we

can see, the standard FDK algorithm can not handle transverse truncation and severe distortions (cup artifacts) appear in the reconstruction. On the other hand, the two modified algorithms show reconstructions free of artifacts. The 1D profile comparison demonstrates that an important reconstruction offset appears with the standard FDK algorithm in case of truncated data whereas this offset is suppressed when using the two modified FDK algorithms.

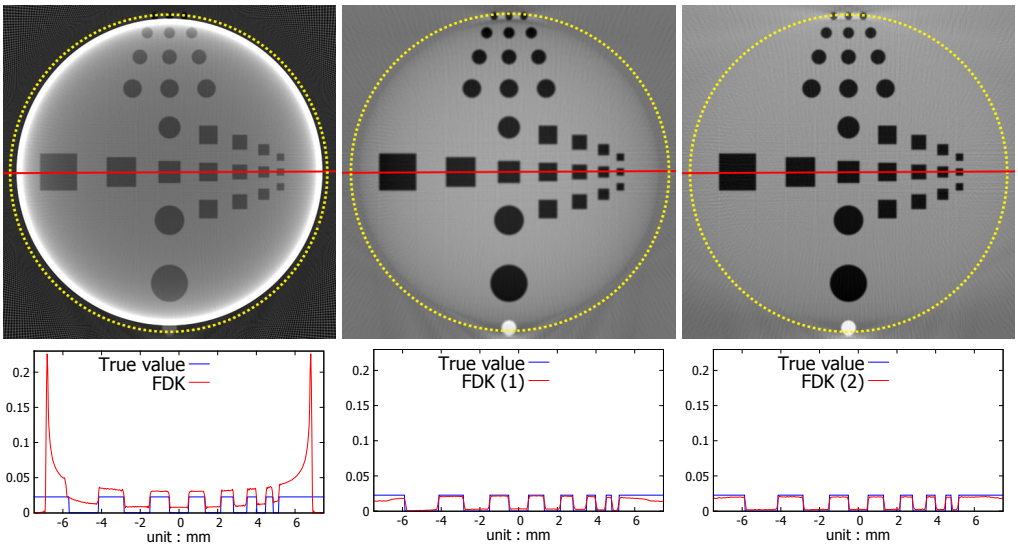

(A) FDK (B) FDK$^{(1)}$ (C) FDK$^{(2)}$

FIGURE 4.14: FDK-type reconstruction of the multi-disk phantom from truncated noiseless projection data.

It should be mentioned that for these two modified FDK algorithms a min-max scaling method was applied manually after reconstruction [117]. Without this step, the reconstruction suffers from a global scaling issue and the measured values are not quantitative. The final calibrated reconstructed values $f_c(i)$ are given by

$$f_c(i) = \frac{(f_r(i) - f_{r(min)})(f_{max} - f_{min})}{(f_{r(max)} - f_{r(min)})} + f_{min}, \tag{4.13}$$

where $f_{r(min)}$ and $f_{r(max)}$ are the minimum and maximum values in the reconstructed image f_r, respectively, while f_{min} and f_{max} correspond to the minimum and maximum attenuation values in the FOV of the original object, respectively, and which should be a priori known.

Finally, we aim to compare the performance of these two algorithms in case of noisy data. We show in Fig. 4.15 reconstruction from truncated noisy data with the same parameters as the noise-free situation. Gaussian noise with a standard deviation of 0.5% of the maximum value in the noise-free data was added prior to reconstruction. These simulation results demonstrate that the two modified FDK algorithms are robust to

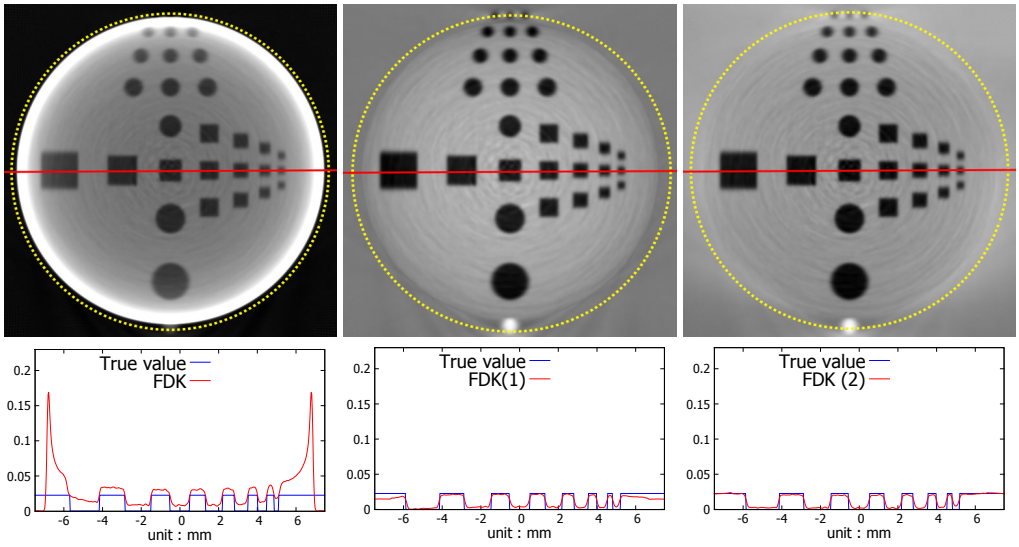

(A) FDK (B) FDK$^{(1)}$ (C) FDK$^{(2)}$

FIGURE 4.15: FDK-type reconstruction of the multi-disk phantom from truncated noisy projection data.

noise with a similar behavior between them and that can be noticed either by comparing the central slice of each reconstructed image or through analyzing the 1D profiles plotted along the red lines.

TABLE 4.4: Quantitative evaluation of the FDK-type algorithms.

Reconstruction algorithm	FDK	FDK$^{(1)}$	FDK$^{(2)}$
Reconstruction time (minutes)	52.5	52.4	54.2
Mean-square-error (complete data) $\times 10^{-6}$	5	6	6
Mean-square-error (truncated data) $\times 10^{-6}$	252.8	7	6

We can notice from the reconstruction time and MSE values illustrated in Table 4.4 that the two modified FDK algorithms have the same computational cost as that of the standard FDK algorithm and the measured MSE is the same for the three algorithms when data are non-truncated. The standard FDK algorithm shows large error when data are truncated, whereas this error is reduced significantly by the two proposed FDK-type algorithms.

4.3 Conclusions

We introduced in this chapter a theoretical overview of three reconstruction algorithms (FDK, FBP and BPF) adapted to helical scanning geometry which was proposed as a solution to deal with long objects. For performance evaluation, we presented a numerical

comparison of the three algorithms using data generated by CIVA. Our computer simulations showed reconstructions with both complete (noiseless and noisy) and transversely truncated data. In case of complete noiseless projection data, the FBP algorithm is the most accurate one. In terms of noise, we notice a better robustness of the FBP and BPF algorithms compared to the FDK algorithm that uses the standard ramp kernel which is a high-pass filter. However, it should be mentioned that the ramp filter could be combined with a smoothing window for a better response to noisy data. When the projections are truncated transversely, the FBP and BPF algorithms perform better than the FDK algorithm that uses the global ramp filter. In particular, these two algorithms solve the well-known cup artifacts usually observed with the FDK algorithm in the case of truncated data. Computationally speaking, the FBP and BPF algorithms are time-consuming compared to the approximate FDK algorithm because of their exactness property.

In these computer simulations a voxel-based implementation of the FBP algorithm was proposed and it was shown by numerical simulations the advantages of this approach over the PI-line based implementation developed originally by Zou and Pan.

We should remind that the BPF algorithm suffers from poor spatial resolution because of the performed interpolation step and as a result needs a large number of projections.

For these reasons, we have chosen to include the FBP algorithm in the next version of CIVA CT. Furthermore, the existing FDK algorithm in CIVA was extended from circular to helical trajectory. The FDK algorithm is preferred if the time of reconstruction is a priority and in case of reconstruction from limited-angle data because of its flexibility where it can be adapted to incomplete trajectories like a reverse helical trajectory in super-short-scan mode. This latter will be introduced in the next chapter.

In addition, we proposed two helical FDK-type algorithms that can handle transversely truncated data . For performance evaluation, we illustrated a numerical comparison of these two algorithms and the standard helical FDK algorithm. Our computer simulations showed reconstructions with both complete and transversely truncated data. There is no observable difference between the image quality of reconstruction from complete data with the three described algorithms. However, when the projections are truncated transversely, the two modified FDK algorithms show a better performance than the standard FDK algorithm.These two algorithms avoid transverse truncation artifacts (cup artifacts) and assure good image quality. Furthermore, the proposed algorithms were tested with noisy data and the obtained reconstruction results show their robustness against noise.

In terms of performance, the reconstruction time of the two modified FDK algorithms is similar to that of the standard FDK algorithm. It should be mentioned that

the two proposed FDK-type algorithms are of great interest because of their filtered-backprojection structure and consequently they are not time-consuming like backprojection-filtration and PI-line based algorithms or other iterative methods for local reconstruction.

Chapter 5

Limited-Angle CT Reconstruction

This chapter studies both analytical and iterative reconstruction algorithms with main focus on limited-angle trajectories. It consists of two sections. The first section is devoted to analytical reconstruction, whereas the second one concerns iterative reconstruction. While iterative reconstruction is directly adapted to limited-angle trajectories, we should handle data redundancy for analytical reconstruction.

In the first section, an analytical algorithm adapted to limited-angle reverse helical trajectory is proposed. This algorithm follows the general structure of FDK and can be applied to both half-scan and super-short-scan geometries. An advantage of this algorithm is that it can also handle transversely truncated data since the filtering operation follows the approach presented in the previous chapter.

In the second section, we present two regularized algebraic algorithms named: SART-FISTA-TV and DART-FISTA-TV that perform well with limited-angle trajectories and that are supposed to give good reconstruction even if the scanning angle of the trajectory is relatively small. Due to their iterative nature, these two algorithms are flexible and could be applied to arbitrary scanning trajectories.

The validation and evaluation of these algorithms are based on CIVA-simulated data of the multi-disk phantom shown previously. Missing data configurations like limited-angle data, truncated data and few-view projections are used to test these algorithms. Based on the numerical results obtained, some remarks are concluded regarding the pros and cons of each algorithm when reconstructing with such configurations.

5.1 FDK-type Algorithm

Recently, three FDK-type reconstruction methods adapted to the reverse helical trajectory were proposed [140]. The filtering step in these methods is based on the ramp or Hilbert kernel. From the general structure of these methods, we propose an FDK-type algorithm for limited-angle reverse helical trajectory. This algorithm is based on a filtering operation combining the 1D Laplace operator with a logarithmic kernel and

which was described in the previous chapter. Thus, this proposed algorithm can deal with both limited-angle and transversely truncated data.

5.1.1 Algorithm Description

The structure of this algorithm consists of the following steps:

1. Cosine weighting and dealing with data redundancy:

$$P'(u_d, v_d, \lambda) = \frac{D}{\sqrt{D^2 + u_d^2 + v_d^2}} W(u_d, v_d, \lambda) P(u_d, v_d, \lambda). \tag{5.1}$$

2. Filtering weighted projection data:

$$P_L(u_d, v_d, \lambda) = \frac{\partial^2}{\partial u_d^2} P'(u_d, v_d, \lambda), \tag{5.2}$$

$$P_f(u_d, v_d, \lambda) = -\frac{1}{4\pi^2} \int_{-\infty}^{+\infty} \ln|u_d - u'_d| P_L(u'_d, v_d, \lambda)\, du'_d. \tag{5.3}$$

3. Back-projection:

$$f^+(\overrightarrow{r}) = \int_0^{\lambda_m} \frac{RD}{|R - \overrightarrow{r} \cdot \overrightarrow{e_w}(\lambda)|^2} P_f(u_d, v_d, \lambda)\, d\lambda, \tag{5.4}$$

$$f^-(\overrightarrow{r}) = \int_{-\lambda_m}^{0} \frac{RD}{|R - \overrightarrow{r} \cdot \overrightarrow{e_w}(\lambda)|^2} P_f(u_d, v_d, \lambda)\, d\lambda. \tag{5.5}$$

4. Fusion:

$$f(\overrightarrow{r}) = f^+(\overrightarrow{r}) F^+(z) + f^-(\overrightarrow{r}) F^-(z). \tag{5.6}$$

In these equations, we use the same notations shown previously in Chapter 3. As illustrated in Fig. 5.1, the X-ray source S moves on a reverse helical trajectory of radius R and angular range $150°$ (rotation reversal every $150°$). The coordinates of S in the system $(\overrightarrow{e_x}, \overrightarrow{e_y}, \overrightarrow{e_z})$ are denoted by

$$\overrightarrow{y}(\lambda) = (R\cos((-1)^n\lambda), R\sin((-1)^n\lambda), \frac{2\pi h}{l}\lambda) \qquad \lambda \in [\lambda_{min}, \lambda_{max}], \tag{5.7}$$

where l is the angular range of each turn and n is the turn index number. Remind that λ_{min} and λ_{max} are the endpoints of the rotation angle λ and $2\pi h$ is the helical pitch.

In Eqn. (5.1), $W(u_d, v_d, \lambda)$ represents a weighting function proposed previously by Noo et al. [79] to handle redundant data. This function is based on the Parker

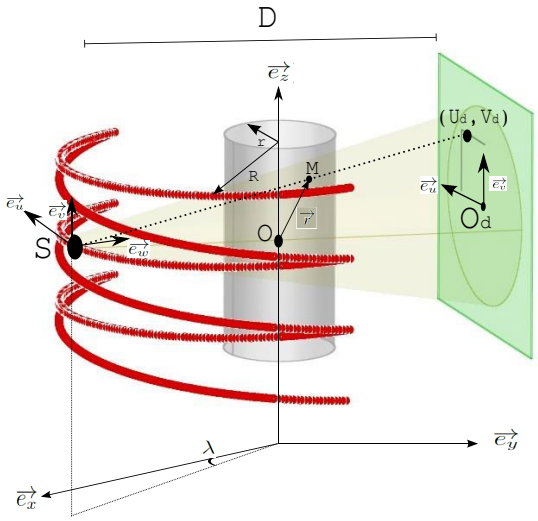

FIGURE 5.1: Limited-angle reverse helical CB acquisition geometry and associated notations.

weighting function [88] and is expressed by:

$$W(u_d, v_d, \lambda) = \frac{c(\lambda)}{c(\lambda) + c(\lambda + \pi - 2\arctan(u_d/D))}, \tag{5.8}$$

where $c(\lambda)$ is a smooth function which vanishes outside $[-\lambda_m, \lambda_m]$ with $-\lambda_m$ and λ_m are the endpoints of the lower and upper helical turns corresponding to the point M defined by the position vector $\vec{r}$.

To explain the fusion process, we consider two helical turns defined by the endpoints $-\lambda_m$ and λ_m as illustrated in Fig. 5.2. Using data from these lower and upper helices, respectively, we can reconstruct two functions $f^-(\overrightarrow{r})$ and $f^+(\overrightarrow{r})$ and merge them to obtain $f(\overrightarrow{r})$. The two fusion weighting functions $F^-(z)$ and $F^+(z)$ are defined by:

$$F^-(z) = \begin{cases} 1 & (-H + 0.5L_F) \leq z \leq -0.5L_F \\ cos^2\left(\frac{\pi(z+0.5L_F)}{2L_F}\right) & -0.5L_F < z \leq 0.5L_F \\ 0 & \text{otherwise,} \end{cases} \tag{5.9}$$

$$F^+(z) = \begin{cases} 1 & 0.5L_F \leq z \leq (H - 0.5L_F) \\ sin^2\left(\frac{\pi(z+0.5L_F)}{2L_F}\right) & -0.5L_F \leq z < 0.5L_F \\ 0 & \text{otherwise,} \end{cases} \tag{5.10}$$

where L_F is the length of the zone within which fusion is performed and H is the z-range of each function $f^-(\overrightarrow{r})$ and $f^+(\overrightarrow{r})$. Further explanations for the case of more than two helical turns have been illustrated [136].

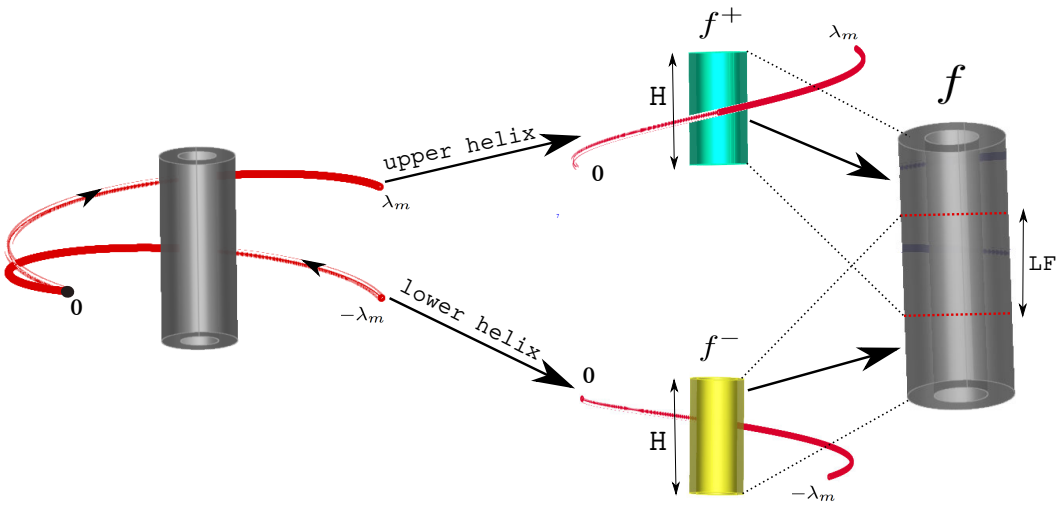

FIGURE 5.2: Illustration of the fusion process.

5.1.2 Numerical Validation

TABLE 5.1: Numerical simulation parameters.

Object radius (r)	7.5 mm
Helix radius (R)	20 mm
Source-detector distance (D)	40 mm
Helical pitch (2πh)	2.05 mm
Total number of turns	9
Number of projections per turn	300
Detector sampling	256×256 pixels
Detector pixel size	0.14×0.14 mm^2
Reconstruction matrix	$512 \times 512 \times 512$ voxels

The evaluation of this algorithm is based on CIVA-simulated data of the multi-disk phantom. Two scanning angles of the reverse helix are considered. The first one corresponds to the half-scan geometry with an angular range of $240°$ and the second one corresponds to the super-short-scan geometry with an angular range of $150°$. Remind that half-scan geometry refers to a scan over $180°$ plus the opening angle of the X-ray beam and provides the minimum data required for image reconstruction. On the other hand, in case of super-short-scan geometry, there are missing data and reconstruction of the whole object is difficult and may be impossible if the scanning angle is very small.

Due to the low computational cost of the FDK-type algorithm compared to iterative reconstruction methods, we implemented the algorithm on a single-core CPU. We

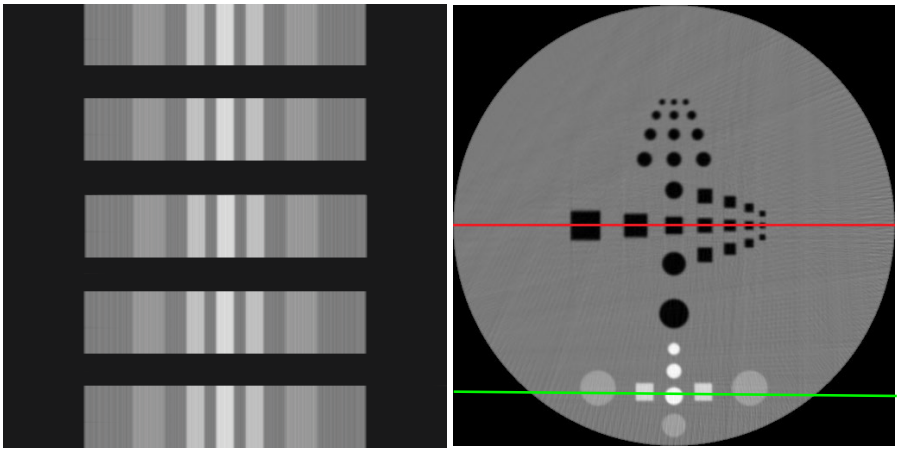

(A) Vertical slice (B) Horizontal slice

FIGURE 5.3: FDK-type reconstruction from noiseless projections generated on a reverse helical trajectory with angular range limited to 240°.

test the robustness of the algorithm to noisy and truncated data. The data acquisition parameters are given in Table 5.1.

Figure 5.3 presents reconstruction results with the half-scan geometry (240°) and from complete noiseless projections. A horizontal and a vertical slice of the reconstructed volume are illustrated. The shown vertical slice (see Fig. 5.3a) is the one containing the green line illustrated in Fig. 5.3b. These obtained results are satisfying and demonstrate the validity of the proposed algorithm. For quantitative comparison, 1D profiles along the red and green lines are given in Fig. 5.4. These profiles confirm that the reconstructed values are correct and agree well with the original ones.

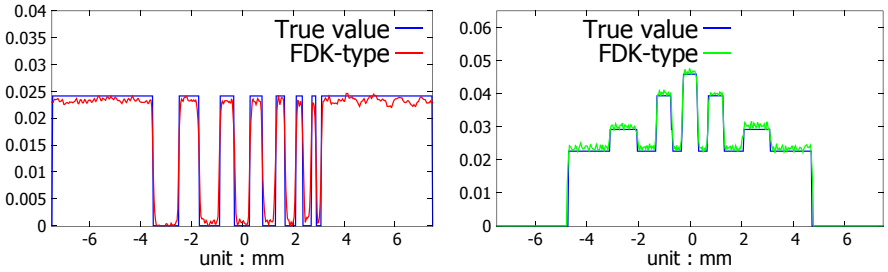

FIGURE 5.4: 1D numerical comparison along the red and green lines plotted in Fig. 5.3.

We aim to study the behavior of the algorithm with respect to transversely truncated data. The configuration of data truncation is similar to that shown in the previous chapter where the FOV is reduced to its half-size. The reconstruction results from truncated noiseless data are presented in Fig. 5.5 where the yellow dashed-region corresponds to the ROI viewed by the detector. Within this configuration, the half-scan geometry is used again. It can be observed that the developed FDK-type algorithm is

very efficient and there are no artifacts in the reconstruction neither due to data truncation nor due to limited-angle data. For quantitative evaluation, a 1D profile is traced along the red line and it can be noticed that the reconstructed values agree well with the original ones.

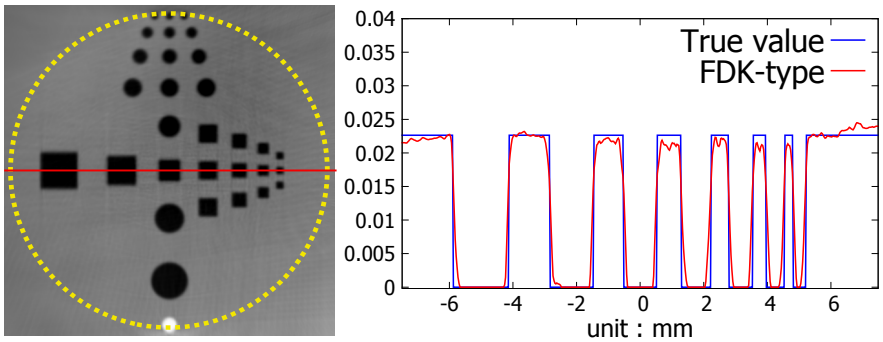

FIGURE 5.5: FDK-type reconstruction from truncated noiseless data generated on a reverse helical trajectory with angular range limited to $240°$.

In order to show the robustness of the algorithm to noise, we added Gaussian noise to the truncated noiseless projection data. The standard deviation of this Gaussian noise is 0.5 % of the maximum value in the noise-free projections. The reconstruction results from truncated noisy data are displayed in Fig. 5.6 that illustrates a ROI in the horizontal slice of the reconstructed volume and a 1D numerical comparison along the red line. Although the image quality is a little worse than the one obtained in the absence of noise, these reconstruction results are acceptable and the algorithm is not so sensitive to noisy data.

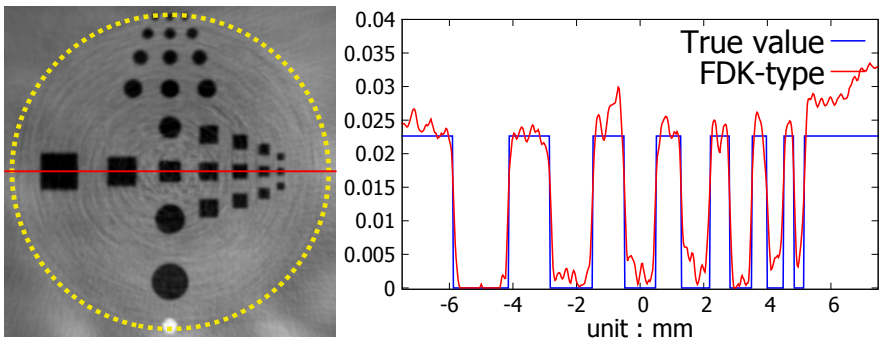

FIGURE 5.6: FDK-type reconstruction from truncated noisy data generated on a reverse helical trajectory with angular range limited to $240°$.

Reconstruction from a few number of projections is studied also. For this purpose, the number of projections per helical turn is reduced from 300 to 50. We show in Fig. 5.7 the reconstruction results obtained from this small number of complete noiseless projections. A horizontal and a vertical slice of the reconstructed volume are illustrated and it is clear that there is a significant loss of contrast and resolution in the

reconstructed image and the reconstruction is affected by streak artifacts. This result is expected since the proposed algorithm is an analytical one and the sampling must be sufficient enough to satisfy the Nyquist sampling theorem.

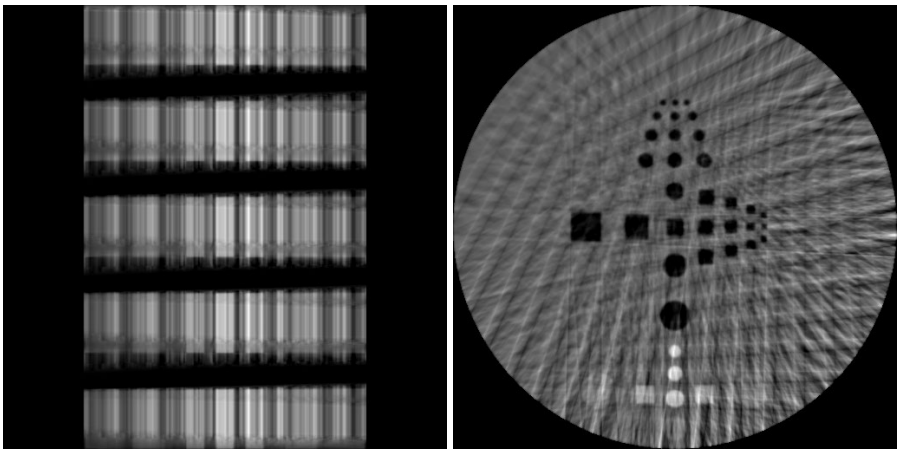

(A) Vertical slice (B) Horizontal slice

FIGURE 5.7: FDK-type reconstruction from a few number of complete noiseless projections generated on a reverse helical trajectory with angular range limited to $240°$.

Finally, we aim to study the performance of the algorithm when the scanning angle of the trajectory of acquisition is reduced more. We present reconstruction from a reverse helical trajectory with an angular range of $150°$ which is significantly smaller than the half-scan range. In fact, it has been mentioned that for an exact ROI reconstruction from fan-beam projections on less than a short scan, each line passing through the ROI must intersect the source trajectory [79]. Knowing that FDK is an extension of the FBP algorithm from fan-beam into CB geometry, we show in Fig. 5.8 a horizontal slice of the phantom and we illustrate the ROI (region below the dashed-line) that we can reconstruct correctly with the FDK-type algorithm within such incomplete trajectory.

The reconstruction results are illustrated in Fig. 5.9 where a horizontal and a vertical slice are shown with a 1D numerical comparison corresponding to the red line plotted along the horizontal slice. It can be seen that the proposed algorithm succeeded in reconstructing the ROI defined by the yellow dashed-region and the reconstructed values along the 1D profile are very close to the original ones. However, the reconstruction outside this region is not good enough and some artifacts are visible. To suppress these artifacts caused by missing data and that is known to be the limitation of analytical reconstruction algorithms, we will study two iterative methods in the next section.

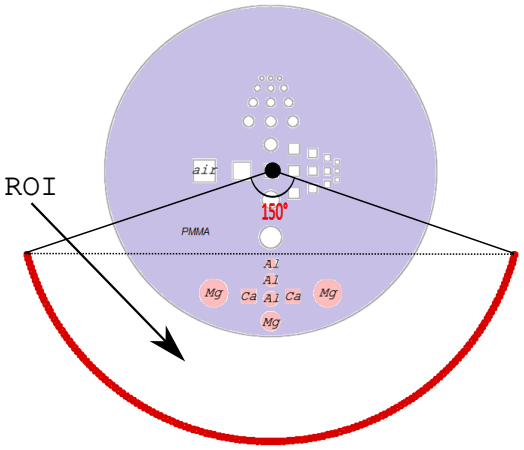

FIGURE 5.8: ROI of the object defined by source trajectory in red.

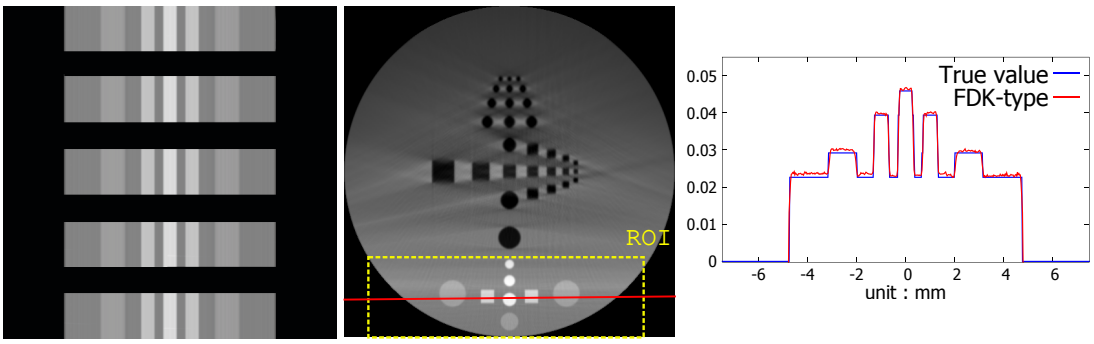

FIGURE 5.9: FDK-type reconstruction from complete noiseless data generated on a reverse helical trajectory with angular range limited to $150°$.

5.2 Regularized Algebraic Algorithms

For our application case, a sufficient amount of statistical information is available. In addition, prior information about the materials in the object could be known and this can be exploited in algebraic reconstruction. Thus, among iterative algorithms described in Chapter 3, we choose algebraic ones. In particular, we present in this section two regularized algebraic methods that minimize the TV of the image. TV minimization [95] is a regularization term that enforces smoothness in the reconstructed image to account for unrealistic variations between neighboring. This regularization tends to smooth out noise while preserving image edges. In addition, both algorithms integrate fast iterative shrinkage-thresholding algorithm (FISTA) technique [9] to speed up the convergence speed. The first algorithm named SART-FISTA-TV is based on SART which is commonly used for iterative reconstruction and the second one is called

DART-FISTA-TV and is based on DART. We illustrate here the structure of each algorithm and we evaluate numerically the performance of each one.

5.2.1 SART-FISTA-TV

This algorithm consists of three main steps: i) SART update (explained in Chapter 3), ii) TV minimization and iii) FISTA acceleration technique. In other words, this algorithm is similar to SART-TV [131] with an additional acceleration step.

TV minimization has been one of the most popular regularization methods up to date to reduce artifacts for image reconstruction from few-view or limited-angle data. This optimization problem which was inspired by compressed sensing (CS) theory [34] was already applied to circular cone-beam CT [96] and expressed as

$$\vec{f}^{*} = argmin\|\mathbf{f}\|_{TV}, \text{subject to } |A.\vec{f}^{*} - p| < \epsilon, \tag{5.11}$$

where $\vec{f}^{*}$ is the volume image to be reconstructed, ϵ is a parameter that corresponds to the level of data inconsistency tolerance and $\|\mathbf{f}\|_{TV}$ is the l_1-norm of the image gradient magnitude which is utilized as the cost function and represented by

$$\|\mathbf{f}\|_{TV} = \sum_{i,j,k} \sqrt{(f_{i,j,k} - f_{i-1,j,k})^2 + (f_{i,j,k} - f_{i,j-1,k})^2 + (f_{i,j,k} - f_{i,j,k-1})^2} \tag{5.12}$$

with $f_{i,j,k}$ is the value of the voxel with index (i, j, k).

Standard techniques like conjugate gradients or steepest descent were used to solve Eqn. (5.11). TV regularization can be optimized by introducing an anisotropic TV minimization approach [18, 48] dedicated to limited-angle CT. This technique takes the scanning range as additional prior knowledge and provides higher image quality than the standard TV counterpart when reconstructing from limited-angle data.

The FISTA acceleration step is denoted by

$$f^{(m+1)} = f^{m} + \left(\frac{t^{m} - 1}{t^{(m+1)}}\right)\left(f^{m} - f^{(m-1)}\right), \tag{5.13}$$

where the parameter t is updated at each iteration as follows

$$t^{(m+1)} = \frac{1 + \sqrt{1 + 4\,(t^{m})^2}}{2}, \tag{5.14}$$

with t = 1 is the initial given value and m is the index of the global iteration step.

In this implementation, the standard TV regularization is considered and a gradient descent method is used to minimize $\|\mathbf{f}\|_{TV}$. Non-negativity constraint is considered as well. Knowing that these iterative approaches are computationally intensive compared

to analytical ones, the CB projection and back-projection steps are accelerated. The projection (pixel-driven) and backprojection (ray-driven) steps are implemented on a Graphics Processing Unit (GPU) using C-CUDA on nVidia TITAN card. We apply 50 iterations to ensure that convergence is reached.

The steepest gradient method used to minimize the TV objective function is based on an iterative scheme where the image is updated each iteration n as follows

$$f^{(n+1)} = f^{(n)} - \alpha \cdot d_p \cdot \frac{df^n}{|df^n|}, \tag{5.15}$$

with

$$d_p = |f - f_0| \tag{5.16}$$

and

$$df^n = \nabla_f \|f\|_{TV}. \tag{5.17}$$

The value of d_p is computed initially and depends on the values of f_0 and f corresponding to the image values before and after the SART update step, respectively. ∇ represents the gradient operator and α is a parameter to control the effect of regularization. In our numerical simulations we choose $\alpha = 0.2$ and the number of iterations for TV minimization is set to 10.

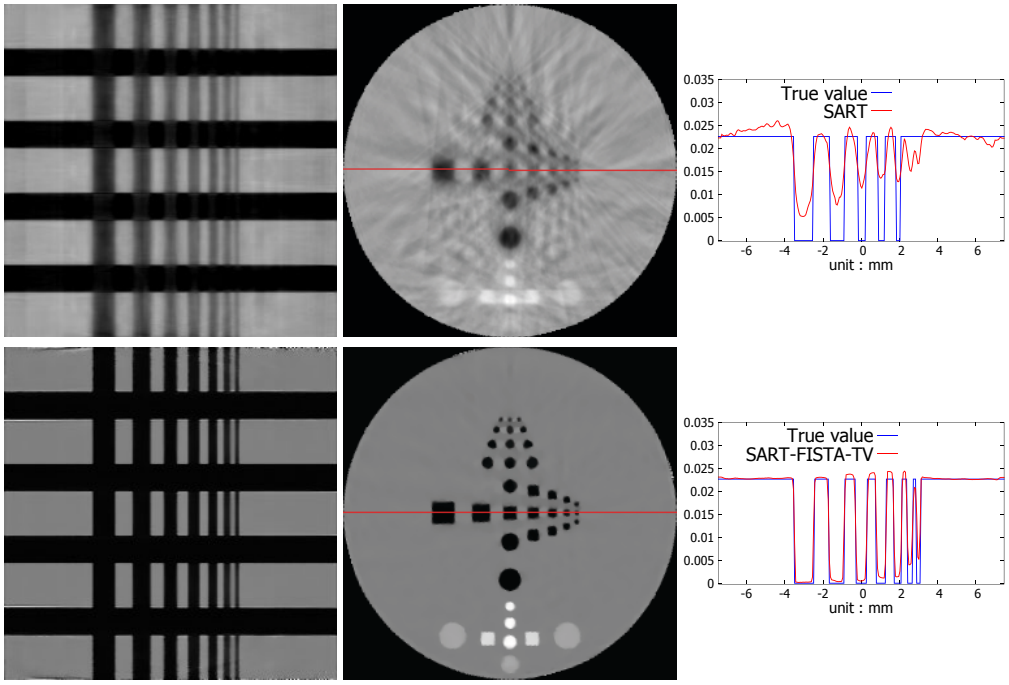

FIGURE 5.10: SART (first row) and SART-FISTA-TV (second row) reconstruction from noiseless data simulated on a reverse helix of angular range limited to $150°$ and with only 10 projection views per helical turn.

We show the robustness of this iterative approach against CB artifacts obtained previously with the FDK-type algorithm when the scanning angle is smaller than the short scan range. We perform two sets of studies that consider reconstruction on a reverse helix with angular range limited to $150°$ with the presence and absence of noise. The data acquisition parameters are identical to those specified in the previous section, but the projection data are reduced from 300 views per helical turn to only 10 views per helical turn. The reconstructed volumes are composed of only $256 \times 256 \times 256$ cubic voxels because of the high computational cost and memory demands.

To show the advantages of the integrated regularization step, SART-FISTA-TV results are shown together with SART. Horizontal and vertical slices of the volumes reconstructed by the use of SART-FISTA-TV and SART are illustrated in Fig. 5.10. The SART-FISTA-TV reconstruction appears to be accurate, whereas SART reconstruction shows significant artifacts due to limited-angle data. In addition, there are streak artifacts caused by the limited number of projections. The reconstruction values are illustrated quantitatively by plotting 1D profiles along the red lines in the horizontal slices. These reconstructed values obtained by the use of SART-FISTA-TV are not exactly identical to the original ones and a small difference error is obtained. However, this error can be accepted and is very small compared to the large error obtained by the use of SART.

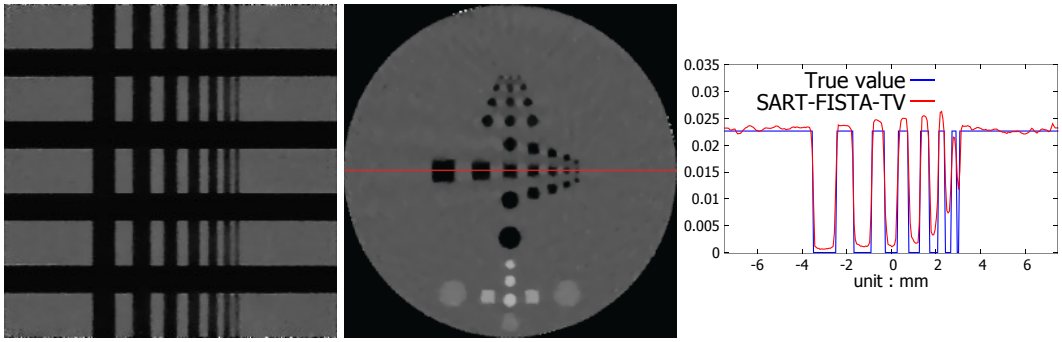

FIGURE 5.11: SART-FISTA-TV reconstruction from noisy data simulated on a reverse helix of angular range limited to $150°$.

We investigate the robustness of the algorithm to noisy data by adding Gaussian noise to the projection data, where the standard deviation σ of this Gaussian is set to 0.5 % of the maximum value in the noiseless data. Fig. 5.11 shows SART-FISTA-TV reconstruction from noisy data. A horizontal and a vertical slice through the reconstructed volume are illustrated with a 1D numerical comparison for quantitative evaluation. When noisy data are introduced, the algorithm appears to be stable. It can be seen that image quality is degraded slightly and the 1D profile becomes less accurate. However, these results are not surprising considering that there are only 10 projection

views per helical turn and we can expect that the robustness of the algorithm to noisy data becomes better when the number of projections increases.

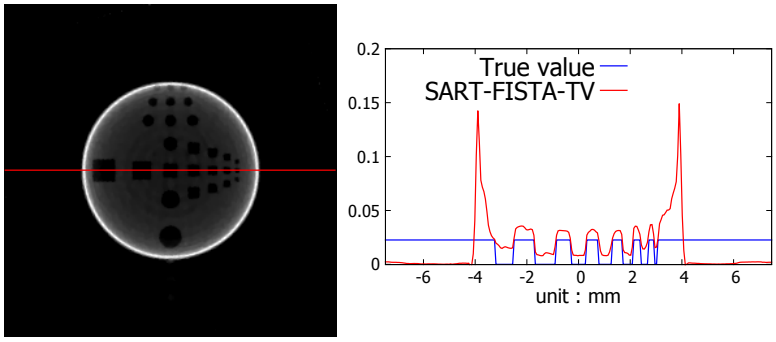

FIGURE 5.12: SART-FISTA-TV reconstruction of the multi-disk phantom from noiseless truncated projection data.

A final study is performed to investigate the behavior of this algorithm when data are truncated transversely. In this simulation, we aim to study the impact of truncated data only; hence the angular range of the helix is 360°. The width of the detector is reduced to its half size and the reconstruction results are shown in Fig. 5.12. It can be seen that severe cup-artifacts appear in the illustrated horizontal slice of the reconstructed volume. The numerical comparison along the red line shows a large offset between the original values in blue and the reconstructed ones in red. Thus, this algorithm does not perform well when data are truncated.

5.2.2 DART-FISTA-TV

DART-FISTA-TV algorithm is an algebraic algorithm that combines DART with TV regularization and FISTA technique. Remind that DART can incorporate prior knowledge about the different materials (attenuation coefficient) of the scanned object into the reconstruction process. If we refer to the schematic view of DART illustrated in Fig. 3.6 of Chapter 3, we notice that a Gaussian smoothing step is applied at the end of each iteration. The objective of this step is to reduce the fluctuations over the boundary pixels and to deal with noise. We propose here to replace the Gaussian smoothing step by TV minimization combined with FISTA. It is known that TV minimization has the advantage of reducing noise while preserving image edges and performs better than Gaussian smoothing. Similarly, the advantages of FISTA technique is speeding up the convergence. The only drawback here is that TV minimization step is more costly than Gaussian smoothing and it is supposed to increase the overall computational cost of the algorithm. A schematic view of the proposed algorithm is shown in Fig. 5.13. In

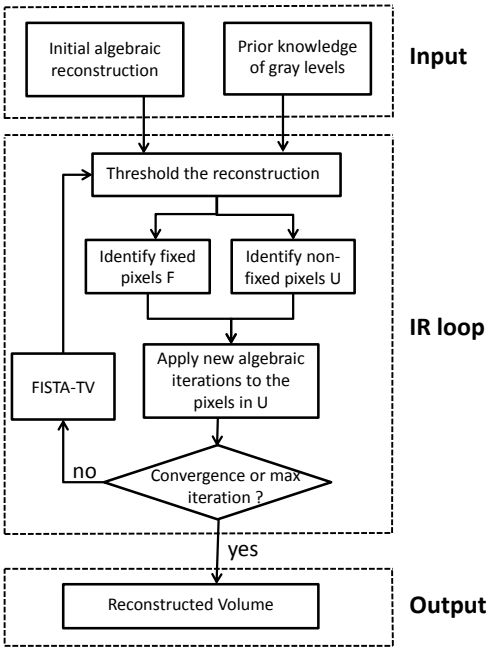

FIGURE 5.13: Schematic view of DART-FISTA-TV reconstruction process.

our performed numerical simulations, SIRT algorithm is chosen for algebraic reconstruction in each iteration and similarly the reconstructed values are enforced to be positive.

For numerical validation of the proposed algorithm, the CIVA multi-disk phantom is used again. We assume a prior knowledge of the attenuation coefficients corresponding to the different materials (PMMA, Mg, Al and Ca) of the object. Data acquisition configuration used previously with SART-FISTA-TV simulations is considered. Similarly, we deal here with both limited-angle (reverse helix of 150° angular range) and few-view (10 projections per helical turn) projection data. In Fig. 5.14, horizontal and vertical slices of the reconstructed volumes from noise-free projections are shown for SART-FISTA-TV and DART-FISTA-TV in the first and second rows, respectively. Visually, DART-FISTA-TV appears to provide improved image reconstruction over SART-FISTA-TV and gives more accurate reconstruction as we can see from the 1D numerical comparison plotted along the red line.

To show the advantages of the modifications we proposed over the original DART algorithm, we show in Fig. 5.15 reconstruction for the case where Gaussian noise is added prior to reconstruction. This Gaussian is of zero mean and standard deviation $\sigma = 0.5\%$ of the maximum value in noiseless data. The DART-FISTA-TV results clearly

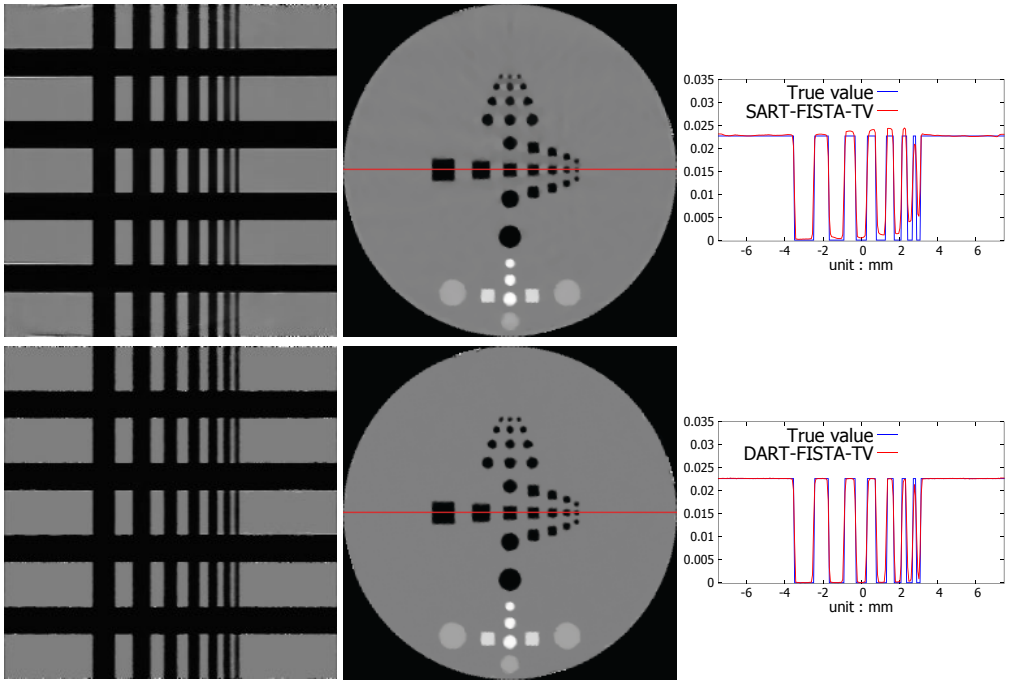

FIGURE 5.14: SART-FISTA-TV (first row) and DART-FISTA-TV (second row) reconstruction of the multi-disk phantom from noiseless data.

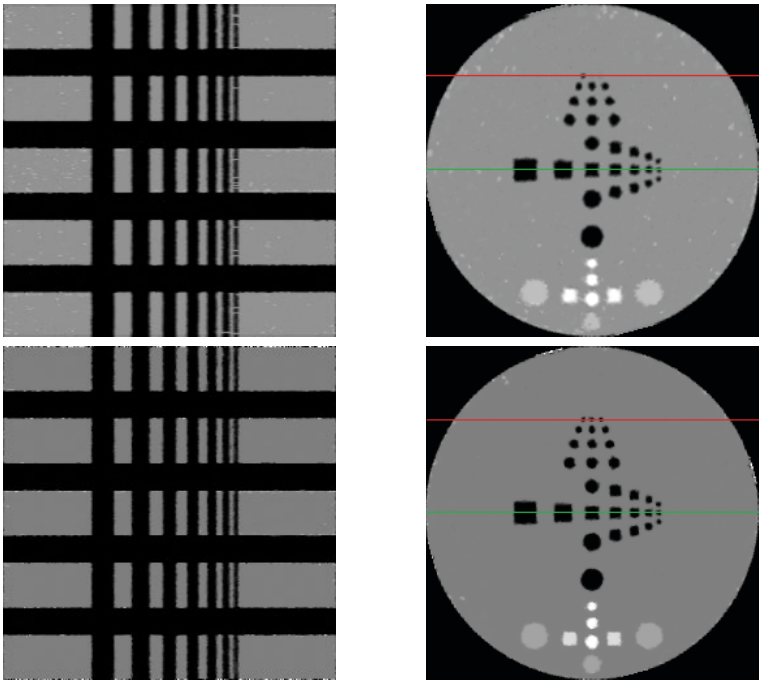

FIGURE 5.15: DART (first row) and DART-FISTA-TV (second row) reconstruction of the multi-disk phantom from noisy data.

show fewer noise artifacts than that of DART. Furthermore, it shows better spatial resolution where it recovers the three tiny holes along the red line in contrast to DART

which recovers only one hole.

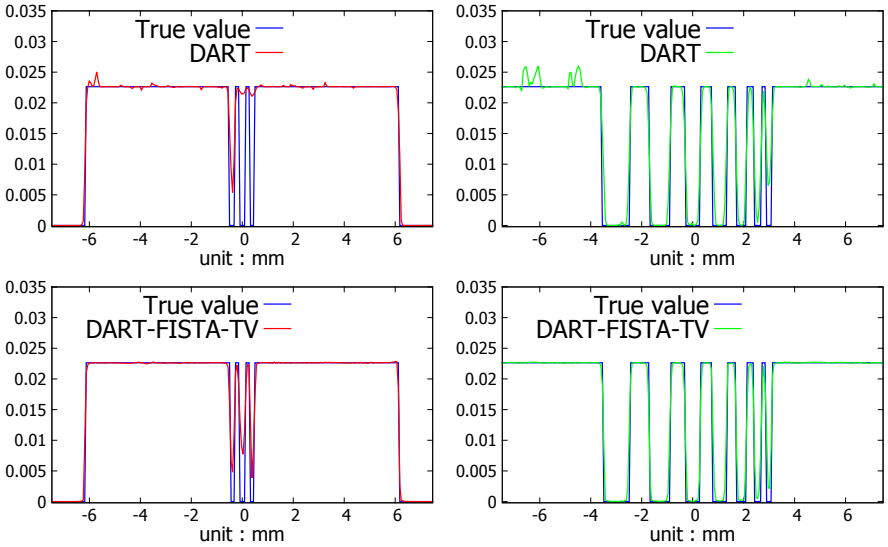

FIGURE 5.16: 1D numerical comparison along the red and green lines plotted in Fig. 5.15.

Fig. 5.16 shows 1D profiles along the red and green lines illustrated previously in Fig. 5.15. This 1D numerical comparison demonstrates that DART-FISTA-TV can reduce noise and give more accurate reconstruction values than DART.

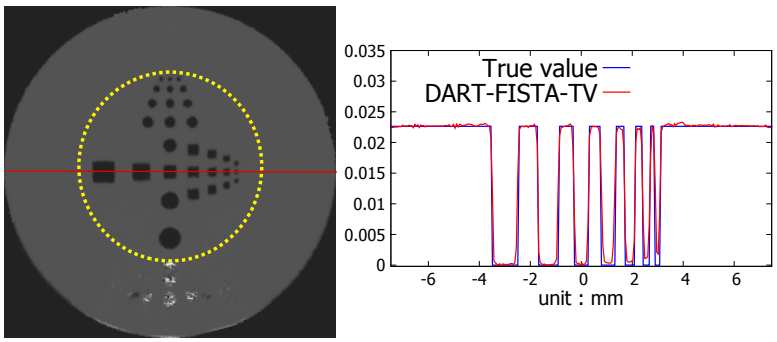

FIGURE 5.17: DART-FISTA-TV reconstruction of the multi-disk phantom from noiseless truncated projection data.

Finally, we study the robustness of DART-FISTA-TV to truncated data. The used detector is of smaller width reducing the FOV to its half-size. In this simulation, noiseless projection data are acquired along a reverse helix of 9 turns with scanning angle limited to 150° and 10 projections per turn. In total, we have 90 projection views. We are dealing here with three kinds of missing data: few-view, limited-angle and transversely truncated data. Thus, the reconstruction problem is severely ill-posed. We show a horizontal slice of the reconstructed volume in Fig. 5.17 with the yellow-dashed region

referring to the ROI contained in the FOV and the red line used for 1D numerical comparison. It is clear that the reconstructed image is of high quality and the reconstructed values are very close to the original ones even if data are truncated and the projection views are few and of limited range.

TABLE 5.2: Reconstruction time comparison of the described algorithms.

Reconstruction algorithm	FDK	SART-FISTA-TV	DART-FISTA-TV
Number of views per helical turn	300	10	10
Total number of projections	2700	60	60
Implementation	single-core CPU	GPU	GPU
Reconstruction time (minutes)	7.1	91.3	73.9

The reconstruction time of these iterative algorithms is studied and compared with that of the proposed FDK-type algorithm. We consider in this comparison that the scan range is limited to 150° and the image volume is reconstructed over 256^3 voxels. This comparison is illustrated in Table 5.2 and we can notice that the FDK-type algorithm is the most rapid one with a reconstruction time of 7.1 minutes although the algorithm is implemented on a single-core CPU and the total number of projections used is 2700 that is considered large. Concerning the iterative algorithms, the projection and back-projection steps are accelerated using parallel GPU implementations and the total number of projections is 60 which is 45 times smaller than that used with the FDK-type algorithm. The reconstruction time of SART-FISTA-TV is 91.3 minutes whereas that of DART-FISTA-TV is 73.9 minutes. As expected, these iterative algorithms are computationally more intensive than the FDK-type algorithm. DART denotes a reconstruction time of 53.9 minutes which is smaller than that of our proposed DART-FISTA-TV algorithm because the integrated TV regularization technique is more costly than Gaussian smoothing.

5.3 Conclusions

We focused in this chapter on the problem of image reconstruction from limited-angle data. We presented both analytical and iterative approaches to deal with this problem. Again, a helical-like scanning trajectory was considered for numerical comparison illustration. In total, three algorithms were presented and the main objective was their validation and comparing their performance with realistic simulated data. In addition to limited-angle data, the algorithms were evaluated also with other missing data configurations like truncated data and few-view projections.

In the first part, we proposed an algorithm of FDK-type which is adapted to the reverse helical trajectory with limited angular range and that can also deal with transversely truncated data. The algorithm was validated on such scanning trajectory with

both half-scan and super-short-scan geometries. An interesting point about this algorithm is its high speed and low computational cost. For half-scan geometry, the obtained results were accurate and the whole object was reconstructed well when a sufficient number of projection views is available. Furthermore, the algorithm showed a good performance even when the projections acquired on this incomplete trajectory were truncated and noisy. In other words, it was illustrated that this algorithm can handle the two main problems discussed in the thesis: limited-angle data and transversely truncated data. However, in the case of super-short-scan geometry, only a region in the object could be reconstructed correctly and this was expected due to the analytical nature of the algorithm. Another limitation of this algorithm which comes from its analytical nature is demanding a large number of projections, where we illustrated that the reconstruction was affected by streak artifacts when the number of projections is small.

In the second part, we proposed two regularized algebraic iterative algorithms: SART-FISTA-TV and DART-FISTA-TV. These two algorithms are computationally more intensive than the FDK-type algorithm, but they improve the image quality significantly when the scanning angle is relatively small and less than the half-scan range. In addition to improvements in image quality, the source/detector positioning of these algorithms is highly flexible and thus they work with arbitrary trajectories which is important for future use of the robotic platform. We showed by numerical simulations that these algorithms are capable of reconstructing the whole object even if the angular range is limited to $150°$. As expected, these algorithms work well with very few number of projections and no streak-like CB artifacts appear in the reconstruction. In terms of speed, DART-FISTA-TV is slower than SART-FISTA-TV but in general their computational cost is similar when compared to the FDK-type algorithm which is very rapid. DART-FISTA-TV demands a prior knowledge on the attenuation coefficients of the inspected object, but this algorithm provides the best image quality among the described ones and is accurate even when data are truncated, noisy and acquired on incomplete trajectories. The major limitation of this algorithm when dealing with real experimental data is the possibility to know the attenuation coefficients exactly and which is difficult due to the polychromatic aspect of the X-ray source. This difficulty was not solved in our current implementation. However, some methods were already developed to solve this problem by estimating the optimal values of these attenuation coefficients automatically. These methods could be integrated in our algorithm for applying DART-FISTA-TV on experimental data. Another limitation of this algorithm is that it can not be applied to an object composed of more than five materials. Remind that DART-FISTA-TV was an extension of a developed algorithm named DART. Our idea was integrating TV minimization in the original DART algorithm and accelerating

the convergence speed using a technique called FISTA. We performed computer simulations to illustrate the advantages of DART-FISTA-TV over DART when adding noise to the projections.

In conclusion, each of these proposed algorithms has its pros and cons and one method may be preferred to the other depending on data acquisition configuration. For example, the rapid FDK-type algorithm is very interesting if the trajectory scanning angle is not smaller than the half-scan angle and if the number of acquired projections is sufficient enough. When the angular range is very small and we aim to reconstruct the whole object, the proposed iterative algorithms are a good choice. Here, SART-FISTA-TV is capable of providing acceptable results. Moreover, if a prior knowledge of the attenuation coefficients in the object is available, DART-FISTA-TV may be used for more accurate reconstruction.

Chapter 6

Experimental Results of Robotic CT Platform

This chapter presents reconstruction results from real data obtained with the robotic inspection platform. The proposed algorithms shown in Chapters 4 and 5 are used for reconstruction. Three different inspections are defined in these experimental studies. The first one is the helical scanning trajectory and the two other inspections consider reconstruction from truncated data and limited-angle data. For each inspection a reconstruction algorithm is selected based on the previous numerical results that we have shown during evaluating the different proposed algorithms. In summary, three algorithms are used: helical FDK, FDK$^{(1)}$ and SART-FISTA-TV. Remind that FDK$^{(1)}$ is the helical FDK algorithm that replaces the ramp filter kernel with the Hilbert transform and the first derivative operator.

The chapter is divided into three sections. We describe in the first section the robotic inspection platform where we give main characteristics of the used robots, X-ray equipments and we introduce a robotic software that is used to check if the defined trajectory is accessible by the robots. In the second section, we show reconstruction results from real data obtained from different inspections. Finally, some conclusions are given in the third section.

6.1 Robotic CT System Setup

X-ray equipment consists of a Viscom 225 kV micro-focus tube with a tungsten target and a Perkin Elmer flat panel detector with a pixel size of 200 μm. Technical data of these elements are given in Table 6.1. Two KUKA robots are used to manipulate the X-ray source and detector. Robots are chosen so as to be compatible with these CT elements weight and to ensure good performances in terms of stability and repeatability. Their main characteristics are given in Table 6.2.

Figure 6.1 displays the complete system installed at CEA LIST with both robots equipped with X-ray source and detector. The system is used in a so called Master /

TABLE 6.1: X-ray source and detector characteristics.

X-ray source XT9225 -TED		**Flat panel detector XRD0822**	
High voltage range	10 225 kV	Pixels	1024 x 1024
Target material	Tungsten	Pixel size	200 μm
Focal spot size	$\leq$ 3 μm	Scintillator	CsI
Weight	35.5 kg	Weight	3.7 kg

TABLE 6.2: Robots characteristics.

Robots KUKA KR60HA	
Maximum payload	60 kg
Maximum range	2258 mm
Repeatability	< 0.05 mm

Slave configuration, where both robots are first moved independently to a desired relative position and are then coupled. After this coupling, trajectory points are sent to the Master robot only and the Slave robot moves automatically to keep the same relative position with respect to the Master robot. In our case, we chose the robot equipped with the source as the Master and we implemented a step-and-shoot acquisition strategy. Therefore, for each point of the trajectory, robots motion is stopped during image acquisition. The automatic control of these robots guarantee the shortest and safest path when moving from one programmed position to another.

CSR robotics software is used to validate the accessibility of the trajectory and to determine the maximum angular range we can expect. When a new trajectory is loaded, its accessibility by each robot is tested and a feedback is given to the user by colouring reachable points in green and non-reachable ones in red as illustrated in Fig. 6.2. Evaluation performed with the installed setup allows a maximum angular range of about

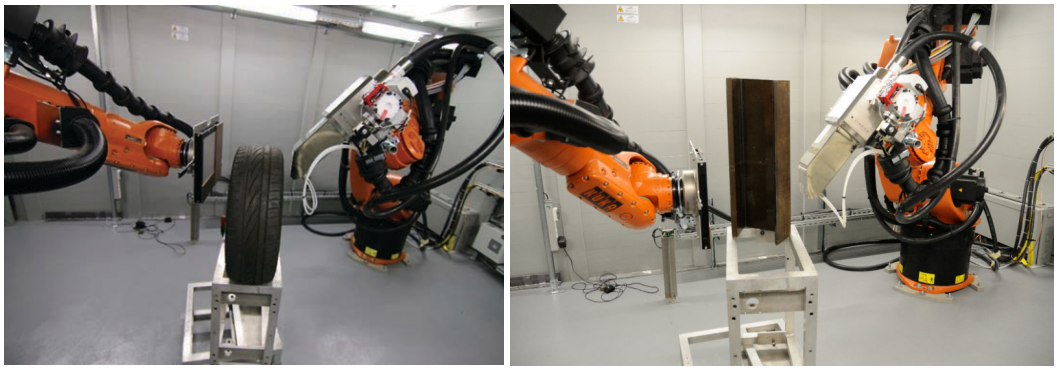

FIGURE 6.1: Robotic CT system installed at CEA LIST.

150°.

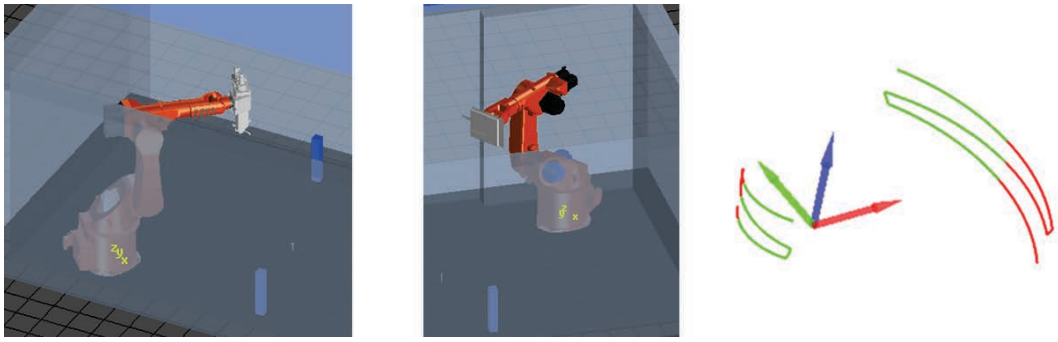

FIGURE 6.2: Model of the source robot (left) and the detector robot (center) in CSR software and an example of the visualization of the accessible trajectory (right).

6.2 Reconstruction Results

When dealing with experimental data, a pre-processing step of the sinogram is essential before the reconstruction. First, a normalization procedure known as flat field correction (FFC) is applied on the measured projections. This normalization is based on flat and dark field images which are acquired in the absence of the inspected object. Flat fields are also known as gain fields and are measured by the detector with X-ray beam turned on. Dark fields or offset fields are obtained without X-ray illumination and with the same exposure time as the one required for the inspection of the object. We use here a conventional FFC method and the normalized projection images I_n are computed as follow

$$I_n = \frac{(I - I_{offset})}{(I_{gain} - I_{offset})}, \tag{6.1}$$

with I are the measured projections in the presence of the object, I_{offset} are the offset fields and I_{gain} refer to the gain fields.

Once the projections are normalized using the FFC method, the negative logarithm of the result is taken in order to extract the line integral values. Here, the two terms $(I - I_{offset})$ and $(I_{gain} - I_{offset})$ may produce zeros or negative values and this will affect the logarithm operator by creating NaN values in the sinogram. This problem is corrected using the "Remove NaNs" function of ImageJ and that replaces NaN values with the neighborhood median value.

In addition, the reconstruction algorithm considers that the rotation axis is located along the center of the sinogram. However, this assumption is difficult to accomplish in real acquisitions where the axis of rotation is almost shifted from the center of the object. To solve this problem, the sinogram is shifted horizontally by the difference

between the object center and the position of the axis of rotation. We estimate this difference based on subtracting a 2D projection acquired at an angle α from another 2D projection acquired at an angle $(\alpha + \pi)$.

Furthermore, the rotation axis is not ideally vertical and might be slightly tilted; hence, the inclination of the rotation axis has to be corrected also. Here, we select a 2D projection and then we locate the midpoint of raw data in the first and last rows. The inclination angle β between the vertical axis and the line joining these two defined midpoints is measured. Then, the sinogram is rotated by this angle β. Finally, there are some defective detector elements or dead pixels and which appear as lines in the sinogram. To remove these lines, we apply a median filter on the regions where the lines are located.

Let's now show some reconstruction results obtained from real experimental data acquired using the robotic platform. These results are divided into three parts. First, we start by showing results from a complete helical scanning trajectory. Then, helical scanning of a large object extending outside the detector FOV is performed and reconstruction results from truncated projection data are illustrated. Finally, reconstructions from incomplete trajectories limited to $150°$ are represented.

6.2.1 Reconstruction on a Helical Scanning Trajectory

The sample object used for inspection is an additive manufactured vase made of titanium alloy and provided by the nuclear energy division (DEN) of CEA. The diameter and height of this vase are 10 cm and 15 cm, respectively. As we can see in Fig. 6.3a, the vase contains a visible defect which is illustrated in the red region. There is also another small hidden defect located inside the vase and that we aim to detect by 3D reconstruction of the volume object.

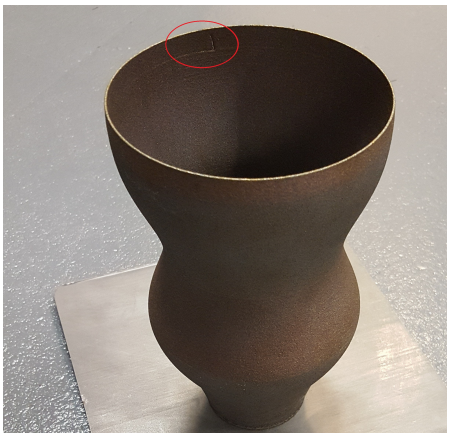

(A) Object

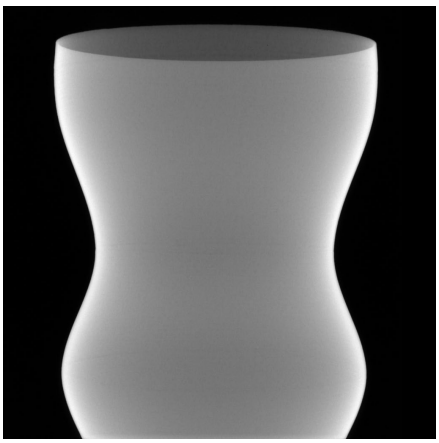

(B) 2D projection

FIGURE 6.3: An additive manufactured vase.

Data acquisition on a complete helical trajectory can not be achieved using the robotic platform only due to limitation of the scanning angle range of each robot. To accomplish scanning on this trajectory, the object is placed on a turntable and during the rotation of the object on this turntable, the two robots move vertically along the direction of the axis of rotation. A synchronization between the rotation of the object and the translational movement of the robots is performed. During data acquisition, X-ray tube voltage is set to 150kV, tube current is 40 μA and a thin Al sheet of 1.5 mm thickness was placed to remove the low energy photons.

The geometrical parameters of this helical scanning are specified in Table 6.3 and an acquired 2D projection is shown in Fig. 6.3b. The number of projections per helical turn is 360 with 4.5 turns to obtain in total 1620 projections. The time between every two consecutive measured projections is 2 seconds where first the rotation of the turntable takes 0.5 seconds, then the two robots need 0.5 seconds for its stabilization and finally the time of acquiring the projection image is 1 second. The total duration of this acquisition is 54 minutes.

TABLE 6.3: Parameters of performed helical scanning.

Distance source-object (Dso)	40 cm
Distance source-detector (Dsd)	60 cm
Helical pitch	6.48 cm

The standard helical FDK algorithm is the algorithm chosen for 3D reconstruction. Thus, some conditions have to be satisfied when defining the parameters of data acquisition. First, the number of projections per helical turn is set to 360 which is sufficient to avoid streak artifacts as we have seen in the numerical results illustrated in Chapter 4. The distances source-object and source-detector are chosen so that the object is included in the FOV and projection data are not truncated transversely. In addition, when reconstructing each voxel in the object, the back-projection step of the helical FDK algorithm is performed along a helical turn corresponding to the axial position of this voxel. Based on this fact, two conditions are required in order to assure that no projection data are missing or truncated axially. Firstly, the value of the pitch (axial translation per helical turn) is adjusted to respect the condition that the detector height is larger than $\left(\frac{Dsd}{Dso} \cdot pitch\right)$. Secondly, the lower and upper endpoints of the helix have to be located at a distance of $\left(\frac{pitch}{2}\right)$ below and above the object, respectively.

The ramp filter of the FDK algorithm is apodized with a Hamming window in order to reduce noise and the reconstruction results are presented in Fig. 6.4 which shows a horizontal slice, vertical slice and 3D view of the reconstructed volume of $512\times512\times512$ voxels. It is clear that the inspected vase is reconstructed well. A zoom-in on the 3D view of the reconstructed volume is shown in Fig. 6.5 and it can be seen that two

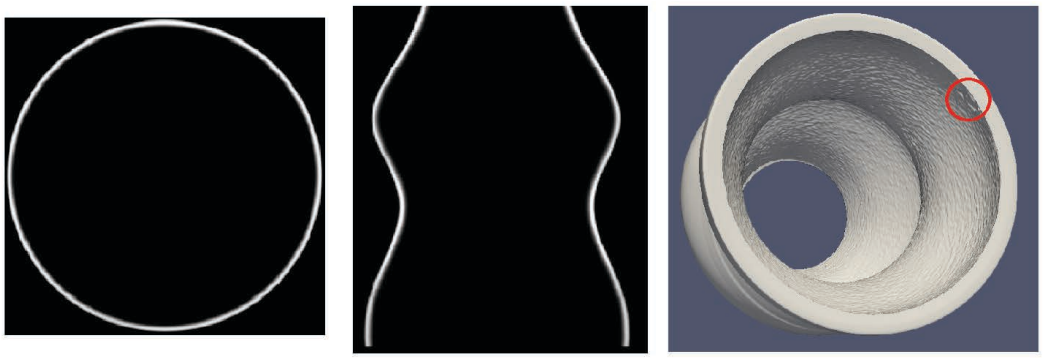

FIGURE 6.4: Horizontal slice (left), vertical slice (center) and 3D view (right) of the vase volume reconstructed using the helical FDK algorithm.

defects are well detected and bounded by the rectangular red regions. The open source software Paraview is used for 3D visualization.

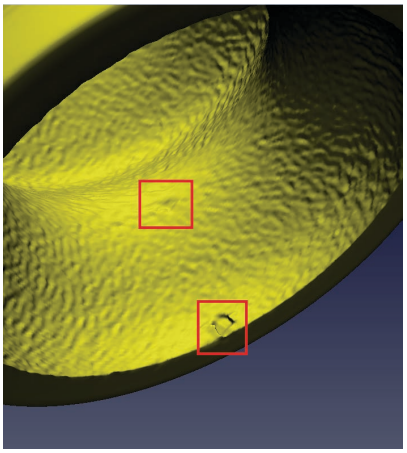

FIGURE 6.5: A zoom-in on the 3D view of the reconstructed volume.

6.2.2 Reconstruction from Truncated data

An aluminium-alloy engine cylinder head of 40 cm in height and 25 cm in width is inspected. This object is large and its projections are supposed to be truncated. We aim to reconstruct a ROI of 17 cm in height and 9 cm in width and that corresponds to the rectangular yellow region shown in Fig. 6.6a. The helical scanning trajectory is used again and the geometrical parameters are identical to those given in the previous subsection. We can see here the advantages of this trajectory when inspecting long objects where we only perform two helical turns around the ROI and which is sufficient to avoid axial truncations. On the other hand, the projections still suffer from transverse truncations and to deal with this aspect FDK$^{(1)}$ algorithm proposed in Chapter 4 is used

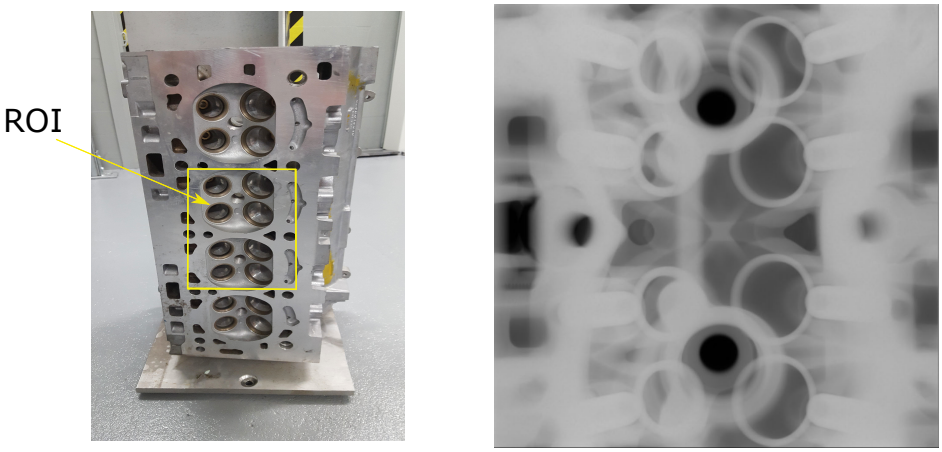

(A) Object (B) 2D projection

FIGURE 6.6: An engine cylinder head.

for reconstruction. Due to analytical nature of this algorithm the number of projections per turn is fixed to 360 projections. The total number of projections is 720 and the duration of data acquisition is 24 minutes. This experiment is carried out at an X-ray tube voltage of 180 kV and tube current of 60 μA and a 2D projection image is illustrated in Fig. 6.6b.

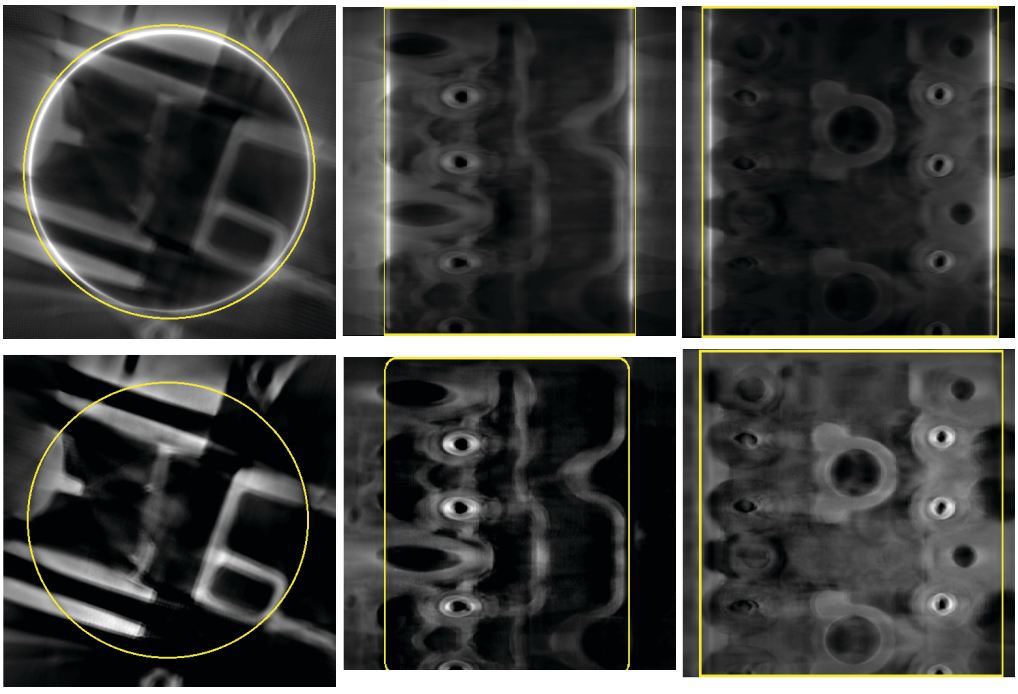

FIGURE 6.7: Reconstruction of an engine cylinder head using the standard helical FDK algorithm (first row) and FDK$^{(1)}$ (second row).

We aim to show the advantages of FDK$^{(1)}$ when data are truncated transversely;

hence, the reconstruction results of this algorithm are shown together in Fig. 6.7 with that of the standard helical FDK algorithm. The first row refers to FDK reconstruction and here the ramp kernel is apodized again with a Hamming window in order to reduce noise artifacts. FDK$^{(1)}$ reconstruction is illustrated in the second row and in this case noise is reduced by smoothing the projections using a Gaussian filter. The first column corresponds to a horizontal slice in the reconstructed volume whereas the second and third columns refer to two orthogonal vertical slices in the reconstructed volume of $512 \times 512 \times 512$ voxels. There are some artifacts in both reconstructions which are linked to geometrical misalignment of the system where the real trajectory performed during acquisition cannot be as precise as the input trajectory. However, it can be seen that structure details in each slice of the volume reconstructed by FDK$^{(1)}$ are visualized better than those of the standard FDK algorithm. Furthermore, the standard FDK algorithm shows cup-artifacts at the boundaries of the ROI shown in yellow whereas these artifacts are not obtained with FDK$^{(1)}$.

6.2.3 Reconstruction from Limited-Angle Data

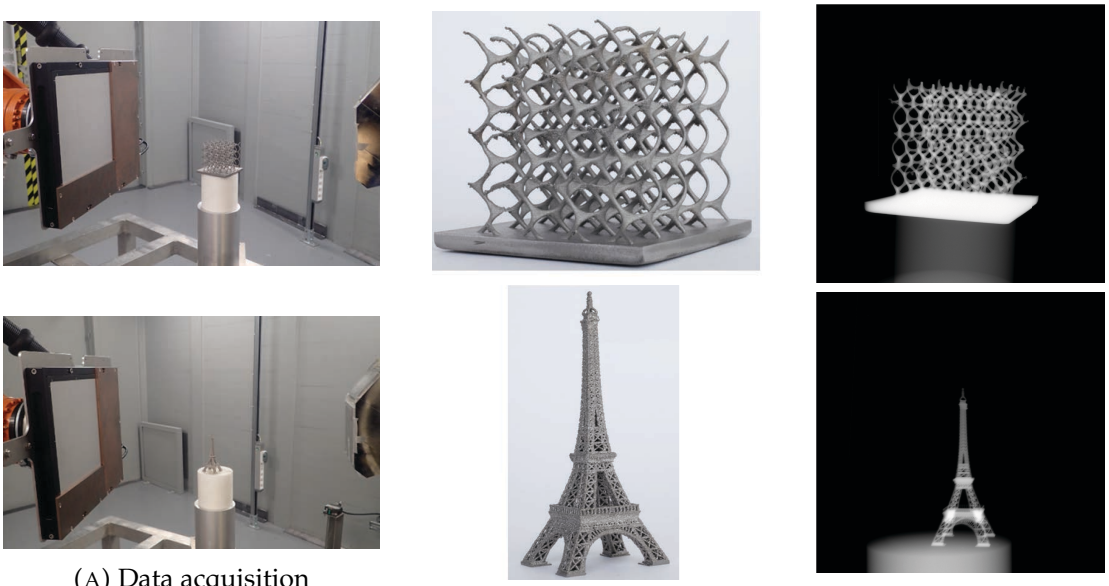

(A) Data acquisition (B) Object (C) 2D projection

FIGURE 6.8: Experimental acquisition of two additive manufactured components.

Experimental studies on incomplete trajectories limited to $150°$ are performed also. Two additive manufactured components supplied by the DEN are used for inspection. Knowing that these two objects are of small dimensions (less than $10 \times 10 \times 10\,\text{cm}^3$), a circular trajectory is sufficient for data acquisition. Thus, the scan is carried out on a

circular trajectory and 150 projections are acquired over an angular range of $150°$. The distances source-object and source-detector are 20 cm and 60 cm, respectively. During this inspection the two robots only move and the object is held fixed. An X-ray tube voltage of 150 kV and tube current of 500 μA are used. Knowing that the turntable is not used here, the time between two consecutive acquisitions is 1.5 seconds and the total duration of data acquisition is 3.75 minutes. These experimental acquisitions are shown in Fig. 6.8 where a 2D projection of each component is illustrated and it can be observed that data truncation does not occur here.

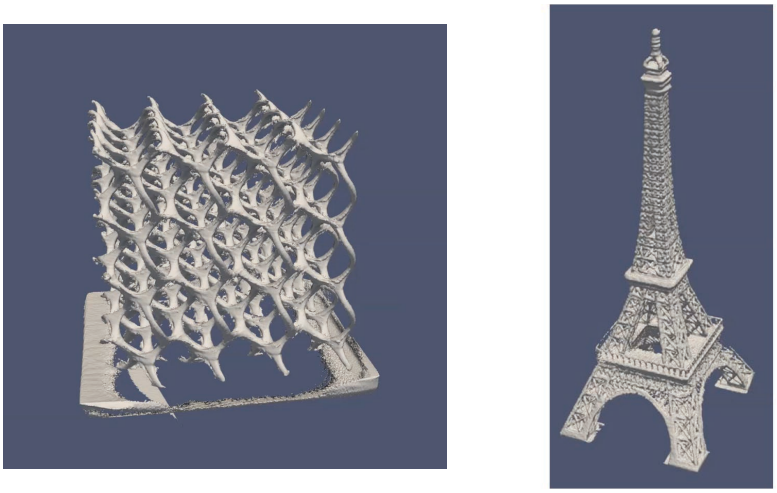

FIGURE 6.9: Reconstruction of two additive manufactured components using SART-FISTA-TV.

Under such condition of very small angle, the tomography reconstruction problem is ill-posed due to missing data and iterative algorithms perform much better than analytic ones as we have seen in Chapter 5 that showed numerical reconstruction results of different algorithms on limited-angle trajectories. Thus, SART-FISTA-TV is chosen here knowing that DART-FISTA-TV is not adapted yet for reconstruction from real experimental data. Paraview software is used for a 3D volume rendering of the reconstructed additive manufactured lattice and Eiffel tower of $500 \times 500 \times 400$ voxels and $300 \times 300 \times 600$ voxels, respectively. It can be seen in Fig. 6.9 that these two objects are reconstructed correctly despite the angular limitation on the scanning trajectory. However, the base of the lattice structure is not reconstructed well because of the greater amount of material the beam has to penetrate. Most of the photons traversing the base are absorbed with these experimental parameters which were chosen in order to reconstruct the upper part of the lattice.

6.3 Conclusions

We validated the performance of the robotic platform by showing reconstruction results from real experimental data. During reconstruction, we did not use all the algorithms proposed in this thesis. However, for each inspection the most suitable algorithm is selected depending on some factors like reconstruction time and nature of missing data. In particular, the standard helical FDK algorithm was used for reconstruction during the first helical inspection due to its high speed and low memory demands knowing that the acquired data were complete and a sufficient number of projections was available. In the second helical scanning, projection data were truncated and here FDK$^{(1)}$ algorithm was used. The reconstruction results were better than that of the standard helical FDK algorithm which produced cup artifacts in this case. Finally, inspections on trajectories limited to 150° were presented. Here, analytical algorithms are not capable of giving satisfying results because of the severe limitation on the scanning angle range. Thus, SART-FISTA-TV algorithm was selected and the reconstruction results were good. It should be mentioned here that a circular trajectory was used because the scanned objects were of small dimensions. Although, this trajectory is a classical one, the main objective of reconstruction from limited-angle data was accomplished and this algorithm is of iterative nature and thus it is flexible and supposed to give the same results when applying it to more complex scanning trajectories with this angular range limitation.

The other implemented algorithms which were not illustrated in these experimental validations are: the exact FBP and BPF algorithms, the FDK-type algorithm adapted to reverse helical limited-angle trajectory and DART-FISTA-TV. First, it was shown that the BPF algorithm needs a large number of projections due to a required rebinning step and thus it is not interesting to our application where more projections have to be acquired and the inspection time will be longer. Concerning the exact FBP algorithm, we performed reconstruction on the helical scanning trajectory by the use of this algorithm and the results obtained were identical to that of FDK and consequently were not mentioned in the previous section. The FDK-type algorithm proposed in the previous chapter was not used for reconstruction on the inspection performed on the incomplete trajectory because this algorithm is limited to the half-scan geometry when we aim to reconstruct the whole object. Finally, DART-FISTA-TV was not adapted to experimental data as we have mentioned in the previous chapter, but we believe that the use of this algorithm with the robotic platform is one of the major perspectives.

In conclusion, these primary reconstruction results obtained from real data acquired with the robotic platform were encouraging. Although the reconstructed images were of good quality, there are some artifacts and thus further improvements are desirable as

developing a geometrical calibration method of the CT system and proposing a correction method for undesired physical phenomena like scattering and beam-hardening.

Chapter 7

Conclusions and Perspectives

7.1 Conclusions

In this thesis, we have studied reconstruction algorithms for non-standard trajectories and that could be applicable to a robotic X-ray inspection platform. This study aimed to review existing analytical and iterative approaches and then to modify the adequate ones and to adapt them to our CT application. In particular, we can divide our work into three parts: i) studying analytical algorithms, ii) studying iterative algorithms and iii) demonstrating reconstruction results from primary experimental data acquired with the robotic platform. The study of each algorithm included theoretical analysis first and then its validation and evaluating its performance using CIVA simulated data. In these numerical evaluations, we were interested in two main aspects that may occur during data acquisition and that could be imposed by this robotic platform: i) truncated data and ii) limited-angle data. First, the two robotic arms cannot perform a complete rotation around the object due to some mechanical constraints and the rotation angle is limited to 150°. This difficulty is very challenging for the reconstruction algorithms. Second, when inspecting large industrial objects, a FOV is only viewed by the detector and consequently the acquired projections are truncated.

In the first part, we studied analytical approaches of image reconstruction. Our study considered exact helical reconstruction algorithms. Among them we chose and implemented two algorithms of type FBP and BPF and which were initially developed by Zou and Pan [149, 150]. Here, we proposed an optimized approach for the implementation of the FBP algorithm [150]. We showed by numerical simulations the advantages of our proposed implementation that avoids a rebinning process and can consequently denote better image quality compared to the original implementation developed by Zou and Pan.

The main drawback of these exact algorithms is that they are not flexible and can not be adapted to limited-angle trajectories. Hence, we were more interested in the well-known approximate FDK algorithm which can be easily adapted to the super-short scan geometry by using a weighting function to handle data redundancy. First, we

worked on modifying this algorithm to deal with transversely truncated data, where we replaced the ramp filtering step of the algorithm by two different approaches. We illustrated the advantages of these two approaches mathematically and then numerically using simulated truncated projection data. Then, one of these algorithms was adapted to the reverse helical trajectory based on a method derived in the context of extended-volume C-arm CT [140]. Therefore, this proposed analytical algorithm was capable to handle the two major aspects discussed in the thesis: limited-angle data and transversely truncated data. Concerning limited-angle data, the performance of the algorithm is limited to a certain degree depending on the scanning angle range. This is due to the analytical nature of the algorithm and which is known to be more affected by missing data compared to its iterative counterpart. Specifically, these limitations of the algorithm were viewed when the scanning angle was less than the short-scan range. In this case, it was not possible to reconstruct the whole object and only a region in the object was reconstructed correctly. However, knowing that the scanning angle that could be obtained by the robotic platform is limited to 150° which is relatively small and less than the short-scan range, this algorithm was not the best choice for our CT application and studying iterative algorithms was essential to solve this problem.

In the second part, we studied iterative reconstruction algorithms. The main advantage of these algorithms is their flexibility where they can be applied to arbitrary trajectories and this is important for the use of our robotic platform to process non-conventional scans. On the other hand, these type of algorithms are time consuming and computationally demanding compared to the FDK-type algorithm. We considered algebraic methods and we worked on integrating regularization techniques where we used the well-known TV minimization to deal with limited-angle data problem. In addition, FISTA technique was integrated to accelerate the convergence speed of the proposed algorithms.

One of our proposed iterative methods named SART-FISTA-TV was tested with a reverse helical trajectory of angular range limited to 150°. This algorithm recovered the overall structure of the multi-disk phantom whose reconstruction was not possible with the presented FDK-type algorithm within such configuration. Another interesting point of this algorithm is that it works well with very few number of projections in contrast to the FDK-type algorithm that causes streak artifacts in this case. Furthermore, this algorithm is efficient in noise suppression. The main drawback of this algorithm is that it can not deal with truncated data.

To further improve the accuracy of reconstruction from these incomplete scanning trajectories, we studied another algebraic algorithm named DART [7] which can incorporate prior knowledge about the different materials of the scanned object into the reconstruction process. The algorithm can be applied if the object consists of five or less different materials and this is feasible in NDT applications where in general the

inspected object is composed of few materials only like aluminum, steel, plastic, etc... Our contribution here was improving the performance of this algorithm by combining it with TV minimization technique. This algorithm was tested with a reverse helix of angular range limited to $150°$ and from very few projections that were corrupted with noise. The obtained results were accurate and it was illustrated that the proposed DART-FISTA-TV algorithm showed a significant impact on image quality with an efficient reduction of noise and better performance than the original DART algorithm. It was shown also that this algorithm can deal with truncated data. However, in experimental acquisitions, the source is polychromatic and we can not know exactly the attenuation coefficient of each material because of its dependence on X-ray beam energy. For this reason, it was not possible to apply the current DART-FISTA-TV algorithm on experimental data. To solve this problem, methods for automatic estimation of the attenuation coefficients could be integrated and this will be discussed in the perspectives.

In the third part, we conducted real experimental inspections using the platform. Three categories of inspections were performed. The first category considered the complete helical scanning trajectory. For this trajectory and to avoid the limitation of the scanning angle range imposed by the two robots, the object was placed onto a rotating turntable and only axial translation of the two robots was performed. The FDK algorithm was used for reconstruction from this complete helical scanning trajectory. Secondly, we presented an inspection of a large object whose acquired projections were truncated transversely. Here, FDK$^{(1)}$ algorithm was used to obtain the 3D reconstructed volume of the corresponding FOV viewed by the detector. Finally, inspections on limited-angle trajectories were realized. In this case, the two robots were used only and the scanning trajectory was circular with an angular range limited to $150°$. Here, the projection data were not truncated and SART-FISTA-TV was used for reconstruction. In general, the reconstruction results obtained with all these performed acquisitions were satisfying and the inspected objects were reconstructed correctly despite of severe missing data in some situations. These encouraging primary experimental results strongly demonstrate the feasibility of robotic inspection for NDT.

Concerning software development, this thesis contributed to integrating new reconstruction plugins in CIVA CT tool whose existing reconstruction algorithms were limited to the circular scanning trajectory. In particular, our developed reconstruction plugins can deal with more complex trajectories including truncation of projection data and limited angular range. The helical-like scanning trajectory was considered for analytical reconstruction where the FDK-type algorithm was integrated and is available in the current version of CIVA. For the iterative part, SART-FISTA-TV was integrated also and can deal with any scanning trajectory. The other implementations like DART-FISTA-TV and the exact FBP algorithm will be integrated in the near future. These reconstruction tools are essential for our robotic CT system. Once data acquisition is

performed, experimental data are imported into CIVA and then 3D reconstruction of the object can be performed using the available plugins.

To summarize, this thesis addressed a significant number of aspects related to reconstruction algorithms adapted to non-standard trajectories for the use with a robotic X-ray inspection platform. Table 7.1 gives a complete list of the proposed algorithms with the scanning trajectory for which it is adapted. More specifically, this thesis presented analytical algorithms for helical-like scanning trajectories, iterative algorithms for arbitrary scanning trajectories and real data demonstration with the robotic platform. We are convinced that these contributions are an important step forward for X-ray robotic inspections in the industrial field.

TABLE 7.1: Reconstruction algorithms proposed in this thesis.

Reconstruction algorithm	**Scanning trajectory**
$FDK^{(1)}$, $FDK^{(2)}$	Standard helix
FDK-type algorithm	Reverse helix with limited angular range
SART-FISTA-TV, DART-FISTA-TV	Arbitrary

7.2 Perspectives

As it was shown in the session "Robotics Assisted NDE" organised at the 19th World Conference on Non-Destructive Testing (WCNDT), at which our presentation was selected as Keynote, the use of robots is an actual trend in CT because it provides more flexibility in the scanning trajectory and allows the inspection of more complex objects. This thesis studied and developed reconstruction algorithms for the use with a robotic X-ray inspection platform. The proposed algorithms were validated on real data obtained by this platform. However, further improvements could be done in the future. We give here an outlook about possible suggestions and ideas for the continuation of this work.

Although the proposed analytical and iterative algorithms were validated with both simulated and real data, two improvements could be achieved from an implementation point of view. First, only CPU implementations of the analytical algorithms were developed due to its low computational cost compared to its iterative alternatives. However, we can highly accelerate these algorithms by developing GPU implementations of the back-projection step only knowing that this step is the most computationally intensive operation in analytical approaches. Second, the iterative algorithms were accelerated with GPU implementations, but there were some limitations on the resolution of the reconstructed volume and on the number of projections that can be used by

these algorithms because of its high memory demands. Thus, a memory management of these algorithms is of great interest.

The performed numerical comparisons showed that DART-FISTA-TV can give accurate reconstructions even with different missing data configurations. Thus, it is very interesting to modify DART-FISTA-TV in order to deal with experimental data. An estimation method that can automatically determine the grey level corresponding to each material is important. In this context, some methods [110, 148] were already proposed and could be integrated in our algorithm.

A prominent feature of industrial CT is that sometimes a CAD model of the inspected object is available. This additional information may be beneficial in obtaining more accurate reconstruction and accelerating the inspection process by reducing the number of projections. In particular, this prior knowledge about the object could be either integrated directly into the reconstruction process of the iterative algorithms by restricting reconstruction to regions where material is present or it could be used to optimize the scanning trajectory and to adapt it to the object by determining the most valuable acquisition poses [37]. We suppose here more complex trajectories using all degrees of freedom. Furthermore, it would be interesting to inspect more complex and challenging industrial objects in the future.

Finally, for better reconstructions, it will be valuable to work on the calibration of the CT system in order to ensure the correct positioning of the imagery system and to deal with misalignment errors during data acquisition which introduced some artifacts in the reconstructed images. There are other improvements that might be possible also like developing a correction method for scattering and beam-hardening which are two physical effects that occur usually in CT.

8

Résumé Étendu

8.1 Contexte

Cette thèse aborde des sujets de recherche dans le domaine industriel du contrôle non destructif (CND) par rayons X. Le CND permet de caractériser l'état d'intégrité d'une structure ou d'une pièce sans l'endommager. Parmi les différentes techniques de CND (par exemple ultrasons, courants de Foucault, thermographie, radiographie ...), la tomographie par rayons X ou CT pour "Computed Tomography" est un outil puissant pour caractériser et localiser les défauts internes et pour vérifier la conformité géométrique d'un objet. L'utilisation de la CT s'est largement développée dans de nombreux domaines industriels afin d'inspecter les composants pour la détection des défauts ainsi que pour les applications d'ingénierie inverse. La CT peut être utilisée pour le contrôle des composants soit pendant leur fabrication ou régulièrement tout au long de leur vie, ce qui peut assurer l'intégrité du produit et permet d'optimiser les coûts de production au cours du processus de fabrication.

Dans le contexte des nouveaux enjeux de la CT, une cellule de tomographie X robotisée a été installée au CEA LIST (voir Figure 8.1). La plateforme se compose de deux bras robotiques pour positionner et déplacer la source et le détecteur en vis-à-vis. Avec cette technologie innovante, les trajectoires d'acquisition peuvent être variées et cela permettra d'optimiser l'inspection des objets complexes de grandes dimensions, présentant une anisotropie importante, principalement des pièces et composants industriels utilisés en aéronautique et automobile. Pendant l'inspection, l'objet reste fixe et notre stratégie repose sur l'idée que seuls les deux robots se déplacent ce qui assure un nouveau niveau d'automatisation au cours du processus d'inspection. Les applications d'une telle plateforme avancée incluent la détection de défauts, la mesure dimensionnelle et l'analyse 3D d'objets complexes dans les domaines de l'automobile, l'aéronautique et la fabrication en général.

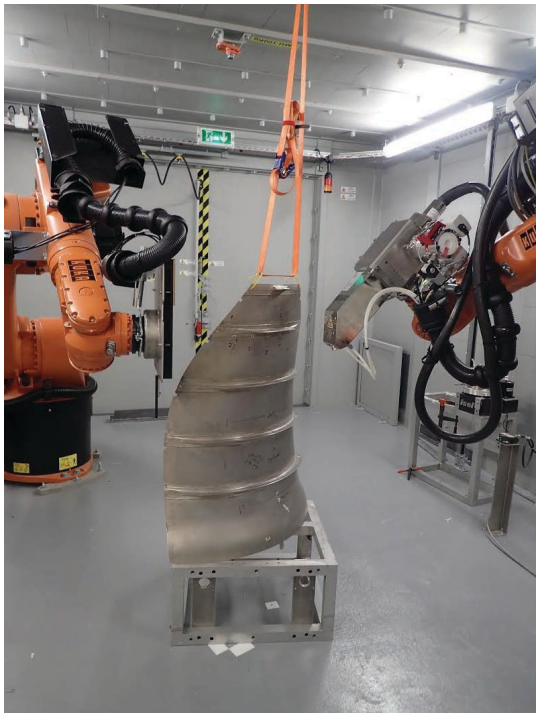

FIGURE 8.1: Cellule de tomographie X robotisée installée au CEA-LIST.

8.2 Objectifs et Défis

Par rapport à des applications médicales, l'objet inspecté en CND peut être très grand et composé de matériaux de haute atténuation auquel cas l'utilisation d'une trajectoire circulaire pour l'inspection est impossible à cause de contraintes dans l'espace. Ainsi, l'utilisation des bras robotisés est l'une des nouvelles tendances reconnues dans la CT car elle permet d'avoir plus de flexibilité dans la trajectoire d'acquisition et permet donc la reconstruction 3D des régions difficilement accessibles qui pourraient être une limitation majeure de systèmes de tomographie industriels classiques. Cette technologie permet une grande variété de trajectoires d'acquisition pour l'inspection de pièces industrielles complexes ou des objets avec des dimensions défavorables à la pénétration des rayons X. Un exemple simple de ces trajectoires d'inspection est la trajectoire hélicoïdale bien connue. Cette trajectoire est considérée comme une solution pour l'inspection des objets longs, qui est la limitation principale de la trajectoire d'acquisition circulaire.

Parmi les nouveaux défis posés par la tomographie robotisée, nous nous concentrons ici plus particulièrement sur la limitation en ouverture angulaire imposée par la configuration en raison des contraintes importantes sur le mouvement mécanique de la plateforme. Le deuxième défi majeur est la troncation des projections qui se produit lorsque l'objet est trop grand par rapport au détecteur.

Un autre défi connu est la localisation de la source et du détecteur pour chaque

point de la trajectoire car l'erreur de positionnement des robots peut introduire des artefacts dans la reconstruction. Ce défi particulier n'est pas traité dans ce travail. Néanmoins, il est possible de réduire l'impact de cette limitation de la tomographie robotisée en choisissant des robots de haute précision et par l'intégration d'une méthode de calibration géométrique.

Avant d'effectuer des inspections robotiques réelles, nous nous appuyons sur des simulations numériques pour évaluer la performance de l'algorithme de reconstruction correspondant à une certaine configuration d'acquisition. Pour ce faire, nous utilisons CIVA qui est un outil de simulation pour le CND développé au CEA et qui peut fournir un modèle réaliste pour les acquisitions radiographiques et capable de simuler les données de projection correspondant à une configuration d'acquisition définie par l'utilisateur. Ainsi, l'objectif principal de cette thèse est de développer des algorithmes de reconstruction adaptés aux trajectoires non-standards et d'intégrer ces algorithmes dans le logiciel CIVA sous forme de plugins de reconstruction.

8.3 Contributions

Dans cette thèse, nous présentons différentes méthodes de reconstruction analytiques et itératives. Pour les algorithmes analytiques, nous considérons seulement les trajectoires hélicoïdales. Au contraire, les algorithmes itératifs que nous proposons sont adaptés aux trajectoires d'acquisition quelconques. Nous nous concentrons principalement dans ce travail sur deux aspects importants qui peuvent se produire lors de l'acquisition de données: i) troncation de données et ii) angle de vue limité. Nous visons également à reconstruire à partir d'un faible nombre de projections afin d'accélérer les cycles d'inspection et augmenter la durée de vie de l'équipement. Les algorithmes que nous proposons sont d'abord testés avec des données simulées par CIVA, puis utilisés pour effectuer des reconstructions à partir de données expérimentales acquises avec la plateforme robotique. Une brève description de ces contributions est donnée ci-aprés:

- **Algorithmes analytiques pour la trajectoire hélicoïdale**

  Nous donnons un aperçu théorique et les détails d'implémentation de trois algorithmes de reconstruction analytique suivant une trajectoire hélicoïdale. Les deux premiers algorithmes sont exacts et ont été développés par Zou et Pan [150, 149] et le troisième est le célèbre algorithme approximatif de Feldkamp, Davis et Kress ou FDK [113]. Nous avons implémenté ces trois algorithmes de manière optimisée par rapport aux formules d'inversion proposées dans la littérature. Une comparaison numérique de ces trois algorithmes en utilisant des données

complètes (sans et avec bruit) et tronquées, simulées avec CIVA, a été présentée lors d'une conférence internationale [2]. De plus, notre implémentation de l'algorithme FDK sur une trajectoire hélicoïdale a été intégrée en tant que plugin de reconstruction dans CIVA CT, et ce travail était une partie d'une communication présentée lors d'une conférence internationale [22].

- **Reconstruction avec des données tronquées**

  Nous proposons deux algorithmes de type FDK pour la reconstruction avec des données tronquées sur une trajectoire hélicoïdale et nous montrons par des simulations numériques (utilisant CIVA) le bon fonctionnement de ces deux algorithmes et leur capacité à corriger les artefacts observés avec l'algorithme standard de FDK dans le cas des données tronquées. Cette contribution a été présentée lors d'une conférence internationale [5].

- **Reconstruction avec un angle de vue limité**

  Nous proposons deux algorithmes pour la reconstruction sur une trajectoire hélicoïdale avec un angle de vue limité. Le premier algorithme est analytique de type FDK et le second est itératif et basé sur un algorithme algébrique (SART). Une comparaison numérique de ces deux algorithmes a été illustrée en utilisant des données simulées par CIVA et qui sont générées sur une trajectoire hélicoïdale avec un angle de vue limité à $150°$. En se basant sur les résultats numériques obtenus, nous donnons quelques éléments de discussion en ce qui concerne les avantages et les inconvénients de chaque algorithme pour la reconstruction avec une telle configuration. Ces résultats ont été inclus dans une publication qui a été présentée lors d'une conférence internationale [4].

- **Algorithmes itératifs**

  Nous présentons une version améliorée d'un algorithme appelé Discrete Algebraic Reconstruction Technique (DART). DART est un algorithme algébrique qui peut incorporer dans le processus de reconstruction des informations a priori sur les différents matériaux (coefficients d'atténuation) de l'objet inspecté. L'algorithme proposé est appelé DART-FISTA-TV et il combine DART avec la variation totale (TV) comme méthode de régularisation. Nous montrons par des comparaisons numériques que l'algorithme DART-FISTA-TV proposé peut améliorer la qualité de l'image reconstruite et fonctionne mieux que l'algorithme original DART. En outre, un algorithme algébrique régularisé nommé SART-FISTA-TV a été intégré dans CIVA comme plugin de reconstruction. Ces résultats ont été présentés lors d'une conférence internationale et seront soumis prochainement [3].

- **Reconstruction à partir des acquisitions expérimentales**

Nous montrons des premiers résultats de reconstruction à partir d'acquisitions expérimentales effectuées avec la plateforme robotique. Plusieurs inspections ont été effectuées puis les volumes ont été reconstruits avec les algorithmes proposés. Ce travail a été présenté lors d'une conférence internationale [6].

Pour résumer, cette thèse est basée sur six papiers de conférence publiés [5, 2, 3, 4, 6, 22] et un article est prêt à être soumis pour publication dans un journal. Voici une liste complète de ces papiers:

- H. Banjak, M. Costin, C. Vienne, V. Kaftandjian, "Two Local FBP Algorithms for Helical Cone-beam Computed Tomography". In: Digital Industrial Radiology and Computed Tomography, 2015.
- H. Banjak, M. Costin, C. Vienne, V. Kaftandjian, "Implementation and Evaluation of Two Helical CT Reconstruction Algorithms in CIVA". In: 42nd Annual Review of Progress in Quantitative Non-Destructive Evaluation. AIP Publishing, Vol. 1706. AIP Publishing, 2016, p. 110001.
- H. Banjak, M. Costin, C. Vienne, R. Guillamet, V. Kaftandjian, "Reconstruction Algorithms for Reverse Helical Super-Short-Scan Mode". In: 4th International Meeting on Image Formation in X-ray Computed Tomography, 2016.
- H. Banjak, M. Costin, C. Vienne, V. Kaftandjian, "X-ray Computed Tomography Reconstruction on Non-Standard Trajectories for Robotized Inspection". In: proceedings of the World Conference of NDT, 2016.
- M. Costin, D. Tisseur, C. Vienne, R. Guillamet, H. Banjak, N. Bhatia, R. Fernandez, "CIVA CT, an advanced simulation platform for NDT". In: 6th Conference on Industrial Computed Tomography, 2016.
- H. Banjak, M. Costin, C. Vienne, R. Guillamet, V. Kaftandjian, "Iterative CT Reconstruction on Limited Angle Trajectories Applied to Robotic Inspection". In: 43nd Annual Review of Progress in Quantitative Non-Destructive Evaluation. AIP Publishing, 2017 (à publier).

8.4 Plan de Manuscrit

Cette thèse est composée de sept chapitres. Après l'introduction présentée dans le premier chapitre, nous présentons une étude bibliographique qui est divisée en deux chapitres (Chapitres 2 et 3) . Une brève description de ces deux chapitres est présentée ci-après:

- Chapitre 2: Nous décrivons les principes de la CT comprenant les bases physiques de l'imagerie par rayons X et les bases mathématiques de reconstruction d'image. D'autres aspects importants sont présentés, comme l'évolution des scanners à rayons X, les trajectoires d'acquisition des données et les problèmes de données manquantes comme la reconstruction à partir d'un faible nombre de projections ou sur un angle de vue limité et le cas des projections tronquées.

- Chapitre 3: Nous étudions les méthodes principales de reconstruction analytique et itérative pour les trajectoires d'acquisition non-standards. Pour la reconstruction analytique, les deux algorithmes de type exacts et approximatifs sont détaillés en mettant l'accent principal sur les trajectoires hélicoïdales d'acquisition. Nous introduisons les notations mathématiques de base, les conventions de géométrie et des formules d'inversion de certains algorithmes de reconstruction. Pour la reconstruction itérative, les méthodes statistiques et algébriques sont examinées. Le processus de reconstruction de certaines méthodes algébriques est également illustré. Ce chapitre se termine par quelques remarques sur les avantages et les inconvénients de chaque approche.

Nos contributions sont présentées dans les trois chapitres suivants (Chapitres 4, 5 et 6). Une description de ces trois chapitres est la suivante:

- Chapitre 4: Ce chapitre est consacré uniquement à des algorithmes analytiques pour la reconstruction sur une trajectoire hélicoïdale. Nous avons implémenté deux algorithmes exacts pour la trajectoire hélicoïdale. Les détails de ces deux implémentations sont donnés et une implémentation optimisée a été proposée. Nous montrons par des simulations numériques les avantages des implémentations proposées et nous comparons les deux algorithmes exacts avec l'algorithme FDK. De plus, nous proposons deux algorithmes de type FDK pour une trajectoire hélicoïdale qui sont bien adaptés au cas des données tronquées. Les données simulées par CIVA sont utilisées pour montrer les avantages de ces deux algorithmes par rapport à l'algorithme standard de FDK lorsque les projections sont tronquées.

- Chapitre 5: Nous présentons dans ce chapitre des contributions pour la reconstruction analytique et itérative. Nous nous concentrons principalement sur l'angle de vue limité pendant l'acquisition. Pour la reconstruction analytique, nous proposons un algorithme de type FDK qui est adapté à la trajectoire hélicoïdale avec un angle de vue limité. Pour la partie itérative, deux algorithmes algébriques régularisés: i) SART-FISTA-TV et ii) DART-FISTA-TV sont proposés pour la reconstruction sur une telle trajectoire incomplète. Nous validons et comparons

les algorithmes proposés et étudions leur performance en utilisant des données numériques générées par CIVA.

- Chapitre 6: Nous présentons des résultats à partir de données réelles obtenues par la plateforme robotique. Ces inspections ont été effectuées sur des trajectoires hélicoïdales et avec des données manquantes comme des projections tronquées ou un angle de vue limité. Nous montrons des reconstructions à partir de données réelles et avec les algorithmes analytiques et itératifs proposés. Ces premiers résultats expérimentaux valident les performances de la plateforme.

Enfin, nous résumons dans le Chapitre 7 le travail de cette thèse et nous discutons certains travaux futurs possibles sur le développement des algorithmes de reconstruction pour la plateforme robotique d'inspection.

8.5 Résultats Obtenus

Les résultats obtenus lors de cette thèse sont résumés dans cette section. D'abord, les avantages de notre implémentation de l'algorithme FBP exact sont montrées. Ensuite, nous présentons deux algorithmes de type FDK pour la reconstruction sur une trajectoire hélicoïdale et qui permet de gérer la troncation des projections. Après, un algorithme de type FDK adapté à la trajectoire hélicoïdale inversée avec un angle d'acquisition limité est illustré. Ensuite, deux algorithmes algébriques régularisés nommés SART-FISTA-TV et DART-FISTA-TV pour la reconstruction sur des trajectoires plus complexes sont présentés. Enfin, la validation de ces algorithmes proposés sur des données réelles obtenues avec la plateforme robotique est montrée.

8.5.1 Algorithme FBP Exact

Les avantages de notre implémentation de l'algorithme FBP exact [150] par rapport à l'implémentation proposée par Zou et Pan sont montrés par des simulations numériques en utilisant le fantôme 3D de Shepp-Logan comme un modèle de référence pour simuler les projections. La Figure 8.2 montre trois coupes orthogonales du fantôme reconstruites avec l'algorithme FBP. La première ligne correspond à des coupes orthogonales originales dans le fantôme où les lignes blanches en pointillé sont utilisées pour une comparaison quantitative. Deux simulations numériques comparent notre implémentation à l'implémentation développée par Zou et Pan. Cette dernière fournit la reconstruction illustrée dans la deuxième ligne où certains artefacts apparaissent dans les régions non-uniformes de chaque coupe. Par contre et comme illustré sur la troisième ligne, notre implémentation semble être plus précise car aucun artefact n'est observé dans les images reconstruites.

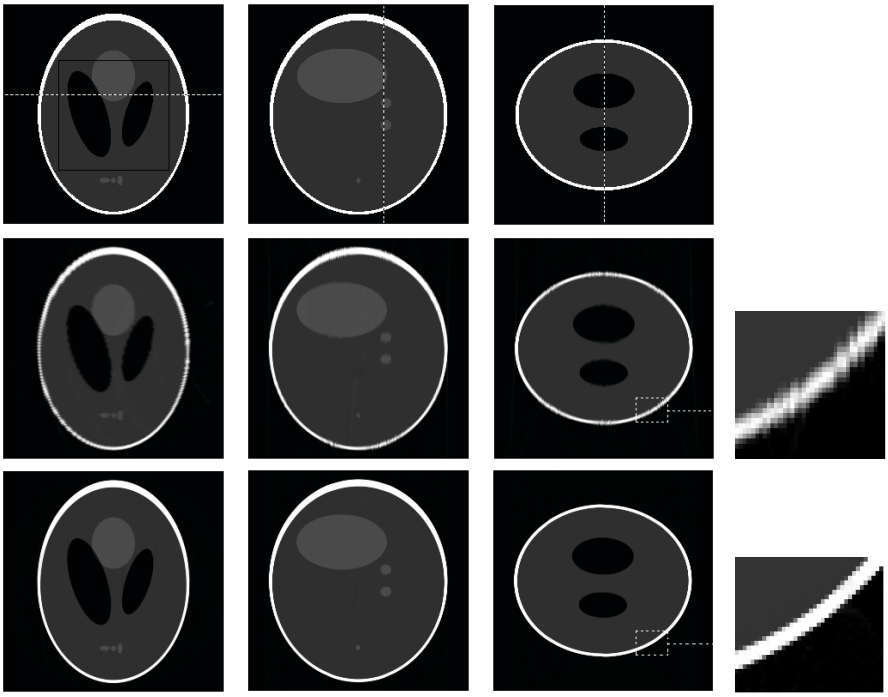

FIGURE 8.2: Reconstruction du fantôme en utilisant deux implémentations différentes de l'algorithme FBP.

Une comparaison quantitative des valeurs originales et reconstruites en utilisant les deux implémentations est illustrée sur la Figure 8.3. Les valeurs originales (ligne continue) et celles reconstruites par le biais de notre implémentation (ligne en pointillée) sont en très bon accord tandis que les valeurs reconstruites avec l'implémentation proposée par Zou et Pan paraissent plus éloignées des valeurs originales.

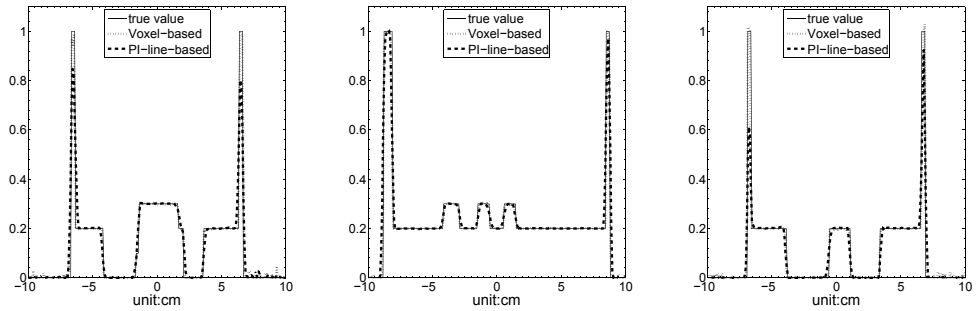

(A) x = -1.45 cm and z = 0. (B) y = 0 and z = 2.5 cm. (C) x = 0 and z = 0.

FIGURE 8.3: Comparaison quantitative selon les lignes blanches en pointillé représentées sur la Figure 8.2

8.5.2 Des Algorithmes de Type FDK pour des Données Tronquées

Deux algorithmes de type FDK ont été proposés pour la reconstruction sur une trajectoire hélicoïdale avec des données tronquées. Ces deux algorithmes utilisent des approches alternatives pour filtrer les projections qui permettent de réduire les artefacts obtenus avec l'algorithme standard de FDK, qui est basé sur le filtre rampe. Le premier algorithme FDK$^{(1)}$ remplace le filtre rampe avec la dérivée première et la transformée de Hilbert et le deuxième algorithme FDK$^{(2)}$ est basé sur l'opérateur de Laplace combiné avec un noyau logarithmique. Les avantages de ces deux algorithmes dans le cas des données tronquées ont été mis en évidence via des simulations numériques. Les paramètres de ces simulations sont indiquées dans le tableau 8.1 où l'objet est un modèle de conception assistée par ordinateur (CAO)similaire au fantôme de Defrise [27] avec des trous circulaires et rectangulaires de différentes tailles (voir Figure 8.4).

TABLE 8.1: Paramètres des simulations numériques.

Rayon de l'objet (r)	7.5 mm
Rayon de l'hélice (R)	30 mm
Distance source-détecteur (D)	60 mm
Pas de l'hélice (2πh)	2.333 mm
Nombre de tours	9
Nombre de projections par tour	360
Taille du pixel du détecteur	0.065×0.065 mm^2
Résolution du détecteur	100×512 pixels
Résolution de l'image reconstruite	$512 \times 512 \times 512$ Voxels

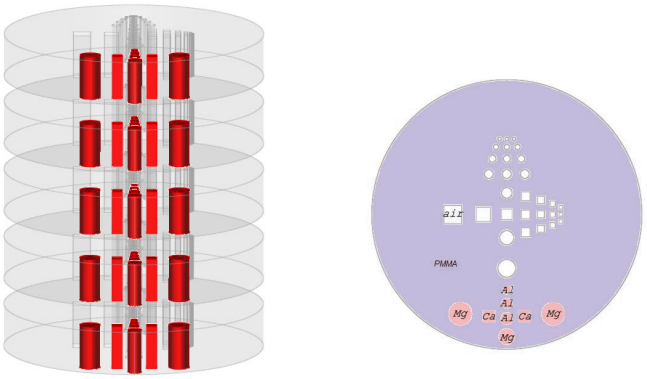

(A) Vue 3D (B) Coupe horizontale

FIGURE 8.4: Illustration du fantôme utilisé dans les simulations.

Dans ces simulations, 128 pixels de chaque côté sur toutes les lignes du détecteur sont mis à zéro. Au sein de cette configuration illustrée sur la Figure 8.5, seulement

la moitié de l'objet est aperçue par le détecteur et le champ de vue en rouge est par conséquent réduit à sa demi-taille.

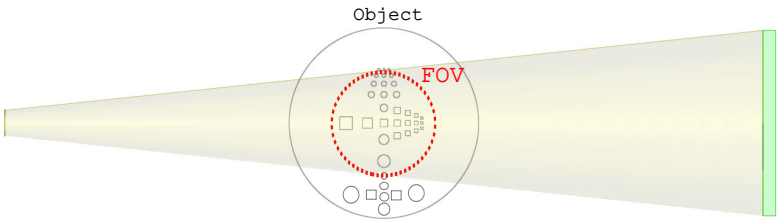

FIGURE 8.5: Illustration du champ de vue correspondant à des données tronquées.

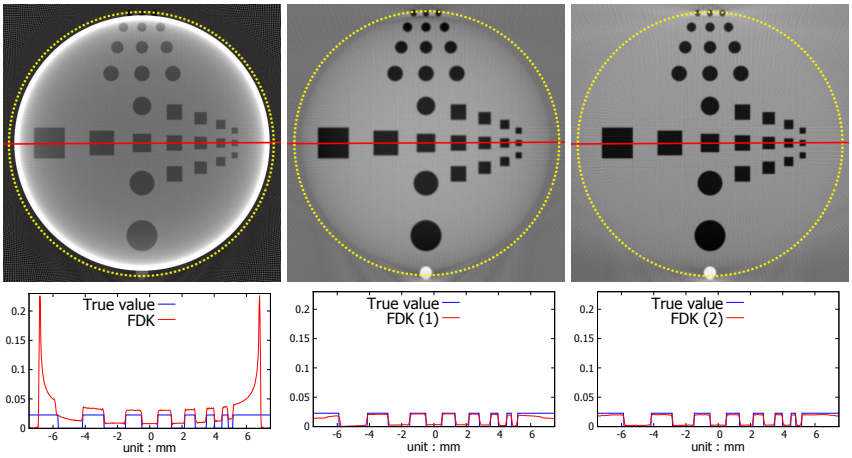

(A) FDK (B) FDK$^{(1)}$ (C) FDK$^{(2)}$

FIGURE 8.6: Reconstruction avec les algorithmes de type FDK à partir des données tronquées sans bruit.

La Figure 8.6 représente les résultats de reconstruction à partir des données tronquées. L'algorithme FDK standard ne peut pas gérer la troncation et des artefacts importants nommés "cup artifacts" apparaissent dans la reconstruction. D'autre part, les deux algorithmes modifiés montrent des reconstructions sans artefacts. La comparaison quantitative sur les lignes rouges montre qu'un offset de reconstruction important est apparu avec l'algorithme FDK standard en cas de données tronquées, alors que cet offset a été supprimé lors de l'utilisation des deux algorithmes FDK modifiés.

La robustesse de ces deux algorithmes proposés a été testée avec des données bruitées. Un bruit gaussien avec un écart type de 0,5 % de la valeur maximale des données sans bruit a été ajouté avant la reconstruction. La Figure 8.7 montre la reconstruction de ces données tronquées et bruitées. Les résultats obtenus montrent que les deux algorithmes FDK modifiés sont robustes au bruit en ayant un comportement similaire. Ce

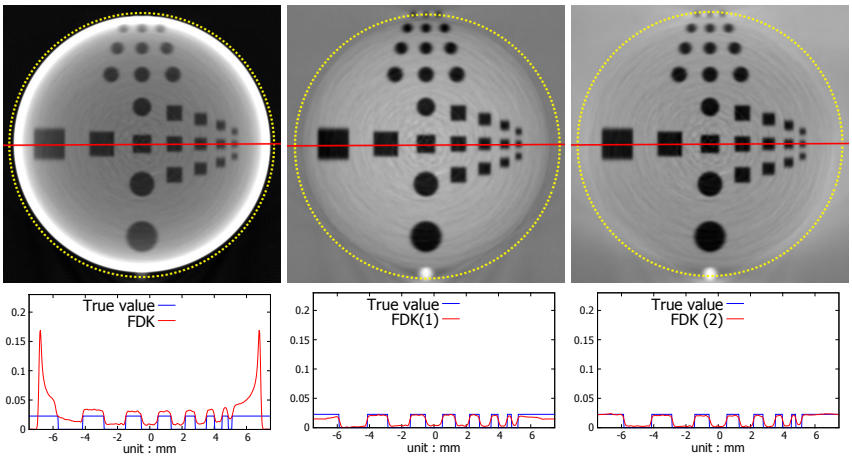

(A) FDK (B) FDK$^{(1)}$ (C) FDK$^{(2)}$

FIGURE 8.7: Reconstruction avec les algorithmes de type FDK à partir des données tronquées et bruitées.

comportement peut être observé soit en comparant la coupe centrale de chaque image reconstruite ou en analysant la comparaison quantitative sur les lignes rouges.

8.5.3 Un Algorithme de Type FDK pour l'Angle de Vue Limité

Récemment, trois algorithmes de type FDK ont été proposés pour la reconstruction sur une trajectoire hélicoïdale inversée [140]. Ces algorithmes sont basés soit sur le filtre rampe soit sur la transformée de Hilbert. A partir de la structure générale de ces algorithmes, nous proposons un algorithme de type FDK pour la reconstruction sur une trajectoire hélicoïdale inversée avec un angle de vue limité. Cet algorithme utilise un filtre basé sur lopérateur de Laplace combiné avec un noyau logarithmique et qui a été représenté dans la sous-section précédente. Ainsi, cet algorithme proposé est adapté à la fois pour des données tronquées et un angle de vue limité.

TABLE 8.2: Paramètres des simulations.

Rayon de l'objet (r)	7.5 mm
Rayon de l'hélice (R)	20 mm
Distance source-détecteur (D)	40 mm
Pas de l'hélice (2πh)	2.05 mm
Nombre de tours	9
Nombre de projections par tour	300
Taille du pixel du détecteur	256×256 pixels
Résolution du détecteur	0.14×0.14 mm^2
Résolution de l'image reconstruite	$512 \times 512 \times 512$ Voxels

L'évaluation de cet algorithme est basée sur des données simulées par CIVA avec les paramètres d'acquisition donnés dans le tableau 8.2. la robustesse de l'algorithme aux données bruitées et tronquées a été testée et deux angles ($240°$ et $150°$) d'acquisition pour la trajectoire hélicoïdale inversée sont considérés.

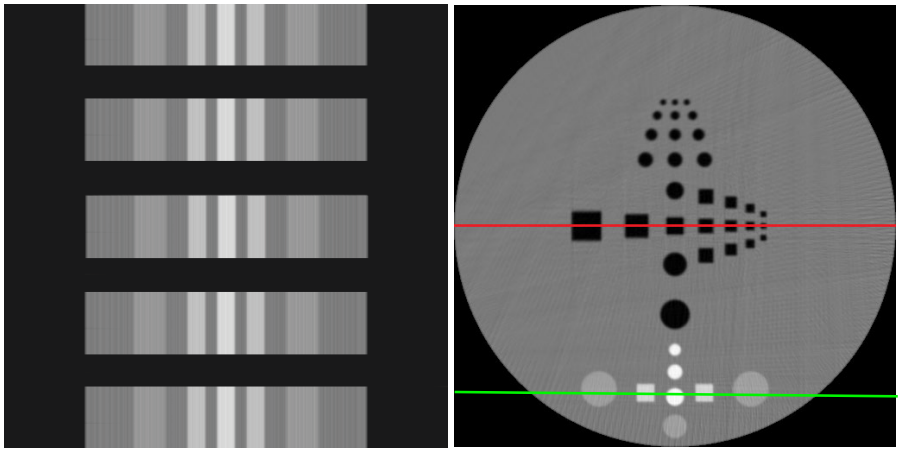

(A) Coupe verticale (B) Coupe horizontale

FIGURE 8.8: Reconstruction avec l'algorithme de type FDK à partir de projections non bruitées générées sur une trajectoire hélicoïdale inversée avec un angle d'acquisition de $240°$.

La Figure 8.8 présente les résultats de reconstruction avec un angle d'acquisition de $240°$ et à partir de projections complètes et non bruitées. Des coupes horizontale et verticale dans le volume reconstruit sont illustrées et les résultats obtenus sont satisfaisants et valident l'algorithme proposé. Une comparaison quantitative sur les lignes rouge et verte est illustrée en Figure 8.9 où il peut être observé que les valeurs reconstruites sont correctes et concordent bien avec les valeurs originales.

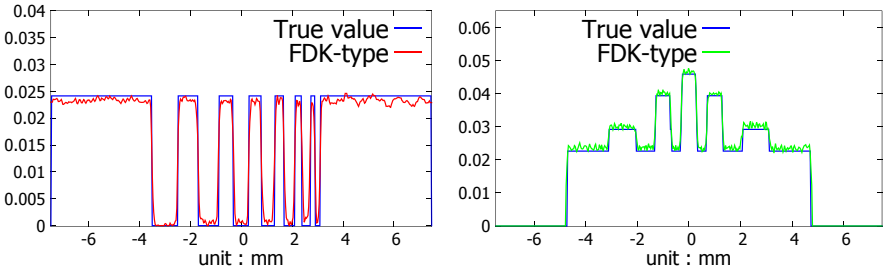

FIGURE 8.9: Une comparaison quantitative sur les lignes rouge et verte en Figure 8.8.

Le comportement de l'algorithme aux données tronquées a été étudié où la configuration de troncation est similaire à celle de la sous-section précédente avec le champ

de vue réduit à sa demi-taille. Les résultats de reconstruction à partir des données tronquées et sans bruit sont présentés sur la Figure 8.10 où le cercle en pointillé jaune correspond à la région d'intérêt vue par le détecteur. Au sein de cette configuration, la trajectoire hélicoïdale inversée de $240°$ a été utilisée. Il peut être observé que l'algorithme développé de type FDK est très efficace et il n'y a pas d'artefacts dans la reconstruction ni en raison des données tronquées ni en raison de l'angle de vue limité. Une comparaison quantitative sur la ligne rouge est tracée et il est clair que les valeurs reconstruites concordent bien avec les valeurs originales.

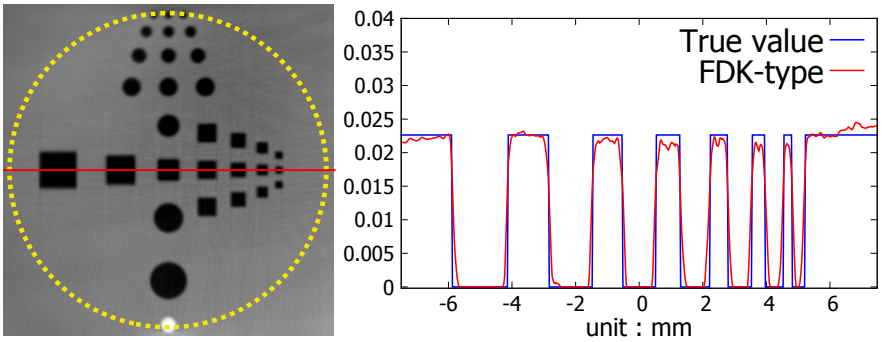

FIGURE 8.10: Reconstruction avec l'algorithme de type FDK à partir de projections tronquées et non bruitées générées sur une trajectoire hélicoïdale inversée avec un angle d'acquisition de $240°$.

Du bruit gaussien a été ajouté aux données tronquées afin de montrer la robustesse de l'algorithme au bruit. L'écart-type de ce bruit gaussien est 0.5 % de la valeur maximale dans les projections sans bruit. Les résultats de reconstruction à partir des données tronquées et bruitées sont présentés sur la Figure 8.11 qui montre une région d'intérêt dans une coupe horizontale du volume reconstruit et une comparaison quantitative sur la ligne rouge. Bien que la qualité d'image soit un peu moins bonne que celle obtenue en l'absence de bruit, ces résultats sont acceptables et l'algorithme est robuste aux données bruitées.

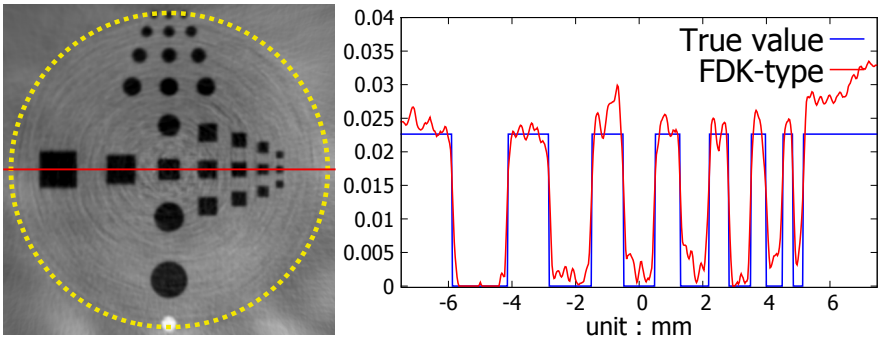

FIGURE 8.11: Reconstruction avec l'algorithme de type FDK à partir de projections tronquées et bruitées générées sur une trajectoire hélicoïdale inversée avec un angle d'acquisition de $240°$.

Dans le but d'étudier la reconstruction à partir d'un faible nombre de projections, le nombre de projections par tour est réduit de 300 à 50 projections et la reconstruction obtenue à partir de ce faible nombre de projections est illustrée en Figure 8.12. Une coupe horizontale et une coupe verticale du volume reconstruit sont représentées et il est clair qu'il y a une dégradation importante en contraste et en résolution dans les images reconstruites et la reconstruction est affectée par des artefacts nommés "streak atifacts". Ce résultat est attendu puisque l'algorithme proposé est de type analytique et l'échantillonnage doit être suffisant afin de respecter le théorème d'échantillonnage de Nyquist-Shannon.

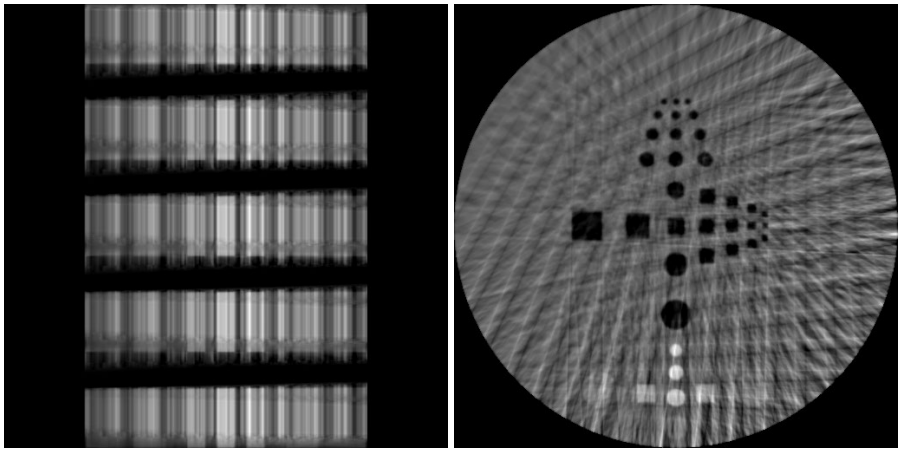

(A) Vertical slice (B) Horizontal slice

FIGURE 8.12: Reconstruction avec l'algorithme de type FDK à partir d'un faible nombre de projections non bruitées et qui sont générées sur une trajectoire hélicoïdale inversée avec un angle d'acquisition de $240°$.

Enfin, le but est d'étudier la performance de l'algorithme lorsque l'angle d'acquisition est réduit encore plus. Une reconstruction sur une trajectoire hélicoïdale inversée avec un angle d'acquisition de $150°$ est présentée. Les résultats de reconstruction sont illustrés sur la Figure 8.13 où une coupe horizontale et une coupe verticale sont représentées avec une comparaison numérique correspondant à la ligne rouge tracée dans la coupe horizontale. On peut voir que l'algorithme proposé a réussi à reconstruire la région d'intérêt définie par le rectangle jaune en pointillé et les valeurs reconstruites sur la ligne rouge sont très proches des valeurs originales. Cependant, la reconstruction en dehors de cette région n'est pas assez bonne et des artefacts sont visibles. Pour éliminer ces artefacts obtenus à cause des données manquantes et qui est connu pour être la limitation des algorithmes analytiques, deux algorithmes itératifs seront présentés dans la sous-section suivante.

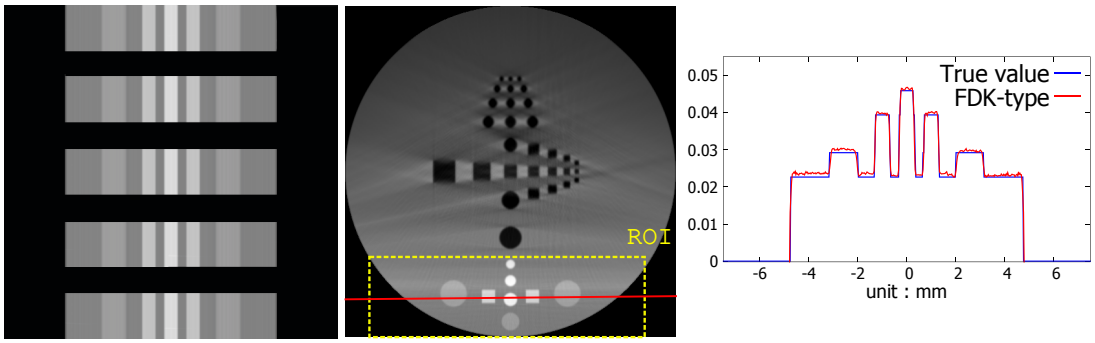

FIGURE 8.13: Reconstruction avec l'algorithme de type FDK à partir de projections complètes non bruitées générées sur une trajectoire hélicoïdale inversée avec un angle d'acquisition de $150°$.

8.5.4 Algorithmes Algébriques Régularisés

Deux méthodes algébriques régularisées qui minimisent la variation totale (TV) de l'image sont présentées dans cette section. TV [95] est un terme de régularisation qui tend à lisser le bruit en préservant les contours de l'image. De plus, les deux algorithmes intègrent un terme nommé Fast Iterative Shrinkage-Thresholding Algorithm (FISTA) afin d'accélérer la convergence. Le premier algorithme appelé SART-FISTA-TV est basé sur SART qui est couramment utilisé pour la reconstruction itérative et le second appelé DART-FIESTA-TV est basé sur DART. Nous montrons ici la robustesse de ces deux méthodes vis à vis des artefacts obtenus précédemment avec l'algorithme de type FDK en cas de faible angle d'acquisition ($150°$). Les paramètres d'acquisition des données sont identiques à ceux qui sont spécifiés dans la sous-section précédente, mais les projections sont réduites de 300 à 10 projections par tour. Les volumes reconstruits sont composés de seulement $256 \times 256 \times 256$ voxels à cause du coût de calcul important et des exigences de mémoire.

SART-FISTA-TV se compose de trois étapes principales: i) SART, ii) minimisation de TV et iii) technique d'accélération de convergence FISTA. Pour montrer les avantages de cet algorithme, les résultats de SART-FISTA-TV sont représentés ensemble avec SART. Une coupe horizontale et une coupe verticale des volumes reconstruits par l'utilisation de SART-FISTA-TV et SART sont illustrées sur la Figure 8.14. La reconstruction par SART-FISTA-TV est satisfaisante, tandis que la reconstruction par SART montre des artefacts importants à cause de l'angle de vue limité. En outre, il y a des artefacts de type streak à cause du faible nombre de projections. Les valeurs de reconstruction sont présentées quantitativement en montrant des profils sur les lignes rouges dans les coupes horizontales. Ces valeurs reconstituées obtenues par l'utilisation de SART-FISTA-TV ne sont pas exactement identiques aux valeurs originales et une petite erreur est obtenue. Par contre, cette erreur peut être acceptée et elle est faible par

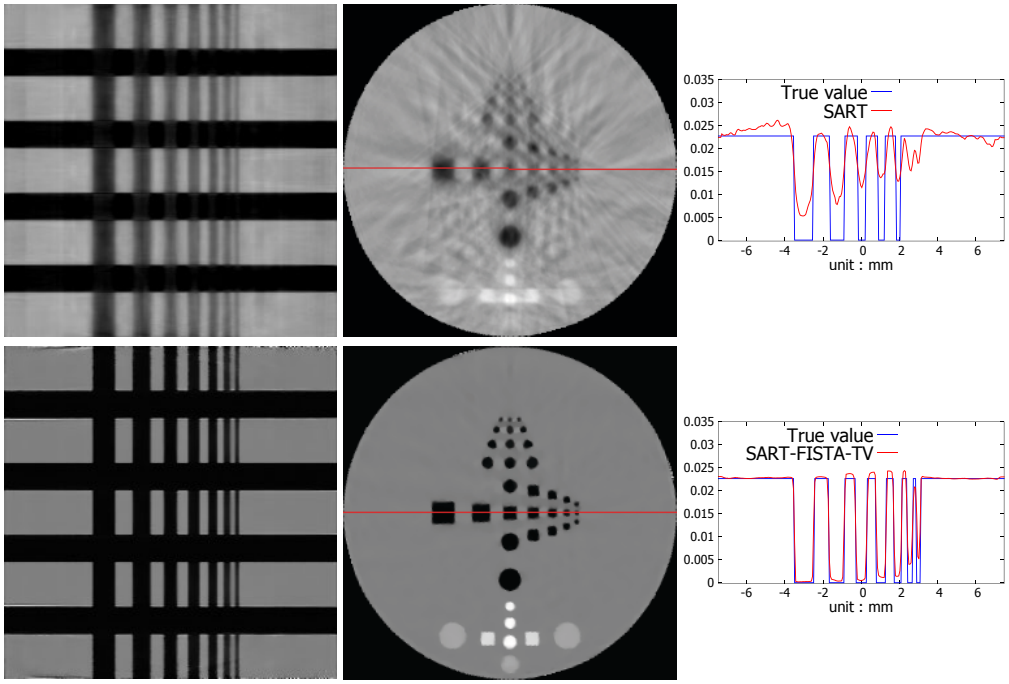

FIGURE 8.14: Reconstruction par SART (avec et sans régularisation) à partir des données non bruitées simulées sur une trajectoire hélicoïdale inversée avec un angle d'acquisition de $150°$. La première et seconde ligne correspondent aux SART et SART-FISTA-TV, respectivement.

rapport à l'erreur obtenue avec l'utilisation de SART.

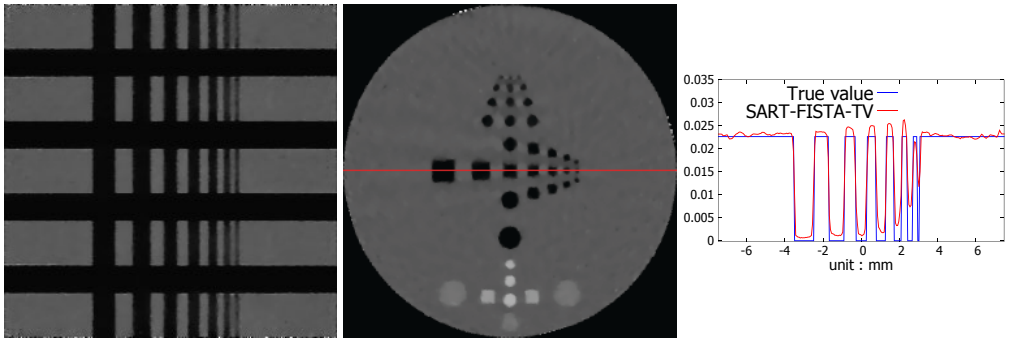

FIGURE 8.15: Reconstruction par SART-FISTA-TV à partir de projections bruitées simulées sur une trajectoire hélicoïdale inversée avec un angle d'acquisition de $240°$.

La robustesse de l'algorithme aux données bruitées a été étudiée par l'ajout d'un bruit gaussien aux projections, où l'écart-type σ de ce bruit gaussien est 0.5 % de la valeur maximale dans les projections non bruitées. La Figure 8.15 montre les résultats de reconstruction de SART-FISTA-TV à partir des données bruitées. Une coupe horizontale et une coupe verticale dans le volume reconstruit sont illustrées avec une

comparaison numérique sur la ligne rouge. On peut voir que la qualité d'image se dégrade légèrement et les valeurs reconstruites deviennent moins précises. Cependant, ces résultats ne sont pas surprenants étant donné qu'il y a seulement 10 projections par tour et il est prévisible que la robustesse de l'algorithme au bruit est meilleure lorsque le nombre de projections augmente.

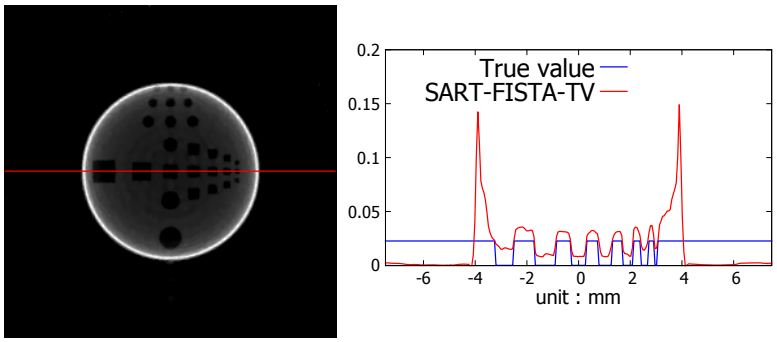

FIGURE 8.16: Reconstruction par SART-FISTA-TV à partir de projections tronquées sans bruit.

Une dernière étude est réalisée pour étudier le comportement de cet algorithme lorsque les données sont tronquées. Dans cette simulation, l'objectif est d'étudier l'impact de la troncation seulement et donc l'angle d'acquisition est 360°. La largeur du détecteur est réduite à sa demi-taille et les résultats de reconstruction sont montrés en Figure 8.16. Il peut être observé que des artefacts importants de type "cup artifacts" apparaissent dans la coupe horizontale illustrée. La comparaison numérique sur la ligne rouge montre un grand offset entre les valeurs originales en bleu et les valeurs reconstruites en rouge. Ainsi, cet algorithme ne fonctionne pas bien lorsque les données sont tronquées.

DART-FISTA-TV est un algorithme qui combine DART avec la régularisation TV et la technique d'accélération FISTA. On rappelle que DART peut incorporer dans le processus de reconstruction des informations a priori sur les coefficients d'atténuation de l'objet inspecté. Pour la validation numérique de cet algorithme, le fantôme de type Defrise simulé par CIVA est utilisé à nouveau. Une connaissance a priori des coefficients d'atténuation correspondant aux différents matériaux (PMMA, Mg, Al and Ca) de l'objet est supposée. La configuration d'acquisition des données utilisée précédemment avec SART-FISTA-TV est considérée là encore. La Figure 8.17 montre des coupes horizontales et verticales des volumes reconstruits à partir des projections non bruitées pour SART-FISTA-TV et DART-FISTA-TV en première et deuxième ligne, respectivement. Visuellement, la qualité des images obtenue par DART-FISTA-TV est meilleure et les valeurs reconstruites sont plus précises comme on peut le voir sur la comparaison numérique tracée sur la ligne rouge.

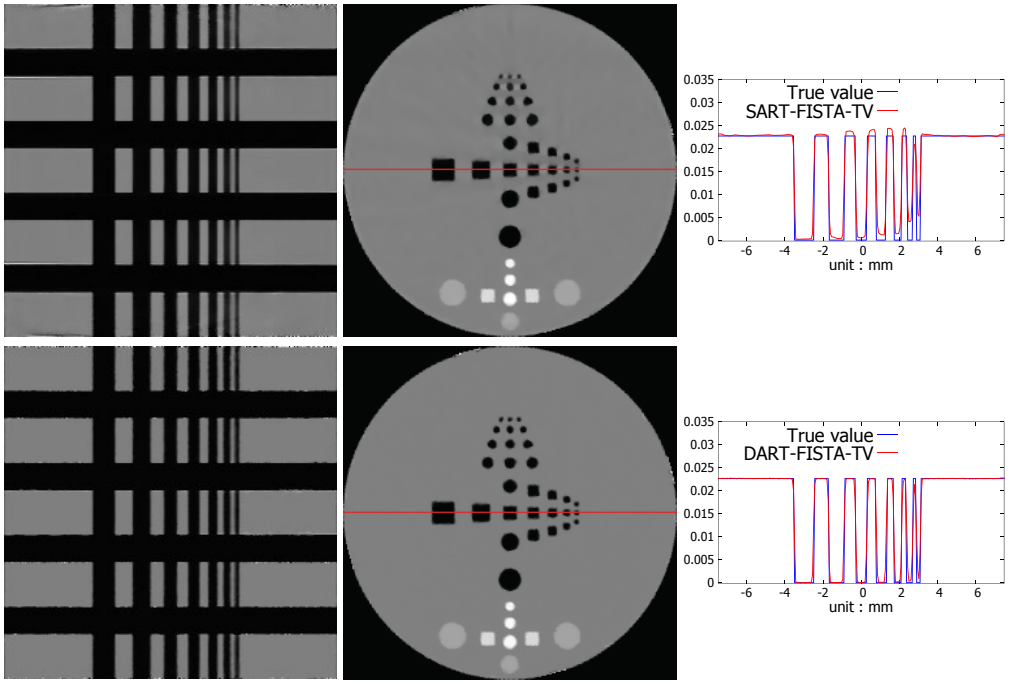

FIGURE 8.17: Reconstruction par SART-FISTA-TV (première ligne) et DART-FISTA-TV (deuxième ligne) à partir des données non bruitées.

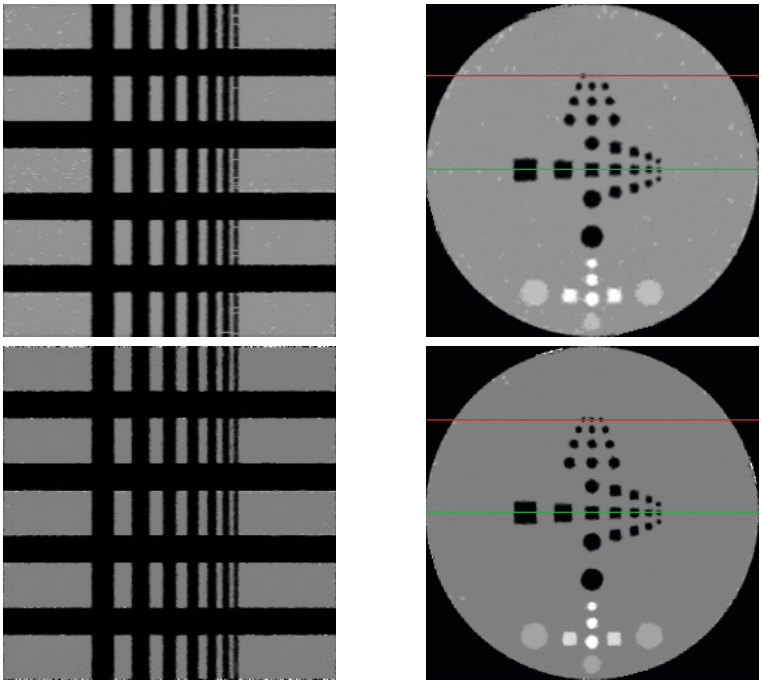

FIGURE 8.18: Reconstruction par DART (première ligne) et DART-FISTA-TV (deuxième ligne) à partir des données bruitées.

Pour montrer les avantages des modifications que nous proposons sur le DART, une reconstruction pour le cas où un bruit gaussien est ajouté aux projections est illustrée

en Figure 8.18. La moyenne de cette gaussienne est zéro et son écart-type $\sigma = 0.5\%$ de la valeur maximale des projections non bruitées. Les résultats obtenus par DART-FISTA-TV montrent clairement moins d'artefacts que celui de DART et la résolution spatiale est meilleure : en effet on peut remarquer que DART-FISTA-TV reconstruit les trois petits trous sur la ligne rouge alors que DART ne reconstruit qu'un seul trou.

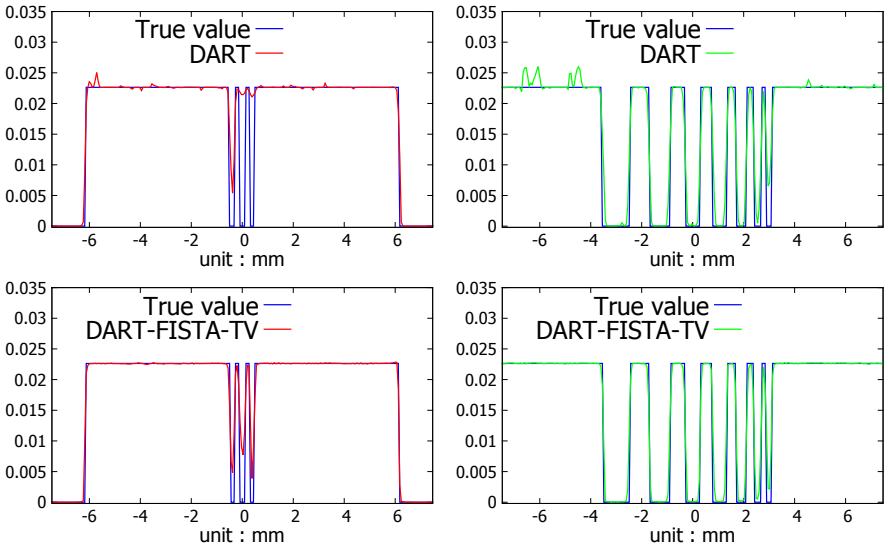

FIGURE 8.19: Une comparaison numérique sur les lignes rouges et vertes tracées en Figure 8.18.

Figure 8.19 montre une comparaison numérique sur les lignes rouges et vertes illustrées précédemment dans la Figure 8.18. Cette comparaison numérique montre que DART-FISTA-TV peut réduire le bruit et les valeurs reconstruites sont plus précises qu'avec DART.

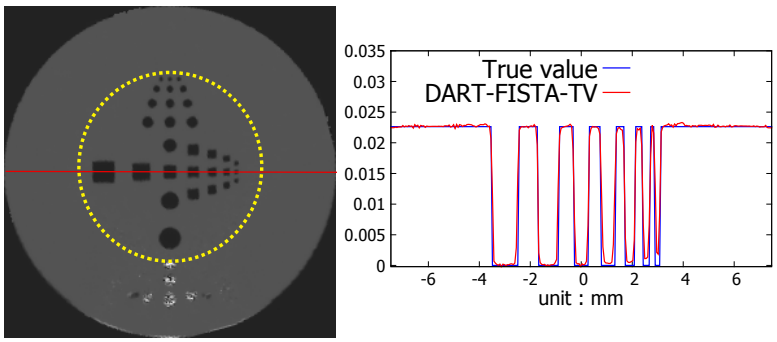

FIGURE 8.20: Reconstruction par DART-FISTA-TV à partir des données tronquées et non bruitées.

Enfin, la robustesse de DART-FISTA-TV aux données tronquées a été étudiée. La

largeur du détecteur utilisé est plus petite en réduisant le champ de vue à sa demi-taille. Dans cette simulation, des projections non bruitées sont acquises sur une trajectoire hélicoïdale inversée avec 9 tours, 10 projections par tour et un angle d'acquisition limité à $150°$. Au total, il y a 90 projections seulement et trois types de données manquantes sont existantes: un faible nombre de projections, un angle de vue limité et des données tronquées. Ainsi, le problème de reconstruction est sévèrement mal posé. Une coupe horizontale du volume reconstruit est représentée dans la Figure 8.20 où la région jaune en pointillé correspond à la région d'intérêt vue par le détecteur et la ligne rouge est utilisée pour une comparaison numérique. Il est clair que l'image reconstruite est de bonne qualité et les valeurs reconstruites sont très proches des valeurs originales même si les données sont tronquées, le nombre de projections est très faible et l'angle d'acquisition est limité à $150°$.

8.5.5 Validation Expérimentale

Nous montrons ici des résultats de reconstruction à partir des données réelles obtenues avec la plateforme robotique. Ces résultats sont divisés en trois parties. D'abord, des résultats avec une acquisition sur une trajectoire hélicoïdale sont présentés. Ensuite, une acquisition hélicoïdale d'un grand objet est effectuée et la reconstruction à partir des données tronquées est illustrée. Enfin, des reconstructions à partir des trajectoires limitées à $150°$ sont représentées.

Reconstruction sur une Trajectoire Hélicoïdale

L'objet inspecté est un vase créé par fabrication additive et fourni par la direction de l'énergie nucléaire (DEN) du CEA. Ce vase est de 10 cm en diamètre et de 15 cm en hauteur et contient un défaut qui est illustré par la région rouge sur la Figure 8.21a.

L'acquisition des données sur une trajectoire hélicoïdale en $360°$ ne peut être atteint en utilisant seulement la plateforme robotique à cause de la limitation sur l'angle de rotation de chaque robot. Pour réaliser cette trajectoire d'acquisition, l'objet est placé sur un plateau tournant et pendant la rotation de l'objet sur ce plateau, les deux robots se déplacent verticalement suivant la direction de l'axe de rotation. Une synchronisation entre la rotation de l'objet et le mouvement des robots est effectuée. Pendant l'acquisition, la tension du tube est de 150 kV, le courant est de 40 μA et une plaque d'aluminium de 1.5 mm a été placée pour éliminer les photons de basse énergie.

TABLE 8.3: Paramètres géométriques d'acquisition.

Distance source-objet (Dso)	40 cm
Distance source-détecteur (Dsd)	60 cm
Pas de l'hélice	6.48 cm

(A) Objet (B) Une projection 2D

FIGURE 8.21: Un vase créé par fabrication additive.

Les paramètres géométriques de cette acquisition hélicoïdale sont spécifiés dans le tableau 8.3 et une projection acquise est représentée sur la Figure 8.21b. Le nombre de projections par tour est 360 avec 4,5 tours au total. Le temps d'acquisition entre deux projections est de 2 secondes. D'abord, la rotation du plateau tournant prend 0,5 secondes, puis les deux robots ont besoin d'environ 0,5 secondes pour se stabiliser et enfin le temps de prendre l'image est de 1 seconde. La durée totale de cette acquisition est de 54 minutes.

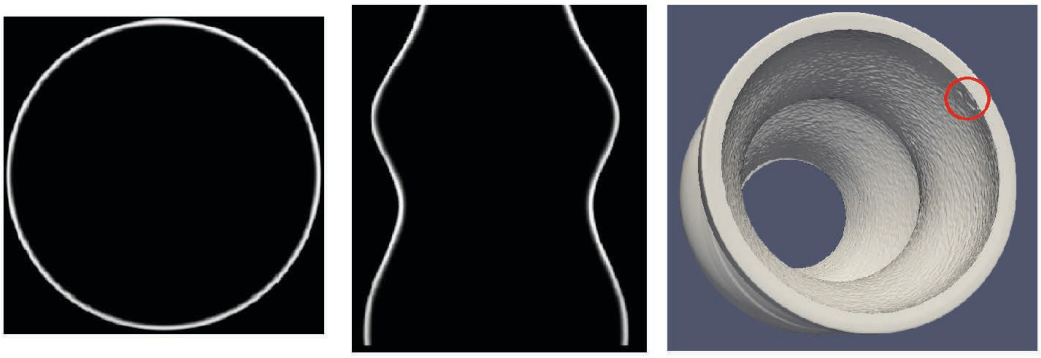

FIGURE 8.22: Une coupe horizontale (à gauche), une coupe verticale (au centre) et une vue 3D (à droite) du volume reconstruit avec l'algorithme standard de FDK.

L'algorithme de FDK a été choisi pour la reconstruction 3D et les résultats obtenus sont présentés sur la Figure 8.22 qui montre une coupe horizontale, une coupe verticale et une vue 3D du volume reconstruit. Il est clair que la reconstruction du vase est bonne et le défaut est bien détecté comme on peut l'observer dans la région rouge de la vue 3D présentée.

Reconstruction à partir des Données Tronquées

une culasse d'un moteur de 40 cm en hauteur et de 25 cm en largeur est inspectée. Cet objet est grand et ses projections sont tronquées. Le but est de reconstruire une région d'intérêt de 17 cm en hauteur et de 9 cm en largeur et qui correspond à la région jaune représentée sur la Figure 8.23a. La trajectoire hélicoïdale est utilisée encore avec les mêmes paramètres géométriques donnés précédemment. L'algorithme FDK$^{(1)}$ proposé en chapitre 4 est utilisé pour la reconstruction. Cette acquisition est réalisée avec une tension de tube de 180 kV et un courant de 60 μ A et une projection est illustrée sur la Figure 8.23b.

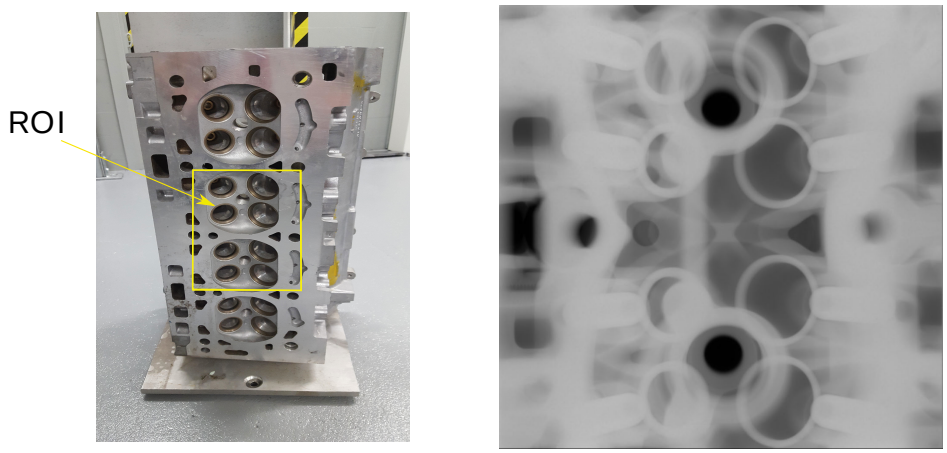

(A) Objet (B) Une projection 2D

FIGURE 8.23: une culasse d'un moteur.

L'objectif est de montrer les avantages de FDK$^{(1)}$ lorsque les données sont tronquées. Donc, la reconstruction avec cet algorithme est représentée sur la Figure 8.24 en même temps que la reconstruction obtenue en utilisant l'algorithme standard de FDK. Les résultats de reconstruction avec l'algorithme standard de FDK sont présentés dans la première ligne tandis que les résultats de FDK$^{(1)}$ sont affichés dans la deuxième ligne. La première colonne correspond à une coupe horizontale dans le volume reconstruit alors que les deuxième et troisième colonnes se rapportent à deux coupes verticales dans le volume reconstruit. On peut voir que les détails de la structure dans chaque coupe reconstruite avec FDK$^{(1)}$ sont mieux visualisés qu'avec l'algorithme standard de FDK. En outre, l'algorithme standard de FDK montre des artefacts nommés "Cup artifacts" sur les bords de la région d'intérêt en jaune alors que ces artefacts ne sont pas obtenus avec FDK$^{(1)}$.

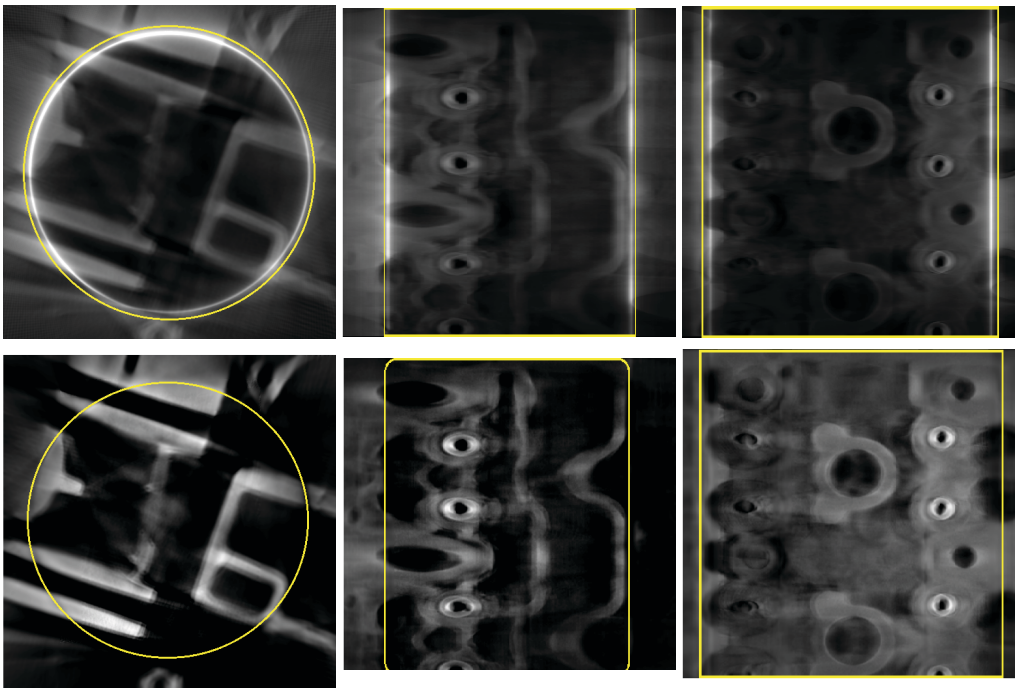

FIGURE 8.24: Reconstruction d'une culassse d'un moteur en utilisant l'algorithme standard de FDK (première ligne) et FDK$^{(1)}$ (deuxième ligne). Une coupe horizontale de chaque volume reconstruit est représentée sur la première colonne et deux coupes verticales sont représentées sur les deuxième et troisième colonnes.

Reconstruction avec un Angle de Vue Limité

Des validations expérimentales sur des trajectoires incomplètes limitées à $150°$ sont effectuées aussi. Deux composants créés par fabrication additive et qui sont fournis par la DEN sont utilisés pour l'inspection. Sachant que ces deux objets ne sont pas grands (moins de $10 \times 10 \times 10\,\text{cm}^3$), une trajectoire circulaire est suffisante pour l'acquisition de données. Ainsi, l'inspection est effectuée sur une trajectoire circulaire et 150 projections sont acquises avec un angle de vue limité à $150°$. La distance source-objet est 20 cm et la distance objet-detecteur est 60 cm. Pendant cette acquisition, seuls les deux robots se déplacent et l'objet reste fixe. La tension du tube est de 150 kV et le courant est de 500 μA. Sachant que le plateau tournant n'est pas utilisé ici, le temps entre deux projections acquises est de 1,5 seconde et la durée totale d'acquisition est de 3,75 minutes. Ces acquisitions sont présentées sur la Figure 8.25 et une projection de chaque composant est illustrée.

SART-FISTA-TV est choisi pour la reconstruction et on peut voir sur la Figure. 8.26 que ces deux objets sont reconstruits correctement malgré la limitation angulaire sur la trajectoire d'acquisition.

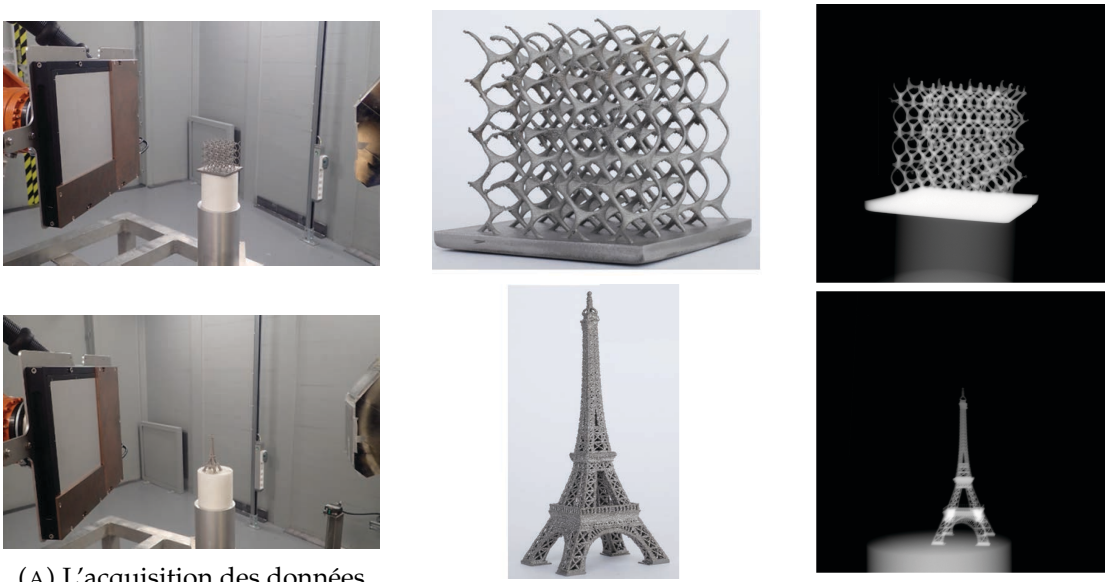

(A) L'acquisition des données

(B) Objet

(C) Une projection 2D

FIGURE 8.25: Inspection de deux composants créés par fabrication additive.

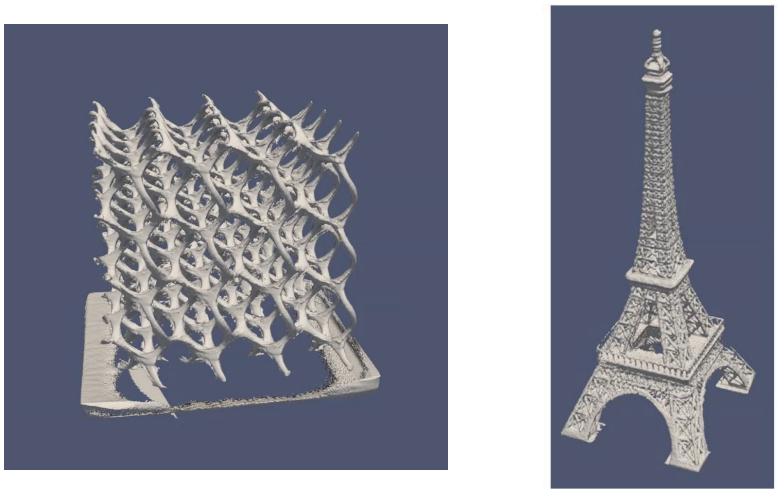

FIGURE 8.26: Reconstruction de deux composants créés par fabrication additive en utilisant SART-FISTA-TV.

8.6 Conclusions

Dans cette thèse, nous avons étudié des algorithmes pour la reconstruction sur des trajectoires non standards et qui pourraient être applicables à une cellule de tomographie X robotisée. Cette étude visait à examiner des méthodes existantes à la fois analytiques et itératives, puis à modifier les algorithmes appropriés afin de les adapter à notre application. En particulier, ce travail peut être divisé en trois parties : i) l'étude

des algorithmes analytiques, ii) l'étude des algorithmes itératifs et iii) la présentation de la reconstruction à partir des premières données expérimentales obtenues avec la plateforme robotique. L'étude de chaque algorithme comprend d'abord une analyse théorique puis sa validation et évaluation en utilisant des données simulées par CIVA. Pour ces évaluations numériques, nous nous sommes particulièrement intéressés à deux aspects principaux qui peuvent survenir lors de l'acquisition des données et notamment dans le cas de cette plateforme robotique : la troncation des données et l'angle de vue limité. En effet, les deux bras robotiques ne peuvent pas effectuer une rotation complète autour de l'objet à cause des contraintes mécaniques et l'angle de rotation est limité à $150°$. Cette difficulté est un défi majeur pour les algorithmes de reconstruction. De plus, pendant l'inspection des grands objets industriels, seule une région d'intérêt est imagée sur le détecteur et donc les projections acquises sont tronquées.

Dans la première partie, des méthodes analytiques ont été étudiées. L'étude a examiné des algorithmes exacts pour la reconstruction sur une trajectoire hélicoïdale. Parmi eux, deux algorithmes [149, 150] de type FBP et BPF ont été choisis et implémentés. Ici, nous avons proposé une implémentation optimisée pour l'algorithme de type FBP [150] et des simulations numériques ont été menées pour montrer les avantages de notre implémentation qui permet d'améliorer la qualité d'image reconstruite par rapport à l'implémentation existante.

L'inconvénient majeur de ces algorithmes exacts est qu'ils ne sont pas flexibles et qu'ils ne peuvent pas être adaptés aux trajectoires avec un angle de vue limité. Par conséquent, nous nous sommes intéressés ensuite à l'algorithme approximatif de FDK qui peut être facilement adapté aux trajectoires incomplètes en utilisant une fonction de pondération pour gérer la redondance des données. D'abord, nous avons travaillé sur la modification de cet algorithme pour gérer les troncations transversales des données en remplaçant le filtre de rampe par deux approches différentes. Les avantages de ces deux approches ont été illustrés mathématiquement et puis avec des simulations en utilisant des données tronquées générées par CIVA. Ensuite, l'un de ces algorithmes a été adapté à la trajectoire hélicoïdale inversée. Ainsi, l'algorithme analytique que nous proposons permet de gérer les deux aspects majeurs abordés dans la thèse: la troncation des données et l'angle de vue limité. Concernant l'angle de vue limité, la performance de l'algorithme est limitée à un certain degré en fonction de l'angle d'acquisition à cause du caractère analytique de l'algorithme qui est connu pour être plus sensible aux données manquantes par rapport aux algorithmes itératifs. En particulier, ces limitations ont été vues lorsque l'angle d'acquisition est très petit. Dans ce cas, il n'a pas été possible de reconstruire l'objet entier et seulement une région dans l'objet a été bien reconstruite. Par contre, l'angle d'acquisition qui peut être obtenu avec la plateforme robotique étant limité à $150°$ ce qui est relativement faible, cet algorithme analytique n'a pas été le choix optimal pour notre application et il était essentiel d'étudier des

algorithmes itératifs afin de résoudre ce problème.

Dans la deuxième partie, des algorithmes itératifs ont donc été étudiés. L'avantage principal de ces algorithmes est leur flexibilité puisqu'ils peuvent être appliqués aux trajectoires quelconques, ce qui est important pour l'utilisation de notre plateforme robotique afin d'effectuer des acquisitions sur des trajectoires non standards. Néanmoins, ce type d'algorithme est coûteux en temps de calcul par rapport aux algorithmes analytiques. Des méthodes algébriques ont été examinées et des techniques de régularisation ont été intégrées, telles que la régularisation de type TV qui a été utilisée pour régler le problème de limitation de l'angle de vue. Enfin, une technique appelée FISTA a été intégrée pour accélérer la convergence des algorithmes proposés.

Une des méthodes itératives que nous proposons nommée SART-FISTA-TV a été testée sur une trajectoire hélicoïdale inverse avec un angle d'acquisition limité à $150°$. Cet algorithme reconstruit la structure globale de l'objet alors que la reconstruction avec cette configuration n'était pas possible en utilisant l'algorithme de type FDK présenté. Un autre point intéressant de cet algorithme est qu'il est adapté à un très faible nombre de projections contrairement à l'algorithme de type FDK qui provoque des artefacts importants dans ce cas. En outre, cet algorithme est très robuste au bruit, mais son inconvénient principal est la présence d'artefacts en cas de données tronquées.

Pour améliorer encore la qualité de reconstruction sur ces trajectoires d'acquisition incomplètes, un autre algorithme algébrique nommé DART [7] a été étudié qui peut incorporer des informations a priori sur les différents matériaux de l'objet dans le processus de reconstruction. L'algorithme peut être appliqué si l'objet se compose de moins de cinq matériaux différents, ce qui est faisable dans les applications de CND où généralement l'objet inspecté est composé de quelques matériaux seulement comme l'aluminium, l'acier et le plastique. Notre contribution ici a été l'amélioration de performance de cet algorithme en le combinant avec la technique de régularisation TV. Cet algorithme a été testé sur une hélice inverse avec un angle d'acquisition limité à $150°$ et à partir d'un faible nombre de projections bruitées. Les résultats obtenus étaient satisfaisants et il a été montré que l'algorithme proposé DART-FISTA-TV a un impact significatif sur la qualité de l'image avec une réduction importante du bruit et une amélioration des performances par rapport à l'algorithme original DART. Il a été montré également que cet algorithme peut gérer les données tronquées. Cependant, les informations a priori nécessaires à cet algorithme sont contraignantes en particulier avec une source polychromatique où il est impossible de connaître exactement le coefficient d'atténuation de chaque matériau. Pour cette raison, il n'a pas été possible d'appliquer l'algorithme actuel de DART-FISTA-TV sur des données expérimentales et pour résoudre ce problème, des méthodes d'estimation automatique des coefficients d'atténuation devraient être intégrées comme discuté dans les perspectives.

Dans la troisième étape, des acquisitions expérimentales ont été réalisées avec la

plateforme robotique. Trois catégories des inspections ont été réalisées. La première catégorie considère la trajectoire hélicoïdale pour l'acquisition des données. Pour cette trajectoire et afin d'éviter la limitation sur l'angle de vue imposée par les deux robots, l'objet a été placé sur une plaque tournante et seulement une translation axiale de chaque robot a été réalisée. L'algorithme de FDK a été utilisé pour la reconstruction à partir de cette trajectoire. Deuxièmement, nous avons présenté des inspections de grands objets dont les projections ont été tronquées. Ici, FDK$^{(1)}$ a été utilisé pour la reconstruction de l'objet. Finalement, des inspections avec un angle de vue limité ont été réalisées. Dans ce cas, les deux robots ont été utilisés seulement et la trajectoire d'acquisition est circulaire avec un angle de vue limité à $150°$. Ici, les projections ne sont pas tronquées et SART-FISTA-TV a été utilisé pour la reconstruction. En général, les résultats de reconstruction obtenus avec toutes ces acquisitions étaient satisfaisants et les objets inspectés ont été reconstruits correctement malgré des données manquantes imposées dans certains cas. Ces premiers résultats expérimentaux sont encourageants et démontrent fortement la faisabilité de l'inspection robotique dans le CND.

En ce qui concerne le développement logiciel, cette thèse contribue à l'intégration de nouveaux plugins de reconstruction dans CIVA qui se limitait jusqu'ici à des algorithmes de reconstruction existants sur trajectoire circulaire. En particulier, nos plugins de reconstruction ont été adaptés aux trajectoires d'acquisition qui sont plus complexes avec des troncations de données et un angle de vue limité. Les trajectoires de type hélicoïdal ont été considérées pour la reconstruction analytique et l'algorithme de type FDK a été intégré et est disponible dans la version actuelle de CIVA. Pour la partie itérative, SART-FISTA-TV a été intégré aussi et il peut fonctionner avec des trajectoires quelconques. Les autres implémentations comme DART-FISTA-TV et l'algorithme exact de type FBP seront intégrées prochainement. Ces outils de reconstruction sont indispensables pour notre plateforme robotique. Une fois que l'acquisition de données est effectuée, les données expérimentales sont importées dans CIVA puis la reconstruction 3D de l'objet peut être réalisée en utilisant les plugins disponibles.

Pour résumer, cette thèse a adressé un nombre important d'aspects sur les algorithmes de reconstruction adaptés aux trajectoires non standard pour l'utilisation avec une plateforme robotique d'inspection. Plus précisément, cette thèse a présenté des algorithmes analytiques pour les trajectoires d'acquisition hélicoïdales, des algorithmes itératifs pour les trajectoires d'acquisition quelconques et des données réelles acquises avec la plateforme. Nous sommes convaincus que ces contributions sont une étape importante pour la tomographie robotisée dans le domaine industriel.

8.7 Perspectives

Comme le montre la session spéciale robotique organisée au dernier congrès mondial du CND (WCNDT2016), lors de laquelle notre présentation a été sélectionnée en Keynote, la tomographie robotisée est une tendance actuelle car elle donne plus de flexibilité sur la trajectoire d'acquisition et elle permet l'inspection d'objets plus complexes. Cette thèse a étudié et développé des algorithmes de reconstruction pour l'utilisation avec une plateforme de tomographie X robotisée. Les algorithmes proposés ont été validés sur des données réelles obtenues avec cette plateforme. Cependant, des améliorations pourraient encore être apportées dans l'avenir. Une perspective sur des propositions possibles et des idées pour la poursuite de ce travail sont données ici.

Bien que les algorithmes analytiques et itératifs proposés aient été validés sur des données simulées et réelles, deux améliorations pourraient être réalisées d'un point de vue implémentation. Tout d'abord, seules des implémentations CPU ont été développées pour les algorithmes analytiques en raison de leur faible coût de calcul par rapport aux alternatives itératives. Cependant, il est possible d'accélérer encore plus ces algorithmes en développant des implémentations GPU de l'étape de rétro-projection, sachant que cette étape est l'opération la plus lourde dans les approches analytiques. Deuxièmement, les algorithmes itératifs ont été accélérés avec des implémentations GPU sur une carte graphique, mais il y avait des limitations concernant la résolution du volume reconstruit et le nombre de projections qui peut être utilisé par ces algorithmes à cause de ses grandes exigences de mémoire. Ainsi, une gestion de la mémoire pour ces algorithmes serait d'un grand intérêt.

Les comparaisons numériques effectuées ont montré que DART-FISTA-TV peut donner des reconstructions précises, même avec plusieurs configurations de données manquantes. Ainsi, il serait très intéressant de modifier DART-FISTA-TV afin qu'il fonctionne avec des données expérimentales. Une méthode d'estimation qui pourrait automatiquement déterminer le niveau de gris correspondant à chaque matériau est importante. Dans ce contexte, certaines méthodes [110, 148] ont déjà été proposées et pourraient être intégrées dans notre algorithme.

Une caractéristique importante de la CT industrielle est que parfois un modèle CAO de l'objet inspecté est disponible. Cette information supplémentaire peut être avantageuse pour obtenir une reconstruction plus précise et pour accélérer le processus d'inspection en réduisant le nombre de projections. En particulier, cette information a priori sur l'objet pourrait être soit intégrée directement dans le processus de reconstruction des algorithmes itératifs, soit utilisée pour optimiser la trajectoire d'acquisition et pour l'adapter à l'objet en définissant les poses d'acquisition les meilleures par simulation [37]. Nous supposons ici des trajectoires plus complexes en utilisant tous les degrés de liberté. De plus, il serait intéressant de contrôler des objets industriels plus

complexes dans l'avenir.

Enfin, pour améliorer encore les reconstructions, il sera utile de travailler sur la calibration du système afin d'assurer le bon positionnement du système d'imagerie et pour corriger les erreurs d'alignement pendant l'acquisition de données qui ont introduit certains artefacts dans les images reconstruites. Il y a d'autres améliorations qui pourraient être possible aussi comme le développement d'une méthode de correction pour la diffusion et les artefacts de beam hardening.

List of Abbreviations

ART	**A**lgebraic **R**econstruction **T**echnique
ATRACT	**A**pproximate **T**runcation **R**esistant **A**lgorithm for **C**omputed **T**omography
BPF	**B**ack-**P**rojection **F**iltration
CCD	**C**harge **C**oupled **D**evice
CAD	**C**omputer-**A**ided-**D**esign
CB	**C**one-**B**eam
CS	**C**ompressed **S**ensing
CT	**C**omputed **T**omography
DART	**D**iscrete **A**lgebraic **R**econstruction **T**echnique
DBP	**D**ifferentiated **B**ack-**P**rojection
FBP	**F**iltered-**B**ack-**P**rojection
FDK	Algorithm of **F**eldkamp-**D**avis-**K**ress
FISTA	**F**ast **I**terative **S**hrinkage **T**hresholding **A**lgorithm
FFC	**F**lat **Field** **C**orrection
FOV	**F**ield **O**f **V**iew
ICD	**I**terative-**C**oordinate-**D**ecent
IR	**I**terative **R**econstruction
LS	**L**east **S**quares
MAP	**M**aximum **A** **P**osteriori
ML	**M**aximum **L**ikelihood
MLEM	**M**aximum **L**ikelihood **E**xpectation **M**aximization
NDT	**N**on-**D**estructive-**T**esting
OS	**O**rdered **S**ubsets
POCS	**P**rojection **O**n **C**onvex **S**ets
ROI	**R**egion **O**f **I**nterest
SART	**S**imultaneous **A**lgebraic **R**econstruction **T**echnique
SIRT	**S**imultaneous **I**terative **R**econstruction **T**echnique
SVD	**S**ingular **V**alue **D**ecomposition
TV	**T**otal **V**ariation
3D	**T**hree-**D**imensional
2D	**T**wo-**D**imensional

List of Symbols

$f(\overrightarrow{r})$	Attenuation function
P	Cone-beam Projection data
(x, y, z)	Coordinates of point M in system $(\overrightarrow{e}_x, \overrightarrow{e}_y, \overrightarrow{e}_z)$
P'	Cosine-weighted projection data
O_d	Detector center
$(\overrightarrow{e_u}, \overrightarrow{e_v}, \overrightarrow{e_w})$	Detector coordinate system
(u_d, v_d)	Detector pixel position
D	Distance source-detector
R	Helix radius
$2\pi h$	Helical pitch
ρ	Line integral
$(\overrightarrow{e}_x, \overrightarrow{e}_y, \overrightarrow{e}_z)$	Object coordinate system
M	Point located on the object
S	Position of the X-ray source
$\overrightarrow{r}$	Position vector of a point M
P^F	Projection data filtered using the kernel $1/\sin\gamma$
r	Radius of the object
h_r	Ramp filter kernel
λ	Rotation angle of the source
λ_{min}	Rotation angle corresponding to the lower endpoint of the helix
λ_{max}	Rotation angle corresponding to the upper endpoint of the helix
P_H	Row-wise Hilbert filtered projection data
P_L	Row-wise Laplace filtered projection data
P_R	Row-wise ramp filtered projection data

g	Weighted cone-beam back-projections
$\overrightarrow{\theta}$	X-ray unit vector

List of Figures

List of Tables

Bibliography

[1] Wim van Aarle et al. "Super-resolution for computed tomography based on discrete tomography". In: *Image Processing, IEEE Transactions on* 23.3 (2014), pp. 1181–1193.

[2] Hussein Banjak et al. "Implementation and evaluation of two helical CT reconstruction algorithms in CIVA". In: *42nd Annual Review of Progress in Quantitative Non-Destructive Evaluation: Incorporating the 6th European-American Workshop on Reliability of NDE*. Vol. 1706. AIP Publishing. 2016, p. 110001.

[3] Hussein Banjak et al. "Iterative CT Reconstruction on Limited Angle Trajectories Applied to Robotic Inspection". In: *43nd Annual Review of Progress in Quantitative Non-Destructive Evaluation*. AIP Publishing. 2017 (to be published).

[4] Hussein Banjak et al. "Reconstruction Algorithms for Reverse Helical Super-Short-Scan Mode". In: *4th International Meeting on Image Formation in X-ray Computed Tomography*. 2016.

[5] Hussein Banjak et al. "Two Local FBP Algorithms for Helical Cone-beam Computed Tomography". In: *Digital Industrial Radiology and Computed Tomography*. 2015.

[6] Hussein Banjak et al. "X-ray Computed Tomography Reconstruction on Non-Standard Trajectories for Robotized Inspection". In: *proceedings of the World Conference of NDT*. 2016.

[7] Kees Joost Batenburg and Jan Sijbers. "DART: a practical reconstruction algorithm for discrete tomography". In: *Image Processing, IEEE Transactions on* 20.9 (2011), pp. 2542–2553.

[8] RHT Bates and TM Peters. "Towards improvements in tomography". In: *New Zealand Journal of Science* 14.4 (1971), p. 883.

[9] Amir Beck and Marc Teboulle. "A fast iterative shrinkage-thresholding algorithm for linear inverse problems". In: *SIAM journal on imaging sciences* 2.1 (2009), pp. 183–202.

[10] FS Beckman. "The solution of linear equations by the conjugate gradient method". In: *Mathematical methods for digital computers* 1 (1960), pp. 62–72.

[11] Freek J Beekman and Chris Kamphuis. "Ordered subset reconstruction for x-ray CT". In: *Physics in medicine and biology* 46.7 (2001), p. 1835.

[12] Marcel Beister, Daniel Kolditz, and Willi A Kalender. "Iterative reconstruction methods in X-ray CT". In: *Physica medica* 28.2 (2012), pp. 94–108.

[13] Folkert Bleichrodt, Frank Tabak, and Kees Joost Batenburg. "SDART: An algorithm for discrete tomography from noisy projections". In: *Computer Vision and Image Understanding* 129 (2014), pp. 63–74.

[14] Charles A Bouman and Ken Sauer. "A unified approach to statistical tomography using coordinate descent optimization". In: *Image Processing, IEEE Transactions on* 5.3 (1996), pp. 480–492.

[15] Ronald Newbold Bracewell and ACf Riddle. "Inversion of fan-beam scans in radio astronomy". In: *The Astrophysical Journal* 150 (1967), p. 427.

[16] Jerrold T Bushberg et al. *The Essential Physics of Medical Imaging*. Lippincott Williams & Wilkins, 2011.

[17] Charles L Byrne. "Iterative image reconstruction algorithms based on cross-entropy minimization". In: *IEEE Transactions on image processing* 2.1 (1993), pp. 96–103.

[18] Zhiqiang Chen et al. "A limited-angle CT reconstruction method based on anisotropic TV minimization". In: *Physics in medicine and biology* 58.7 (2013), p. 2119.

[19] Seungryong Cho et al. "Exact reconstruction of volumetric images in reverse helical cone-beam CT". In: *Medical physics* 35.7 (2008), pp. 3030–3040.

[20] Rolf Clackdoyle and Michel Defrise. "Tomographic reconstruction in the 21st century". In: *Signal Processing Magazine, IEEE* 27.4 (2010), pp. 60–80.

[21] Allan Macleod Cormack. "Representation of a function by its line integrals, with some radiological applications". In: *Journal of applied physics* 34.9 (1963), pp. 2722–2727.

[22] Marius Costin et al. "CIVA CT, an advanced simulation platform for NDT". In: *6th Conference on Industrial Computed Tomography*. 2016.

[23] Andrei Dabravolski, Kees Joost Batenburg, and Jan Sijbers. "A multiresolution approach to discrete tomography using DART". In: *PloS one* 9.9 (2014), e106090.

[24] Per-Erik Danielsson et al. "Towards exact reconstruction for helical cone-beam scanning of long objects. A new detector arrangement and a new completeness condition". In: *Proc. 1997 Meeting on Fully 3D Image Reconstruction in Radiology and Nuclear Medicine (Pittsburgh)(DW Townsend and PE Kinahan, eds.)* 1997, pp. 141–144.

[25] Leonardo De Chiffre et al. "Industrial applications of computed tomography". In: *CIRP Annals-Manufacturing Technology* 63.2 (2014), pp. 655–677.

[26] Bruno De Man et al. "An iterative maximum-likelihood polychromatic algorithm for CT". In: *IEEE transactions on medical imaging* 20.10 (2001), pp. 999–1008.

[27] M Defrise and R Clack. "Filtered backprojection reconstruction of combined parallel beam and cone beam SPECT data". In: *Physics in medicine and biology* 40.9 (1995), p. 1517.

[28] Michel Defrise, Frédéric Noo, and Hiroyuki Kudo. "A solution to the long-object problem in helical cone-beam tomography". In: *Physics in Medicine and Biology* 45.3 (2000), p. 623.

[29] Michel Defrise, Frédéric Noo, and Hiroyuki Kudo. "Rebinning-based algorithms for helical cone-beam CT". In: *Physics in medicine and biology* 46.11 (2001), p. 2911.

[30] Michel Defrise et al. "Truncated Hilbert transform and image reconstruction from limited tomographic data". In: *Inverse problems* 22.3 (2006), p. 1037.

[31] Michel Defrise et al. "Truncated Hilbert transform and image reconstruction from limited tomographic data". In: *Inverse problems* 22.3 (2006), p. 1037.

[32] Junjun Deng et al. "A parallel implementation of the Katsevich algorithm for 3-D CT image reconstruction". In: *The Journal of Supercomputing* 38.1 (2006), pp. 35–47.

[33] Frank Dennerlein and Andreas Maier. "Approximate truncation robust computed tomographyATRACT". In: *Physics in medicine and biology* 58.17 (2013), p. 6133.

[34] David L Donoho. "Compressed sensing". In: *Information Theory, IEEE Transactions on* 52.4 (2006), pp. 1289–1306.

[35] LA Feldkamp, LC Davis, and JW Kress. "Practical cone-beam algorithm". In: *JOSA A* 1.6 (1984), pp. 612–619.

[36] Andreas Fieselmann et al. "Twin robotic x-ray system for 2D radiographic and 3D cone-beam CT imaging". In: *SPIE Medical Imaging*. International Society for Optics and Photonics. 2016, 97830G–97830G.

[37] Andreas Fischer et al. "Object Specific Trajectory Optimization for Industrial X-ray Computed Tomography". In: *Scientific reports* 6 (2016).

[38] Peter Gilbert. "Iterative methods for the three-dimensional reconstruction of an object from projections". In: *Journal of theoretical biology* 36.1 (1972), pp. 105–117.

[39] Richard Gordon, Robert Bender, and Gabor T Herman. "Algebraic reconstruction techniques (ART) for three-dimensional electron microscopy and X-ray photography". In: *Journal of theoretical Biology* 29.3 (1970), pp. 471–481.

[40] Richard Gordon, Robert Bender, and Gabor T Herman. "Algebraic reconstruction techniques (ART) for three-dimensional electron microscopy and X-ray photography". In: *Journal of theoretical Biology* 29.3 (1970), pp. 471–481.

[41] Pierre Grangeat. "Mathematical framework of cone beam 3D reconstruction via the first derivative of the Radon transform". In: *Mathematical methods in tomography*. Springer, 1991, pp. 66–97.

[42] Godfrey N Hounsfield. "Computerized transverse axial scanning (tomography): Part 1. Description of system". In: *The British journal of radiology* 46.552 (1973), pp. 1016–1022.

[43] Jiang Hsieh. "Adaptive streak artifact reduction in computed tomography resulting from excessive x-ray photon noise". In: *Medical Physics* 25.11 (1998), pp. 2139–2147.

[44] Jiang Hsieh. "Computed tomography: principles, design, artifacts, and recent advances". In: SPIE Bellingham, WA. 2009.

[45] Jiang Hsieh et al. "Recent advances in CT image reconstruction". In: *Current Radiology Reports* 1.1 (2013), pp. 39–51.

[46] Jicun Hu, Kwok Tam, and Jinyi Qi. "An approximate short scan helical FDK cone beam algorithm based on nutating curved surfaces satisfying the Tuys condition". In: *Medical physics* 32.6 (2005), pp. 1529–1536.

[47] Philipp JANELLO and Peter JAHNKE. "XXL-Micro-CT Comparative Evaluation of Microscopic Computed Tomography for Macroscopic Objects". In: *positions* 1 (), p. 17.

[48] Xin Jin et al. "Anisotropic total variation for limited-angle CT reconstruction". In: *IEEE Nuclear Science Symposuim & Medical Imaging Conference*. IEEE. 2010, pp. 2232–2238.

[49] Marc KachelrieSS, Stefan Schaller, and Willi A Kalender. "Advanced single-slice rebinning in cone-beam spiral CT". In: *Medical Physics* 27.4 (2000), pp. 754–772.

[50] Marc Kachelriess, Oliver Watzke, and Willi A Kalender. "Generalized multi-dimensional adaptive filtering for conventional and spiral single-slice, multi-slice, and cone-beam CT". In: *Medical physics* 28.4 (2001), pp. 475–490.

[51] Stefan Kaczmarz. "Angenäherte auflösung von systemen linearer gleichungen". In: *Bulletin International de lAcademie Polonaise des Sciences et des Lettres* 35 (1937), pp. 355–357.

[52] A. H. Andersen A. C. Kak. "Simultaneous Algebraic Reconstruction Technique (SART): A superior implementation of the ART Algorithm". In: *Ultrasonic Imaging* (1984).

[53] Avinash C.. Kak and Malcolm Slaney. *Principles of computerized tomographic imaging*. IEEE press, 1988.

[54] Willi A Kalender et al. "Spiral volumetric CT with single-breath-hold technique, continuous transport, and continuous scanner rotation." In: *Radiology* 176.1 (1990), pp. 181–183.

[55] Chris Kamphuis and Freek J Beekman. "Accelerated iterative transmission CT reconstruction using an ordered subsets convex algorithm". In: *Medical Imaging, IEEE Transactions on* 17.6 (1998), pp. 1101–1105.

[56] Alexander Katsevich. "Theoretically exact filtered backprojection-type inversion algorithm for spiral CT". In: *SIAM Journal on Applied Mathematics* 62.6 (2002), pp. 2012–2026.

[57] Alexander Katsevich, Samit Basu, and Jiang Hsieh. "Exact filtered backprojection reconstruction for dynamic pitch helical cone beam computed tomography". In: *Physics in Medicine and Biology* 49.14 (2004), p. 3089.

[58] Hiroyuki Kudo, Frederic Noo, and Michel Defrise. "Quasi-exact filtered backprojection algorithm for long-object problem in helical cone-beam tomography". In: *IEEE transactions on medical imaging* 19.9 (2000), pp. 902–921.

[59] Hiroyuki Kudo and Tsuneo Saito. "Helical-scan computed tomography using cone-beam projections". In: *Nuclear Science Symposium and Medical Imaging Conference, 1991., Conference Record of the 1991 IEEE*. IEEE. 1991, pp. 1958–1962.

[60] Hiroyuki Kudo, Michel Defrise, et al. "Cone-beam filtered-backprojection algorithm for truncated helical data". In: *Physics in Medicine and Biology* 43.10 (1998), p. 2885.

[61] Hiroyuki Kudo, Michel Defrise, et al. "Cone-beam filtered-backprojection algorithm for truncated helical data". In: *Physics in Medicine and Biology* 43.10 (1998), p. 2885.

[62] Hiroyuki Kudo et al. "New super-short-scan algorithms for fan-beam and cone-beam reconstruction". In: *Nuclear Science Symposium Conference Record, 2002 IEEE*. Vol. 2. IEEE. 2002, pp. 902–906.

[63] Hiroyuki Kudo et al. "Tiny a priori knowledge solves the interior problem in computed tomography". In: *Physics in medicine and biology* 53.9 (2008), p. 2207.

[64] Patrick J La Rivière and Xiaochuan Pan. "Nonparametric regression sinogram smoothing using a roughness-penalized Poisson likelihood objective function". In: *Medical Imaging, IEEE Transactions on* 19.8 (2000), pp. 773–786.

[65] Kenneth Lange. "Convergence of EM image reconstruction algorithms with Gibbs smoothing". In: *Medical Imaging, IEEE Transactions on* 9.4 (1990), pp. 439–446.

[66] Kenneth Lange, Richard Carson, et al. "EM reconstruction algorithms for emission and transmission tomography". In: *J Comput Assist Tomogr* 8.2 (1984), pp. 306–16.

[67] Soo-Jin Lee. "Accelerated coordinate descent methods for Bayesian reconstruction using ordered subsets of projection data". In: *International Symposium on Optical Science and Technology*. International Society for Optics and Photonics. 2000, pp. 170–181.

[68] Arnold Lent. "A convergent algorithm for maximum entropy image restoration, with a medical x-ray application". In: *Image Analysis and Evaluation* (1977), pp. 249–257.

[69] Arnold Lent and Yair Censor. "The primal-dual algorithm as a constraint-set-manipulation device". In: *Mathematical Programming* 50.1-3 (1991), pp. 343–357.

[70] Jeih-S Liow and SC Strother. "The convergence of object dependent resolution in maximum likelihood based tomographic image reconstruction". In: *Physics in medicine and biology* 38.1 (1993), p. 55.

[71] F Javier Maestre-Deusto et al. "ADART: An adaptive algebraic reconstruction algorithm for discrete tomography". In: *Image Processing, IEEE Transactions on* 20.8 (2011), pp. 2146–2152.

[72] SH Manglos et al. "Transmission maximum-likelihood reconstruction with ordered subsets for cone beam CT". In: *Physics in Medicine and Biology* 40.7 (1995), p. 1225.

[73] SH Manglos et al. "Transmission maximum-likelihood reconstruction with ordered subsets for cone beam CT". In: *Physics in Medicine and Biology* 40.7 (1995), p. 1225.

[74] Erkan U Mumcuoglu et al. "Fast gradient-based methods for Bayesian reconstruction of transmission and emission PET images". In: *IEEE transactions on Medical Imaging* 13.4 (1994), pp. 687–701.

[75] Frank Natterer. *The mathematics of computerized tomography*. Vol. 32. Siam, 1986.

[76] Frédéric Noo, Michel Defrise, and Rolf Clackdoyle. "Single-slice rebinning method for helical cone-beam CT". In: *Physics in Medicine and Biology* 44.2 (1999), p. 561.

[77] Frederic Noo, Hiroyuki Kudo, and Michel Defrise. "Approximate short-scan filtered-backprojection for helical CB reconstruction". In: *Nuclear Science Symposium, 1998. Conference Record. 1998 IEEE*. Vol. 3. IEEE. 1998, pp. 2073–2077.

[78] Frédéric Noo, Jed Pack, and Dominic Heuscher. "Exact helical reconstruction using native cone-beam geometries". In: *Physics in Medicine and Biology* 48.23 (2003), p. 3787.

[79] Frédéric Noo et al. "Image reconstruction from fan-beam projections on less than a short scan". In: *Physics in Medicine and Biology* 47.14 (2002), p. 2525.

[80] B Ohnesorge et al. "Efficient correction for CT image artifacts caused by objects extending outside the scan field of view". In: *Medical physics* 27.1 (2000), pp. 39–46.

[81] WH Oldendorf. "Isolated flying spot detection of radiodensity dis-continuities-displaying the internal structural pattern of a complex object". In: *IRE transactions on bio-medical electronics* 8.1 (1961), pp. 68–72.

[82] Peyma Oskoui-Fard and Henry Stark. "Tomographic image reconstruction using the theory of convex projections". In: *IEEE Transactions on Medical Imaging* 7.1 (1988), pp. 45–58.

[83] Jed D Pack and Frédéric Noo. "Cone-beam reconstruction using 1D filtering along the projection of M-lines". In: *Inverse Problems* 21.3 (2005), p. 1105.

[84] Jed D Pack, Frédéric Noo, and Rolf Clackdoyle. "Cone-beam reconstruction using the backprojection of locally filtered projections". In: *IEEE Transactions on Medical Imaging* 24.1 (2005), pp. 70–85.

[85] Jed D Pack, Frédéric Noo, and H Kudo. "Investigation of saddle trajectories for cardiac CT imaging in cone-beam geometry". In: *Physics in Medicine and Biology* 49.11 (2004), p. 2317.

[86] Xiaochuan Pan, Yu Zou, and Dan Xia. "Image reconstruction in peripheral and central regions-of-interest and data redundancy". In: *Medical physics* 32.3 (2005), pp. 673–684.

[87] Dennis L Parker. "Optimal short scan convolution reconstruction for fan beam CT". In: *Medical physics* 9.2 (1982), pp. 254–257.

[88] Dennis L Parker. "Optimal short scan convolution reconstruction for fan beam CT". In: *Medical physics* 9.2 (1982), pp. 254–257.

[89] Frank Sauer, Supun Samarasekera, and Kwok Tam. *Practical cone beam image reconstruction using local regions-of-interest*. US Patent 6,009,142. 1999.

[90] Ken Sauer and Charles Bouman. "A local update strategy for iterative reconstruction from projections". In: *Signal Processing, IEEE Transactions on* 41.2 (1993), pp. 534–548.

[91] Stefan Schaller et al. "Exact Radon rebinning algorithm for the long object problem in helical cone-beam CT". In: *IEEE transactions on medical imaging* 19.5 (2000), pp. 361–375.

[92] Stefan Schaller et al. "Novel approximate approach for high-quality image reconstruction in helical cone-beam CT at arbitrary pitch". In: *Medical Imaging 2001*. International Society for Optics and Photonics. 2001, pp. 113–127.

[93] Lawrence A Shepp and Benjamin F Logan. "The Fourier reconstruction of a head section". In: *IEEE Transactions on Nuclear Science* 21.3 (1974), pp. 21–43.

[94] Lawrence A Shepp and Yehuda Vardi. "Maximum likelihood reconstruction for emission tomography". In: *Medical Imaging, IEEE Transactions on* 1.2 (1982), pp. 113–122.

[95] Emil Y Sidky, Chien-Min Kao, and Xiaochuan Pan. "Accurate image reconstruction from few-views and limited-angle data in divergent-beam CT". In: *Journal of X-ray Science and Technology* 14.2 (2006), pp. 119–139.

[96] Emil Y Sidky and Xiaochuan Pan. "Image reconstruction in circular cone-beam computed tomography by constrained, total-variation minimization". In: *Physics in medicine and biology* 53.17 (2008), p. 4777.

[97] Bruce D Smith. "Cone beam convolution formula". In: *Computers in biology and medicine* 13.2 (1983), pp. 81–87.

[98] Bruce D Smith and JIXING Chen. "Implementation, investigation, and improvement of a novel cone-beam reconstruction method [SPECT]". In: *IEEE transactions on medical imaging* 11.2 (1992), pp. 260–266.

[99] Katsuyuki Taguchi, Be-Shan S Chiang, and Michael D Silver. "A new weighting scheme for cone-beam helical CT to reduce the image noise". In: *Physics in medicine and biology* 49.11 (2004), p. 2351.

[100] Kwon C Tam, S Samarasekera, and F Sauer. "Exact cone beam CT with a spiral scan". In: *Physics in medicine and biology* 43.4 (1998), p. 1015.

[101] Kwon C Tam, S Samarasekera, and F Sauer. "Exact cone beam CT with a spiral scan". In: *Physics in medicine and biology* 43.4 (1998), p. 1015.

[102] Xiangyang Tang and Jiang Hsieh. "A filtered backprojection algorithm for cone beam reconstruction using rotational filtering under helical source trajectory". In: *Medical physics* 31.11 (2004), pp. 2949–2960.

[103] Xiangyang Tang and Jiang Hsieh. "A filtered backprojection algorithm for cone beam reconstruction using rotational filtering under helical source trajectory". In: *Medical physics* 31.11 (2004), pp. 2949–2960.

[104] Xiangyang Tang and Jiang Hsieh. "Handling data redundancy in helical cone beam reconstruction with a cone-angle-based window function and its asymptotic approximation". In: *Medical physics* 34.6 (2007), pp. 1989–1998.

[105] Xiangyang Tang et al. "A helical cone-beam filtered backprojection (CB-FBP) reconstruction algorithm using 3D view weighting". In: *Optical Science and Technology, the SPIE 49th Annual Meeting*. International Society for Optics and Photonics. 2004, pp. 577–587.

[106] Xiangyang Tang et al. "A three-dimensional-weighted cone beam filtered backprojection (CB-FBP) algorithm for image reconstruction in volumetric CThelical scanning". In: *Physics in Medicine and Biology* 51.4 (2006), p. 855.

[107] Xiangyang Tang et al. "A three-dimensional-weighted cone beam filtered backprojection (CB-FBP) algorithm for image reconstruction in volumetric CThelical scanning". In: *Physics in Medicine and Biology* 51.4 (2006), p. 855.

[108] Jean-Baptiste Thibault et al. "A three-dimensional statistical approach to improved image quality for multislice helical CT". In: *Medical physics* 34.11 (2007), pp. 4526–4544.

[109] Heang K Tuy. "An inversion formula for cone-beam reconstruction". In: *SIAM Journal on Applied Mathematics* 43.3 (1983), pp. 546–552.

[110] Wim Van Aarle, Kees Joost Batenburg, and Jan Sijbers. "Automatic parameter estimation for the discrete algebraic reconstruction technique (DART)". In: *Image Processing, IEEE Transactions on* 21.11 (2012), pp. 4608–4621.

[111] Ge Wang, Yangbo Ye, and Hengyong Yu. "Approximate and exact cone-beam reconstruction with standard and non-standard spiral scanning". In: *Physics in medicine and biology* 52.6 (2007), R1.

[112] Ge Wang, Hengyong Yu, and Bruno De Man. "An outlook on x-ray CT research and development". In: *Medical physics* 35.3 (2008), pp. 1051–1064.

[113] Ge Wang et al. "A general cone-beam reconstruction algorithm". In: *Medical Imaging, IEEE Transactions on* 12.3 (1993), pp. 486–496.

[114] G Wang et al. "Half-scan cone-beam X-ray microtomography formula". In: *Scanning* 16.4 (1994), pp. 216–220.

[115] Xian-Chao Wang et al. "Cone-beam local reconstruction based on a Radon inversion transformation". In: *Chinese Physics B* 21.11 (2012), p. 8702.

[116] Yan Xia et al. “Reconstruction from truncated projections in cone-beam CT using an efficient 1D filtering”. In: *SPIE Medical Imaging*. International Society for Optics and Photonics. 2013, pp. 86681C–86681C.

[117] Yan Xia et al. “Scaling calibration in region of interest reconstruction with the 1D and 2D ATRACT algorithm”. In: *International journal of computer assisted radiology and surgery* 9.3 (2014), pp. 345–356.

[118] Fang Xu et al. “On the efficiency of iterative ordered subset reconstruction algorithms for acceleration on GPUs”. In: *Computer methods and programs in biomedicine* 98.3 (2010), pp. 261–270.

[119] Guorui Yan et al. “Fast Katsevich algorithm based on GPU for helical cone-beam computed tomography”. In: *IEEE Transactions on information technology in biomedicine* 14.4 (2010), pp. 1053–1061.

[120] Xiao-hong Yan and RM Leahy. “Cone beam tomography with circular, elliptical and spiral orbits”. In: *Physics in Medicine and Biology* 37.3 (1992), p. 493.

[121] Haiquan Yang et al. “Exact cone beam reconstruction for a saddle trajectory”. In: *Physics in medicine and biology* 51.5 (2006), p. 1157.

[122] Jiansheng Yang et al. “Parallel implementation of Katsevich’s FBP algorithm”. In: *International journal of biomedical imaging* 2006 (2006).

[123] Yangbo Ye and Ge Wang. “Filtered backprojection formula for exact image reconstruction from cone-beam data along a general scanning curve”. In: *Medical Physics* 32.1 (2005), pp. 42–48.

[124] Yangbo Ye, Hengyong Yu, and Ge Wang. “Exact interior reconstruction with cone-beam CT”. In: *International journal of biomedical imaging* 2007 (2008).

[125] Yangbo Ye et al. “A general exact reconstruction for cone-beam CT via backprojection-filtration”. In: *IEEE Transactions on Medical Imaging* 24.9 (2005), pp. 1190–1198.

[126] Yangbo Ye et al. “A general local reconstruction approach based on a truncated Hilbert transform”. In: *Journal of Biomedical Imaging* 2007.1 (2007), pp. 2–2.

[127] Yangbo Ye et al. “Exact reconstruction for cone-beam scanning along nonstandard spirals and other curves”. In: *Optical Science and Technology, the SPIE 49th Annual Meeting*. International Society for Optics and Photonics. 2004, pp. 293–300.

[128] Jiangsheng You and Gengsheng L Zeng. “Explicit finite inverse Hilbert transforms”. In: *Inverse Problems* 22.3 (2006), p. L7.

[129] Dan C Youla and Heywood Webb. “Image Restoration by the Method of Convex Projections: Part 1 Theory”. In: *IEEE transactions on medical imaging* 1.2 (1982), pp. 81–94.

[130] Dan C Youla and Heywood Webb. "Image Restoration by the Method of Convex Projections: Part 1Theory". In: *Medical Imaging, IEEE Transactions on* 1.2 (1982), pp. 81–94.

[131] Hengyong Yu and Ge Wang. "Compressed sensing based interior tomography". In: *Physics in medicine and biology* 54.9 (2009), p. 2791.

[132] Hengyong Yu and Ge Wang. "Studies on implementation of the Katsevich algorithm for spiral cone-beam CT". In: *Journal of X-ray Science and Technology* 12.2 (2004), pp. 97–116.

[133] Hengyong Yu, Yangbo Ye, and Ge Wang. "Katsevich-type algorithims for variable radius spiral cone-beam CT". In: *Optical Science and Technology, the SPIE 49th Annual Meeting*. International Society for Optics and Photonics. 2004, pp. 550–557.

[134] Hengyong Yu et al. "A backprojection-filtration algorithm for nonstandard spiral cone-beam CT with an n-PI-window". In: *Physics in Medicine and Biology* 50.9 (2005), p. 2099.

[135] Hengyong Yu et al. "Exact BPF and FBP algorithms for nonstandard saddle curves". In: *Medical Physics* 32.11 (2005), pp. 3305–3312.

[136] Zhicong Yu et al. "Axially Extended-Volume C-Arm CT Using a Reverse Helical Trajectory in the Interventional Room". In: *Medical Imaging, IEEE Transactions on* 34.1 (2015), pp. 203–215.

[137] Zhou Yu et al. "Fast model-based X-ray CT reconstruction using spatially nonhomogeneous ICD optimization". In: *Image Processing, IEEE Transactions on* 20.1 (2011), pp. 161–175.

[138] Zhou Yu et al. "Fast model-based X-ray CT reconstruction using spatially nonhomogeneous ICD optimization". In: *IEEE Transactions on image processing* 20.1 (2011), pp. 161–175.

[139] Zhou Yu et al. "Non-homogeneous updates for the iterative coordinate descent algorithm". In: *Electronic Imaging 2007*. International Society for Optics and Photonics. 2007, 64981B–64981B.

[140] Z Yu et al. "FDK-type reconstruction algorithms for the reverse helical trajectory". In: *Nuclear Science Symposium and Medical Imaging Conference (NSS/MIC), 2011 IEEE*. IEEE. 2011, pp. 3980–3985.

[141] Gengsheng Lawrence Zeng, R Clack, and GT Gullberg. "Implementation of Tuy's cone-beam inversion formula". In: *Physics in medicine and biology* 39.3 (1994), p. 493.

[142] Gengsheng L Zeng et al. "Two finite inverse Hilbert transform formulae for region-of-interest tomography". In: *International Journal of Imaging Systems and Technology* 17.4 (2007), pp. 219–223.

[143] Jun Zhao et al. "Feldkamp-type reconstruction algorithms for spiral cone-beam CT with variable pitch". In: *Journal of X-ray Science and Technology* 15.4 (2007), pp. 177–196.

[144] Shiying Zhao, Hengyong Yu, and Ge Wang. "A family of analytic algorithms for cone-beam CT". In: *Optical Science and Technology, the SPIE 49th Annual Meeting*. International Society for Optics and Photonics. 2004, pp. 318–328.

[145] Shiying Zhao, Hengyong Yu, and Ge Wang. "A unified framework for exact cone-beam reconstruction formulas". In: *Medical physics* 32.6 (2005), pp. 1712–1721.

[146] J Zhou et al. "Computed laminography for materials testing". In: *Applied physics letters* 68.24 (1996), pp. 3500–3502.

[147] Tingliang Zhuang et al. "Fan-beam and cone-beam image reconstruction via filtering the backprojection image of differentiated projection data". In: *Physics in Medicine and Biology* 49.24 (2004), p. 5489.

[148] Xiaodong Zhuge, Willem Jan Palenstijn, and Kees Batenburg. "TVR-DART: a more robust algorithm for discrete tomography from limited projection data with automated gray value estimation". In: (2015).

[149] Yu Zou and Xiaochuan Pan. "Exact image reconstruction on PI-lines from minimum data in helical cone-beam CT". In: *Physics in Medicine and Biology* 49.6 (2004), p. 941.

[150] Yu Zou and Xiaochuan Pan. "Image reconstruction on PI-lines by use of filtered backprojection in helical cone-beam CT". In: *Physics in medicine and biology* 49.12 (2004), p. 2717.

[151] Yu Zou, Xiaochuan Pan, and Emil Y Sidky. "Theory and algorithms for image reconstruction on chords and within regions of interest". In: *JOSA A* 22.11 (2005), pp. 2372–2384.

[152] Yu Zou et al. "PI-line-based image reconstruction in helical cone-beam computed tomography with a variable pitch". In: *Medical physics* 32.8 (2005), pp. 2639–2648.

FOLIO ADMINISTRATIF

THESE DE L'UNIVERSITE DE LYON OPEREE AU SEIN DE L'INSA LYON

NOM : **BANJAK** DATE de SOUTENANCE : **10/11/2016**

Prénoms : **Hussein**

TITRE : **Reconstruction 3D en Tomographie X sur Trajectoires Non-Standards**

NATURE : **Doctorat** Numéro d'ordre : 2016LYSEI113

Ecole doctorale : **Electronique, Electrotechnique Automatique (EEA)**

Spécialité : **Traitement du Signal et de l'Image**

RESUME :

La tomographie par rayons X ou CT pour "Computed Tomography" est un outil puissant pour caractériser et localiser les défauts internes et pour vérifier la conformité géométrique d'un objet. Contrairement au cas des applications médicales, l'objet inspecté en Contrôle Non Destructif (CND) peut être très grand et composé de matériaux de haute atténuation, auquel cas l'utilisation d'une trajectoire circulaire pour l'inspection est impossible à cause de contraintes dans l'espace. Pour cette raison, l'utilisation de bras robotisés est l'une des nouvelles tendances reconnues dans la CT, car elle autorise plus de flexibilité dans la trajectoire d'acquisition et permet donc la reconstruction 3D de régions difficilement accessibles dont la reconstruction ne pourrait pas être assurée par des systèmes de tomographie industriels classiques. Une cellule de tomographie X robotisée a été installée au CEA. La plateforme se compose de deux bras robotiques pour positionner et déplacer la source et le détecteur en vis-à-vis. Parmi les nouveaux défis posés par la tomographie robotisée, nous nous concentrons ici plus particulièrement sur la limitation de l'ouverture angulaire imposée par la configuration en raison des contraintes importantes sur le mouvement mécanique de la plateforme. Le deuxième défi majeur est la troncation des projections qui se produit lorsque l'objet est trop grand par rapport au détecteur. L'objectif principal de ce travail consiste à adapter et à optimiser des méthodes de reconstruction CT pour des trajectoires non standard. Nous étudions à la fois des algorithmes de reconstruction analytiques et itératifs. Avant d'effectuer des inspections robotiques réelles, nous comptons sur des simulations numériques pour évaluer les performances des algorithmes de reconstruction sur des configurations d'acquisition de données. Pour ce faire, nous utilisons CIVA, qui est un outil de simulation pour le CND développé au CEA et qui est capable de simuler des données de projections réalistes correspondant à des configurations d'acquisition définies par l'utilisateur.

MOTS-CLÉS : **Tomographie X robotisée, contrôle non destructif, algorithmes analytiques et itératifs, trajectoires non-standards.**

Laboratoire (s) de recherche :
CEA-LIST, Département d'Imagerie et de Simulation pour le Contrôle (DISC)
Laboratoire Vibrations Acoustique (LVA)

Directeur de thèse: **Valérie KAFTANDJIAN**

Président de jury : Françoise PEYRIN

Composition du jury : **Jan SIJBERS, Thomas RODET, Françoise PEYRIN, Ulf HASSLER, Agnès DECROUX, Valérie KAFTANDJIAN, Marius COSTIN, Caroline VIENNE**